Enhanced Raman Scattering of Molecular Monolayers

DISSERTATION
zur Erlangung des akademischen Grades
Dr. rer. nat.

im Fach Chemie

Spezialisierung: Angewandte Analytik und Umweltchemie

eingereicht an der

Mathematisch-Naturwissenschaftlichen Fakultät
der Humboldt-Universität zu Berlin

von

M.Sc. Wan-Ing Lin

Präsidentin der Humboldt-Universität zu Berlin

Prof. Dr. Sabine Kunst

Dekan der Mathematisch-Naturwissenschaftlichen Fakultät

Prof. Dr. Elmar Kulke

Gutachter/innen:

1. Prof. Dr. Jürgen P. Rabe
2. Prof. Dr. Renato Zenobi
3. Prof. Dr. Janina Kneipp

Tag der mündlichen Prüfung: 28.03.2017

Abstract

The quest to achieve ultrahigh sensitivity, surface specificity and high spatial resolution has led the development of plasmon- and chemically- enhanced Raman spectroscopy, including techniques such as surface-enhanced Raman spectroscopy (SERS) and tip-enhanced Raman spectroscopy (TERS). Although there are many applications shown in the literature, a lack of fundamental understanding and its corresponding experimental demonstrations still remains.

In this thesis, I firstly used gap-mode TERS. In this geometry, the tip induces mirror dipoles on the surface and generates a highly confined strong electromagnetic field in this nanogap, which allows studying even molecularly thin layers of very weakly scattering molecules. With the nanoscale spatial resolution provided by TERS, the spontaneous segregation in a mixed thiol system on a gold surface could be resolved, while scanning tunneling microscopy (STM) could not discern the nanodomains via their apparent height difference.

Furthermore, graphene-enhanced Raman spectroscopy was investigated, since graphene was recently reported to provide some Raman enhancement through a chemical mechanism. A flat gold surface is also known to provide some surface enhancement mainly through a chemical mechanism. Sandwiching copper phthalocyanine (CuPc) molecules between graphene and a flat gold surface allowed electrons to be transferred in both directions, and thereby to address the question whether chemical enhancements with different origins in SERS can add to each other. The results suggest that a photon-driven charge transfer between molecules and gold, and a ground-state charge transfer between molecules and graphene can occur simultaneously. Therefore the chemical enhancements were influenced by the two individual surfaces, and a 68-fold enhancement of sandwiched CuPc between graphene and gold was observed, as compared to CuPc on mica.

Last, TERS was applied to study this sandwiched structure. Molecules self-assembled on a gold surface and covered by transferred graphene acted as optical probes. Such an arrangement has interesting properties in the sense that molecules are prevented from physical or chemical degradation as a result of the graphene encapsulation. Also, a possible ultrahigh Raman enhancement together with localized spatial resolution may be achieved due to the combined effects from SERS and TERS. The results showed that a tip providing enhancement through an electromagnetic mechanism (EM) can improve graphene-enhanced Raman scattering (GERS) further by 4 orders of magnitude. However, the bare molecules are

more strongly enhanced than the ones covered by graphene, by an order of magnitude. This indicates that graphene exerts a shielding effect to gap-mode TERS, probably because the mirror dipole in the gold surface is less strongly induced.

Keyword: TERS, STM, SERS, Graphene

Zusammenfassung

Um hochsensitive räumliche Auflösung zu erreichen, wurden oberflächenverstärkte Raman-Spektroskopie (SERS) und spitzenverstärkte Raman-Spektroskopie (TERS) weiterentwickelt. Obwohl in der Literatur viele Anwendungen beschrieben sind, ist das grundlegende Funktionsprinzip noch nicht voll verstanden und auch Experimente dazu fehlen teilweise.

In dieser Arbeit habe ich zuerst Gap-mode TERS eingesetzt. In dieser Geometrie induziert die Spitze Spiegeldipole an der Oberfläche und erzeugte ein räumlich begrenztes, starkes elektromagnetisches Feld in diesem Nanogap, das es ermöglicht, dünne Schichten von sehr schwach streuenden Molekülen zu untersuchen. Mit der von TERS bereitgestellten Nanometerauflösung konnte ein auf der Goldoberfläche spontan phasen-separiertes gemischtes Thiolsystem räumlich aufgelöst werden, während STM die Nanodomänen nicht über ihre Höhenunterschiede erkennen konnte.

Des Weiteren wurde Graphen eingeführt, um den grundlegenden Mechanismus von SERS zu untersuchen, da neue Studien eine Raman-Verstärkung durch Graphen durch einen chemischen Mechanismus anzeigen. Es ist bekannt, dass eine flache Goldoberfläche Oberflächenverstärkung durch einen chemischen Mechanismus induziert. Kupfer Phthalocyanin (CuPc)-Moleküle zwischen Graphen und einer flachen Goldoberfläche erlauben Elektronenübertragungen in beide Richtungen und damit stellt sich die Frage, ob chemische Verstärkungen von SERS zueinander addiert werden können. Die Ergebnisse deuten darauf hin, dass ein photonengetriebener Ladungstransfer zwischen Molekülen und Gold und ein Grundzustand-Ladungstransfer zwischen den Molekülen und Graphen gleichzeitig auftreten können. Somit zeigt dieses chemische System eine Kopplung von zwei einzelnen Oberflächen und es wurde eine 68-fache Verstärkung von geschichtetem CuPc zwischen Graphen und Gold beobachtet, jeweils bezogen auf CuPc auf Glimmer.

Schließlich wurde TERS angewendet, um diese Schichtstruktur zu untersuchen. Moleküle, die auf der Goldoberfläche selbstassembliert und mit übertragenem Graphen bedeckt sind, fungieren als optische Sensoren. Solche Anordnungen haben die interessante Eigenschaft, dass die Graphenverkapselung den physikalischen oder chemischen Abbau der Moleküle vermeidet. Außerdem kann möglicherweise eine ultrahohe Raman-Verstärkung zusammen mit lokalisierter Ortsauflösung aufgrund der zusammengesetzten Effekte von SERS und TERS herbeigeführt werden. Die Ergebnisse zeigen, dass eine Spitze, die eine EM-Verstärkung erzeugt, die Graphen-verstärkte Raman-Streuung (GERS) zusätzlich um vier

Größenordnungen verbessern kann. Jedoch werden die unbedeckten Moleküle um eine Größenordnung stärker gestärkt als die mit Graphen bedeckten. Dies deutet darauf hin, dass Graphen eine Abschirmwirkung auf Gap-mode TERS bewirken kann, sodass weniger Spiegeldipole in der Goldoberfläche induziert werden.

Schlagwörter: TERS, RTM, SERS, Graphen

Contents

Chapter 1

Introduction

The demand for miniaturization, in order to promote ever-higher efficiency and performance in the electronics and chips industry, has swept the scientific world over the last decades. It has transformed the development of science and technology, with the goal of "seeing" into big things on an ever-smaller scale. Microscopy, as an analog to cameras and telescopes, gives science a method to perceive the universe. Conventional optical microscopy associated with spectroscopy, such as Raman and Infrared (IR), provides a rich and readily accessible chemical fingerprint. However, limited in its ultimate resolution by Abbe's law[1] – to around half the wavelength of the incident light - it only allows analysis hundred-fold coarser than desired (Fig. 1a). The introduction of electron microscopies, e.g. scanning electron microscopy (SEM) and transmission electron microscopy (TEM), improved the resolution limit down to the nanoscale. But it requires working in high vacuum conditions and demands *a priori* knowledge about the sample before complete information can be obtained. The invention of scanning tunneling microscopy (STM), followed by atomic force microscopy (AFM), not only provides precise atomic resolution, but also opens the door to characterization in ambient conditions. Nevertheless, it suffers the same issues as electron microscopies (Fig. 1b). Despite high resolution and ease of use, a lack of chemical information is discouraging. In order to combine the merits of scanning probe microscopy and optical spectroscopy, tip-enhanced Raman spectroscopy (TERS) was developed and improved to attain the lateral super-high resolution with abundant chemical information *simultaneously* (Fig. 1c).

Figure 1.1 A photo of *Brandenburger Tor* in a) coarse-resolution as an analogy of conventional optical microscopy associated with spectroscopy, b) high resolution as an analogy of STM and AFM, and c) high resolution combining with color as an analogy of TERS. (Figure idea based on Mischa Nicklaus [2])

The working principle of TERS traces back to surface-enhanced Raman spectroscopy (SERS).[3, 4] SERS involves the use of nanostructured coinage materials to amplify the signal intensities up to million- or billion-fold. This effect arises from the metal nanostructures harvesting light and acting as nanoantenna to concentrate the electromagnetic field, resulting in the amplification of the molecules' signal in its proximity. The light-matter interaction allows the detection of a small volume of samples and even ultra-high sensitivity down to the single molecule level. Ever since the first observation of unexpectedly high Raman signal intensities for pyridine molecules adsorbed on a roughened silver electrode,[5] SERS has been an area of focus in research. In spite of the demonstration of many successful applications, the direct identification of the underlying principle has been hard to carry out. Measurements also suffer from reproducibility issues due to the inconsistent size and random distribution of many "hot spots" on a surface. A reproducible SERS effect relies on the precise construction of nanomaterials, since a structural difference of only a few nanometers can lead to distinctly different physical and chemical properties.[6] Progresses in nanofabrication techniques such as optical lithography or electron beam lithography have advanced the understanding and performance of this technique. With increasing levels of attention and applications, a term to describe the technique using localized surface plasmons has even been coined: plasmon-enhanced Raman spectroscopy.[7] The investigation of nanoscale dimers showed that the two tiny metallic nanoparticles in close proximity could communicate. When illuminated, the metal nanoparticles exhibit a collective surface plasmon resonance of a dipolar nature. The gap between the two metals accommodates even more intense optical fields. The exploitation of this intense optical field is of great interest for near-field enhancement, acting as a new light source.

In this thesis, the strong near-field enhancement between a metallic nanoparticle on a tip and a metallic surface, commonly referred to as gap-mode TERS, was implemented to investigate a spontaneous nano-phase-segregation of two different thiols self-assembled on a gold surface. Presented in Chapter 4, this large local field combined with a scanning technique afforded by STM makes nanoscale chemical imaging available. If these two mixed thiols show spontaneous segregation on a gold surface at the nanoscale, this would imply new opportunities for molecular electronic devices to be designed and well controlled on a two-dimensional surface for future progress.

In addition to this large optical near-field enhancement, which is usually described as *electromagnetic enhancement* (EM), there is another effect contributing multiplicatively to the

total enhancement called *chemical enhancement* (CM) in SERS.[8] It takes place when molecules are adsorbed on a surface. The underlying mechanism is usually viewed as a modification of the electronic Raman polarizability of the molecules upon adsorption to the metallic surface, and also may be due to charge-transfer effects between molecules and the surface; both may induce resonant Raman scattering.[8] The existence of chemical enhancement is still subject to controversy, due to difficulties in experimental control. However, it is usually believed to be much smaller than the electromagnetic mechanism by two orders of magnitude.[3, 8] While there are a lot of studies working on the electromagnetic enhancement either experimentally or theoretically, the studies on chemical enhancement are still very scarce as there are difficulties in carrying out measurements experimentally and the separation of effects originating from the dominant electromagnetic enhancement.

Graphene, a single atomic thin layer of carbon atoms arranged in a 2D hexagonal lattice, has recently shown a surface enhancement effect in Raman spectroscopy.[9] As a newly emerged novel material, graphene exhibits several unique properties making it ideal for many electronic applications and light harvesting. It has a vanishing electronic gap showing distinct electronic properties. It absorbs 2.3% of the light in the visible and near-infrared range with only a single atom thickness[10] and also it is a wide and extremely flat surface, which intrinsically serves as an extraordinary platform for light-matter interactions. The use of graphene in optical fields not only provides a tighter confinement for light traveling, but also quenches the fluorescence from electronic transitions. Besides the applications in optical fields, the benefits of using graphene include encapsulation applications,[11, 12] i.e. protection of molecules from physical or chemical decay. Also, graphene can immobilize single molecules, giving opportunities to the pursuit of single molecule sensitivity; it also provides the ability to work at ambient conditions. Due to the flat surface and inherent properties as a substrate, graphene induces and allows the exploration of molecular orientations on its surface. [13, 14] Lately, it has been shown that monolayer graphene can offer a seven-fold enhancement of evanescent fields in infrared microscopy, resolving subsurface information at a 500 nm depth.[15, 16] Additionally, the surface enhancement of graphene is also proven for Raman spectroscopy in the visible light range. The fundamental mechanism of graphene-enhanced Raman spectroscopy (GERS) was experimentally demonstrated to be a chemical enhancement effect.[17]

Since enhancement from a flat gold surface was also argued to be dominated by chemical enhancement in SERS,[18] bringing a flat gold surface and graphene together and

sandwiching molecules between them allows studies of whether the chemical enhancements can add to each other. This has been a long-standing question in the field owing to the fact that chemical enhancement alone is challenging to retain. In this sample geometry, the molecules are exposed to both substrates at the same time, which allows electrons transfer in both directions. As presented in Chapter 5, the surface enhancements from gold or graphene are vibration mode dependent - a feature of chemical enhancement - and the selected peak reveals that the combined effect of enhancement from flat gold and graphene is up to 68-fold, while GERS on mica only shows 7-fold. Here a sandwiched molecular junction with strong Raman scattering enhancement is experimentally realized and demonstrated. The results imply that upon exposing the desired molecule to two mainly chemical enhancement dominated substrates at the same time, the total chemical enhancements can be increased further. This facilitates the study of charge transfer in nano-objects with three-dimensional architecture and is also a milestone of studies on surface enhancement.

Based on the fact that chemical enhancements could be strengthened further in this sandwiched molecular junction, in Chapter 6 I applied TERS to investigate whether an additional enhancement can be induced and the enhancement bolstered further. Using TERS on graphene, a highly localized spatial resolution with a strong enhancement from the EM effect can be expected. Studies of TERS on graphene have revealed a great deal of nanoscale local information of graphene, such as nano-defects,[19, 20] edge boundaries[21] and local strains,[22, 23] etc. On the other hand, using graphene in TERS provides a high level of protection for molecules underneath from physical damage caused by a tip or chemical decay due to intensified thermal heating in the gap during laser illumination. Also, it helps to immobilize investigated molecules. The benefits between TERS and graphene are reciprocal.

Apart from the nanoscale resolution afforded by TERS that exceeds the diffraction limit, this technique also offers opportunities to study nanometer or subnanometer gaps in plasmonic materials in a well-controlled manner. It is known that metallic structures with nanogap features are highly effective building blocks for plasmonic systems, since the optical frequency can be widely tuned.[24] The resonant interaction between light and metallic nanostructures enables generation of localized electromagnetic fields at the subwavelength scale, as well as enhancement of optical absorption and scattering phenomena.[24] This enhancement can be approximately $\approx 10^4$-fold, and is increased with decreasing gap distance.[24] However, recent advances in theories and experiments show that this classical description failed to explain some phenomena happening as the gap distance enters the nanometer or

subnanometer regime.[25] Quantum mechanical effects influence the plasmonic resonances of nanogapped structures.[24] Therefore, precise engineering and control of nanogap distances is highly desired and this nano- or picocavities can serve as a basis for developing nanoscale nonlinear quantum optics at the single-molecule detection level.[26, 27]

Chapter 2

Theoretical background

2.1 Raman spectroscopy

When light interacts with matter, the photons may be absorbed or scattered, or may pass straight through it. Figure 2.1 shows the scattering processes. If the energy of an incident photon corresponds to the energy gap between the ground state of a molecule and an excited state, the photon may be absorbed and the molecule is excited to a higher energy. It is this change which is measured in absorption spectroscopy by the detection of the loss of that energy of radiation from the incident light, which for vibrational transitions is termed IR spectroscopy (Fig. 2.2). However, it is also possible for the photon to interact with the molecule and scatter from it. There are two kinds of scattering occurring: elastic and inelastic scattering. The elastic scattering, also called the Rayleigh process, is the most intense process since most photons scatter this way. It does not involve any energy change and consequently the photon retains the same energy. The inelastic scattering of light occurs when incident photons transfer energy to, or receive energy from, the molecule, changing the photon energy by one vibrational unit. It was first observed experimentally in 1928 by Raman and Krishnan.[28] In 1930, Raman won the Nobel Prize in Physics for his work on the scattering of light and for the discovery of the effect. Details of the principles of Raman scattering can be found in various textbooks[29-31] . Raman scattering may describe two kinds of processes (Fig. 2.1 and Fig. 2.2): Stokes and anti-Stokes.

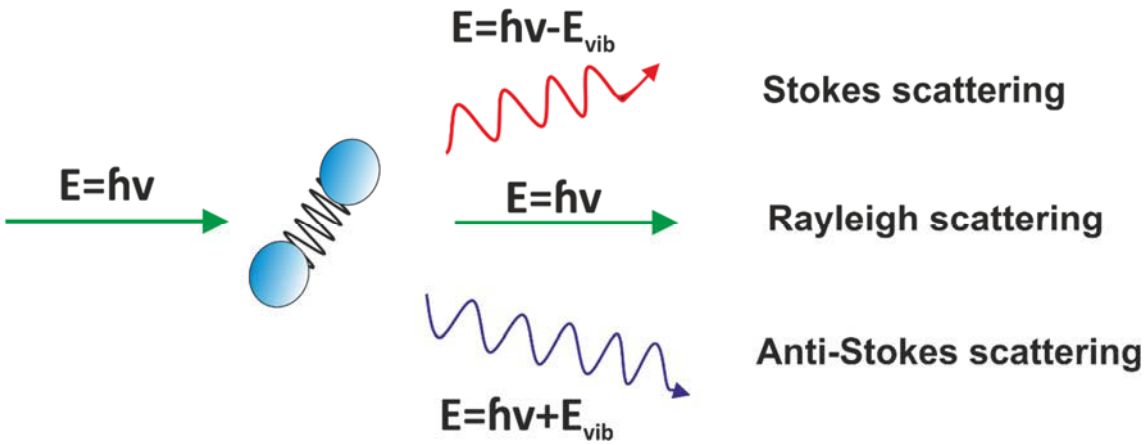

Figure 2.1 Schematic illustration of the Rayleigh and Raman scattering process. Figure based on from reference 29-31.

If the incident photon gives up energy to the sample, it is scattered with a redshifted frequency and referred to as Stokes Scattering. However, due to thermal energy, some molecules may be present in an excited state already, and transfer energy to the scattered photon. Scattering from these states to the ground state is called anti-Stokes scattering which involves a blueshift in the photon frequency.

Because the probability of a molecule being in an excited state is much lower than being in the ground state, the anti-Stokes shift occurs much less frequently than the Stokes-shift. In most cases, the Raman scattered photons collected and analyzed are the Stokes photons. Although the rarity of anti-Stokes photons results in much weaker anti-Stokes lines, they are sometimes favored in analysis due to the absence of fluorescence interference. This is because when there is fluorescence interference, it will occur at a lower energy than the excitation frequency and consequently anti-Stokes scattering can be used to avoid such interference.[31]

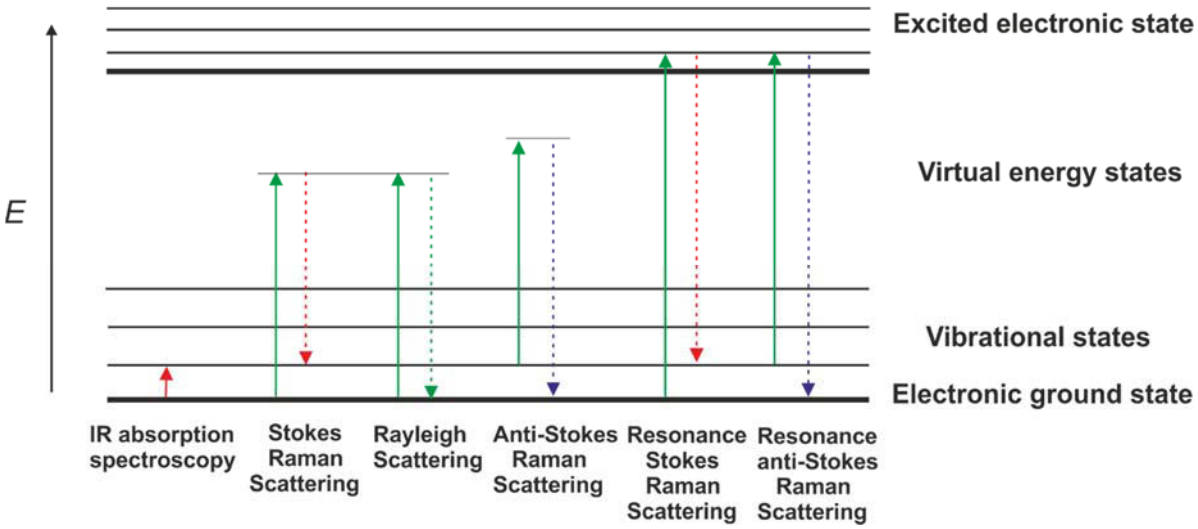

Figure 2.2 Diagram of the basic processes of resonance Raman scattering. (Figure based on reference 29, 32)

As mentioned above, infrared absorption would involve direct excitation of the molecule from ground state to another vibrational state by a photon matching exactly the energy difference between them, while Raman scattering uses much higher energy radiation and measures the difference in energy between two vibrational states by subtracting the energy of the scattered photon from that of the incident beam for Stokes scattering, or adding to it for anti-Stokes scattering. These phenomena result from the same type of quantized vibrational changes. However, IR relies on a change in the molecular dipole moment during

the vibration, whereas Raman requires a change in polarizability during the vibration. The following section follows the theoretical derivation by Ferraro et al.[30]

The change of polarizability can be expressed by the electrical properties of matter. First of all, the external electric field oscillates at the frequency of the incident radiation $\boldsymbol{v_i}$, and is described by

$$\boldsymbol{E = E_0 \cdot sin(2\pi v_i \cdot t)}$$

where $\boldsymbol{E_0}$ is the amplitude, and $\boldsymbol{t}$ is the time.

When the external radiation interacts with the electron cloud of a molecular bond, the induced electric dipole moment is defined by:

$$\boldsymbol{\mu = \alpha E = \alpha \cdot E_0 \cdot sin(2\pi v_i \cdot t)}$$

where α is a proportionality constant, called the polarizability of the bond.

In order to be Raman active, the polarizability (a measure of the deformability of the electron cloud by an electric field) of the bond must vary as a function of the distance between nuclei according to the equation:

$$\boldsymbol{\alpha = \alpha_0 + \gamma \cdot \left(\frac{\partial \alpha}{\partial \gamma}\right)_{\gamma_{=0}}}$$

where α_0 represents the polarizability at the equilibrium bond length, and

$$\boldsymbol{\gamma = \gamma_{max} \cdot sin(2\pi v_i \cdot t)}$$

With $\gamma_{\max}$ the maximum internuclear separation relative to the equilibrium separation.

Substituting the equation for polarizability into the initial equation for the dipole moment, one obtains an expression for the induced dipole moment:

$$\boldsymbol{\mu = \alpha E = \left(\alpha_0 + \gamma \cdot \left(\frac{\partial \alpha}{\partial \gamma}\right)_{\gamma_{=0}}\right) \cdot E}$$

$$\boldsymbol{= \alpha_0 + \left(\frac{\partial \alpha}{\partial \gamma}\right)_{\gamma_{=0}} \gamma_{max} \cdot sin(2\pi v_i \cdot t))\, E_0 \cdot sin(2\pi v_i \cdot t)}$$

Or:

$$\boldsymbol{\mu = \alpha_0 E_0 \cdot sin(2\pi v_i \cdot t) + 1/2 \left(\frac{\partial \alpha}{\partial \gamma}\right)_{\gamma_{=0}} \gamma_{max} \cdot E_0\, cos(2\pi(v_i + v_{int})t)}$$

$$\boldsymbol{+ 1/2 \left(\frac{\partial \alpha}{\partial \gamma}\right)_{\gamma_{=0}} \gamma_{max} \cdot E_0\, cos(2\pi(v_i - v_{int})t)}$$

The first term represents Rayleigh scattering, which occurs at the excitation frequency $\boldsymbol{v_i}$. The second and third terms correspond to the anti-Stokes frequencies of $(\boldsymbol{v_i + v_{int}})$ and

Stokes$(\boldsymbol{\upsilon_i - \upsilon_{int}})$, respectively. It is important to note that Raman scattering requires that the polarizability of a bond varies as a function of distance - that is (∂α/∂r) must be greater than zero if a Raman line is to appear.

The resulting Stokes intensity I_s of the radiation

$$I_S \propto \left(\frac{\partial \boldsymbol{\alpha}}{\partial \boldsymbol{\gamma}}\right)^2_{\boldsymbol{\gamma_0}} I_0 \left(\boldsymbol{\upsilon_i - \upsilon_{int}}\right)^4$$

Depends linearly on the intensity of the incident radiation, I_0, on the fourth power of the frequency of the scattered radiation and on the square of the derivative of the polarizability. It is inherently a weak process, in that only one in every 10^6–10^8 photons that scatter undergo Raman scattering. Therefore, intense incident radiation is necessary to obtain a detectable signal, unlike in IR spectroscopy.

2.1.1. Resonance Raman spectroscopy

Even though Raman scattering is a very weak process, there is one kind of Raman with tremendous enhancements often up to the order of 10^3 or 10^4, and it has also been observed up to 10^6, relative to off resonance Raman.[31] This is Resonance Raman, and it happens when the frequency of the laser beam is close to the frequency of an allowed electronic transition. Ideally, a tunable laser would be used for excitation and the frequency would be chosen to correspond exactly to the energy difference between the ground vibrational state and the first or second vibrational state of the excited state. This condition is shown in Figure 2.2. This technique is appealing because it allows detection from dilute samples and provides new information on the Raman bands, which was not obtainable from the ordinary Raman effect.[33]

2.1.2. Confocal Raman imaging

In Raman spectroscopy, the instrumentation consists of three major parts: light source, optical components and a Raman Spectrometer.[34] A continuous-wave fixed laser beam is used for excitation. A beam splitter, a set of optical mirrors, and polarizer included in the excitation compartment are used to divert the laser light into the sample compartment. Lastly, the Raman Spectrometer is usually a computerized single beam spectrophotometer. Automation makes sure that a software controlled step-motor positions the grating into the proper position perfectly. For analysis and detection of the collected light, spectrometers with interchangeable gratings and charge-coupled device (CCD) detectors are most frequently used.

The newest generation of electron-multiplying CCDs (EMCCD) offer high sensitivity, down to single photon counting, and fast readout rates (in the millisecond range). In order to suppress thermal noise, a liquid N_2- or Peltier-cooled CCD-camera yields sufficiently accurate results.

There are two kinds of filters to suppress the laser wavelength: notch filters and edge filters. Notch filters suppress mainly the laser wavelength, allowing for the detection of both Stokes and anti-Stokes Raman spectra. However, as in most applications, only the stronger Stokes lines are of interest, so less expensive edge filters are more frequently used.

Raman imaging is a technique allowing for imaging with the full spectroscopic information collected in every pixel. It can be accomplished by scanning a focused laser beam through a sample, either by laser scanning using mirrors and motorized objectives or by sample scanning through piezoelectrically driven stages.[34]

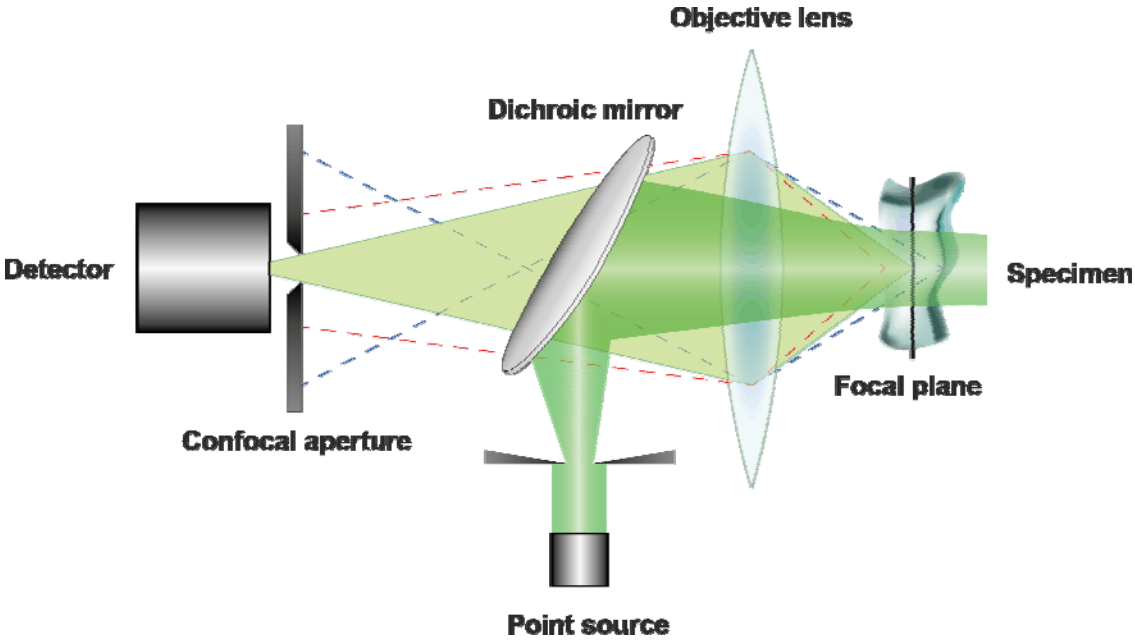

Figure 2.3 Scheme of the light path of a confocal microscope

Since Raman scattering is a weak process, the invention of confocal microscopy makes modern Raman imaging possible. This is realized by the addition of a confocal aperture. When an incident light source illuminates a single point on the focal plane of a specimen, the scattered light is channeled back through the objective lens and through a dichroic mirror. It then impinges upon the confocal aperture, which is located in the primary image plane of the objective. The confocal aperture allows all of the in-focus light from the region of interest on the sample to pass through to the detector, while the light coming from different depths in

the sample will be filtered (see Figure 2.3). As so little of this light gets through to the detector, it adds very little to the final image obtained. This increases the contrast of an image and the efficiency of a Raman signal from a point of interest, and therefore allows further study of surface scan (XY) or depth profiling (XZ). [35]

2.1.3. Surface-enhanced Raman spectroscopy (SERS)

When light illuminates on molecules placed in the proximity of nanostructured gold or silver substrates, the light scattered from the molecules is often amplified by factors of a million or even a billion. This is generally known as the surface-enhanced Raman scateering (SERS) effect. Since the first observation of unexpectedly high Raman signal intensities for pyridine molecules adsorbed on a roughened silver electrode in 1974 by Fleischman and his co-workers[5], SERS has been a continually advancing topic in research. It was first thought to be due to a large specific surface area of the electrode, allowing for a high surface coverage of pyridine molecules and thus increased the amount of observable molecules. Later in 1977, Jeanmaire & Van Duyne demonstrated that the anomalous enhancement in surface Raman spectra is due to a new effect.[36] They described that the fifty-fold increase in signal strength must account from not only an increase in surface area (which brought up ten-fold of signal strength), but also due to the formation of active sites during the anodization process. They conjectured the effect is from the electric field created at the surface during the electrochemical process. In 1978, Martin Moskovits proposed that the giant Raman intensity from a roughened Ag electrode originates from the excitation of surface plasmons (Fig. 2.4).[37] This helped to predict the enhancement dependency on excitation wavelength. Soon Creighton, Blatchford & Albrecht showed the first experimental evidence that the SERS enhancement effect can be observed on Ag and Au colloids in 1979.[38] The working principle of SERS is rooted therein. This amplification effect of SERS allows the detection and identification of very small amounts of molecules, even down to the single molecule sensitivity. [39, 40]

Despite the fact that SERS is a powerful and widespread technique, the understanding of SERS mechanisms has been a struggle since the early days of its life. At the time when only the normal Raman scattering cross-section was considered, the enhancement factor EF is known to be as large as 10^6.[41] There is a consensus among researchers that the effect arises from the collective electron excitations called surface plasmons that form at the nanostructured substrate's surface when light strikes the sample. However, exciting the

localized surface plasmon resonance of a nanostructured metal surface only gives an electromagnetic enhancement factor on the order of 10^4.

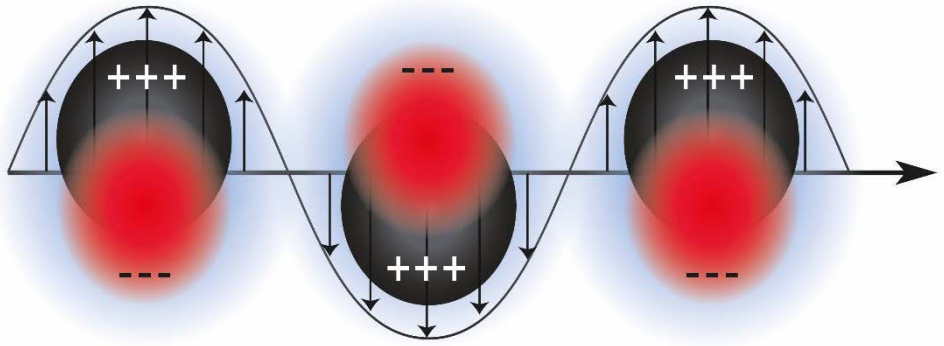

Figure 2.4 Working principle of SERS: Conduction electrons in nanostructured metals can be excited by incident light coherently to oscillate collectively; these surface plasmons can focus the light to a nanoscale near-field, thereby enhancing the local electromagnetic field intensity.

The magnitude of the local field $E_{loc}(v_0)$ outside the particle is described as follows,[34, 42]

$$E_{loc}(v_0) = gE_0 \,, \qquad (1)$$

where E_0 is the magnitude of the incident field and *g* is the field enhancement averaged over the surface of the particle. The induced electric dipole moment of a molecule in close proximity of the surface of the nanostructure will then be:

$$\mu = \alpha E_{loc} = \alpha g E_0 \,, \qquad (2)$$

Since the total Raman scattering intensity is proportional to $|\mu|^2$, the total scattering would be as follows

$$I \propto |\alpha|^2 \left| g g^{\prime} \right|^2 I_0 \,, \qquad (3)$$

Here it is assumed that the Raman scattered light gets enhanced the same way as the incoming light. But the corresponding field enhancement factor *g´* differs from *g* due to the difference in wavelength of the Raman scattered radiation. For low-frequency vibrational modes of adsorbed molecules, the values of *g* and *g´* are usually comparable. Therefore, the intensity scales with the fourth power of the local electromagnetic field enhancement.[7]

As a result, the researchers attribute the additional 10^2 enhancement to the chemical enhancement mechanism, which arises from the adsorption of molecules on the metallic surface. This then induces a modification of the electronic structure of the molecule either by the creation of a complex or by charge transfer between the molecule and the metallic surface. This results in a change of the polarizability of the molecule, and consequently in a change in the intensity of its Raman signal. To sum up, there are two mechanisms contribute to the major SERS effect: (1) a local EM enhancement occurs due to the large local fields generated by the surface plasmon resonances of nanostructures, and the nanostructures acting as an optical antenna to confine far-field light to the near-field (2) a chemical enhancement arises from charge transfer between the molecule and the metal, which alters the Raman polarizability and involves a resonance Raman-like process. [7, 43]

The SERS enhancement decays with $(1+d/r)^{-12}$ for a nanoparticle with radius r and the distance d of the molecule to the particles surface.

2.1.4. Materials and SERS

The EM enhancement of SERS arises from the resonance of the electronic excitation wave on the metal surface induced by the incident radiation. This resonance condition depends on the dielectric constant of the metal, which is also a complex function of the incident wavelength. The enhancement factor can be written as:[41]

$$EF = \frac{\varepsilon_{in} - \varepsilon_{out}}{(\varepsilon_{in} + 2\varepsilon_{out})}$$

ε_{in} is the dielectric constant of the metal nanoparticle, and ε_{out} is the dielectric constant of the external environment. The magnitude of the enhancement reaches a maximum when the denominator of EF approaches zero. Consequently, when the materials exhibit a negative value of the dielectric function at the wavelength of interest and a small absorption, they are good candidates as SERS materials. As a result, silver, gold and copper are widely used, good SERS materials. Among them, silver is the most enhancing and utilized because it has the smallest absorption in the visible range. Gold and copper have absorption at lower wavelengths, thus are limited to use as SERS substrates only at wavelengths above 600 nm. [44]

2.2 Graphene

Graphene is a two-dimensional (2D) atomic crystal allotrope of carbon, or a single layer of graphite. 2D crystals had been studied theoretically long before graphene appeared since subtracting one dimension from the 3D world can bring up a lot of fundamentally interesting phenomena. However, it was not believed to exist in nature because all 2D crystal structures were thought to be thermodynamically unstable. [45] The term "graphene", first coined in 1987, describes the single sheets of graphite as one of the constituents of graphite intercalation compounds.[46] Since 2004 scientists Andre Geim and Konstantin Novoselov developed the "Scotch-tape method", also known as the micromechanical cleavage technique, to exfoliate graphene from graphite for the first time. This simple and effective method triggered this research area growing extremely quickly and enormously.[47] In 2010, Andre Geim and Konstantin Novoselov were awarded the Nobel Prize in Physics for their ground-breaking experiments in making and investigating graphene in the real world.

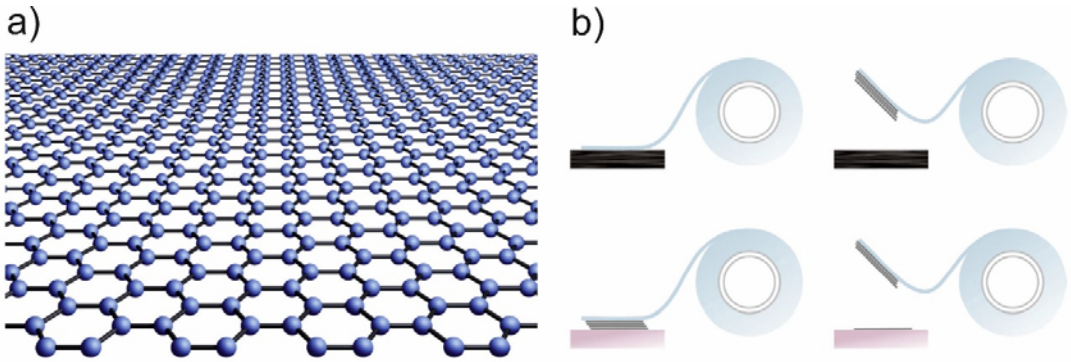

Figure 2.5 a) The crystal structure of graphene—carbon atoms arranged in a honeycomb lattice. b) The ''Scotch-tape'' method for producing graphene. Figure reproduced from refence 48 with permission. Copyright © 2011 WILEY-VCH Verlag GmbH & Co. KGaA, Weinheim.

Graphene is the first example of a 2D atomic crystal whose properties, from a physical point of view, are significantly different from those of the bulk form. It is the thinnest object ever obtained; the strongest material ever tested; and it is extremely electrically and thermally conductive, very elastic and impermeable to any molecules. It is also considered as a giant molecule, which provides numerous functional sites for chemical modification and surface modification.[49] Fig. 2.6 (a) shows the crystallographic structure of graphene including the unit cell with lattice vectors $\overrightarrow{a1}$ and $\overrightarrow{a2}$. The unit cell contains two atoms and the carbon-carbon distance is a_{cc} = 1.422 Å. Carbon atoms are densely bonded in a regular sp^2 hybridized

hexagonal pattern – a combination of orbitals s, p_x and p_y that constitute the σ-bond. The final p_z electron makes up the π-bond. The π-bonds hybridize together to form the π and π* bands. These bands are responsible for most of graphene's notable electronic properties, via the half-filled band that permits free-moving electrons. So graphene is a zero-band-gap semiconductor.

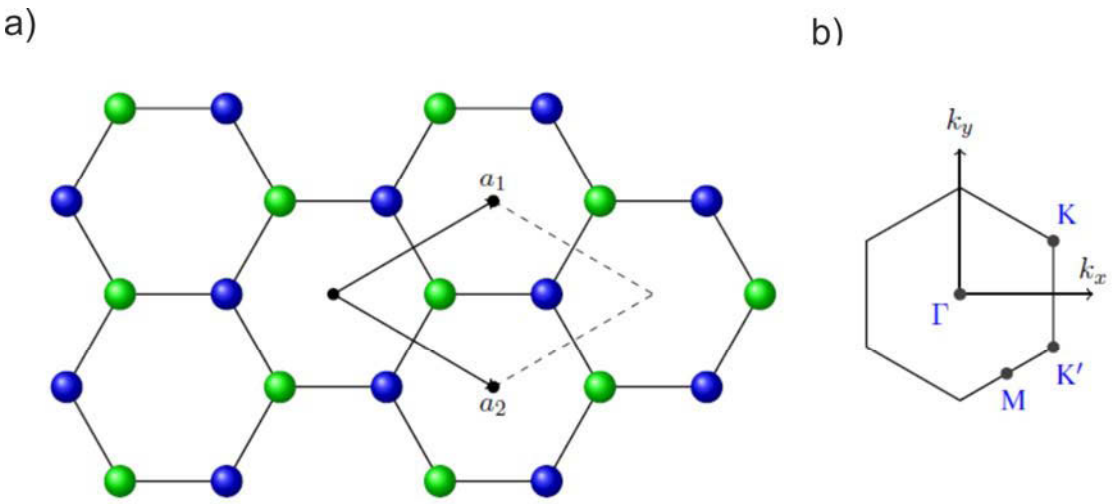

Figure 2.6 (a) Crystallographic structure of single layer graphene with the atoms of different sublattices marked with different colors. Unit cell of graphene with lattice vectors $\overrightarrow{a1}$ and $\overrightarrow{a2}$. (b) Brillouin zone of graphene with high symmetry points. The Γ point is in the zone center, the M point in the middle of two connecting hexagonal sides and the K and K' points are at the corners. Figure reproduced from reference 50.

This marvelous electronic property is what really makes graphene special, with its valence and conduction bands meeting at the K point of the Brillouin zone (Fig. 2.6 b)), which is associated with the Dirac point, as shown in Figure 2.7. In the vicinity of these points, the band structure exhibits an approximately linear energy dispersion.[49] [51] Thus, the electrons follow the Dirac equation at low wave vectors. It allows access to the rich and subtle physics of quantum electrodynamics in a relatively simple condensed matter experiment. The energy-momentum *(E - k)* dispersion relationship is linear for low energies near the 6 corners, which are associated with the positions of carbon atoms in the Brillouin zone. This results from the hexagonal symmetry of the graphene lattice, which has two atoms per unit cell and can be conceptualized as two interpenetrating triangular sublattices (referred to as A and B sublattices). The linear dispersion relation (Fig. 2.7 a) further suggests that the density of states in the valence and conduction bands are essentially described by the same wave function, such that the electron and hole transports in graphene field-effect transistor (FET) devices are

symmetric and ambipolar, as shown in Fig. 2.7 b. When the charge density n = 0, the Fermi energy coincides with the Dirac point, namely, with the charge neutrality point, and a zero density of states (DOS) is supposed to be obtained.

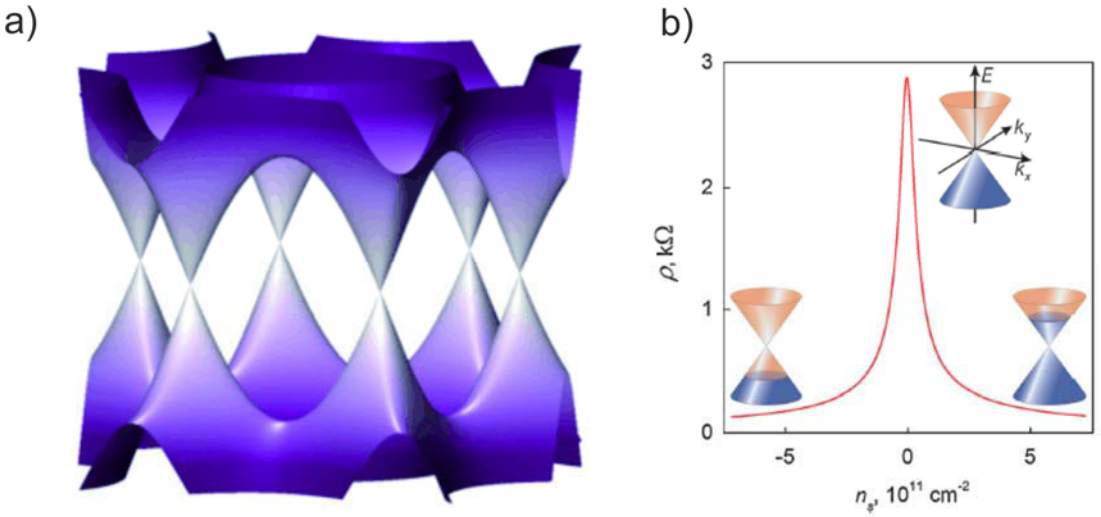

Figure 2.7 Electronic band structure and transport behavior of graphene. a) The low-energy band structure of graphene. (b) The experimentally measured transport characteristics of a representative graphene field-effect transistor shows symmetric, ambipolar behavior. Figures reproduced from reference 48 with permission. Copyright © 2011 WILEY-VCH Verlag GmbH & Co. KGaA, Weinheim.

In addition to its extraordinary electronic structure, as a consequence, graphene also shows intrinsic unique properties in optics. Graphene produces an unexpectedly high opacity for an atomic monolayer, absorbing a significant $\pi\alpha \approx 2.3\%$ fraction of incident white light, where α is the fine-structure constant and independent on material parameters.[10] The origin of its optical properties lies in the two-dimensional nature and gapless electronic spectrum, and experimental results also confirmed that the opacity is practically independent of wavelength. Furthermore, the opacity is found to increase with membrane thickness so that each graphene layer adds another 2.3%. [10, 49]

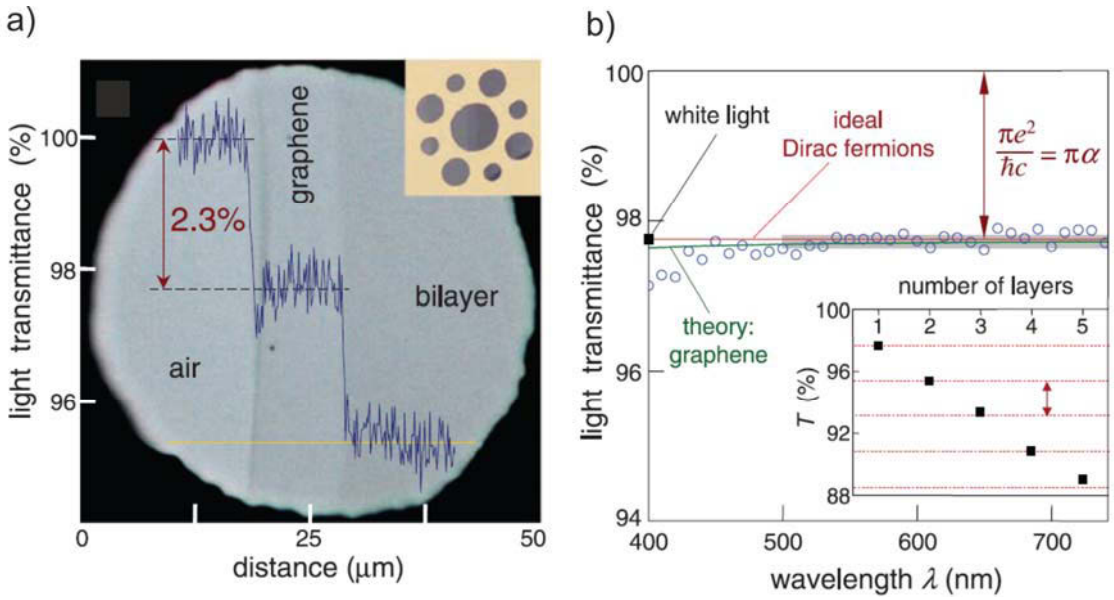

Figure 2.8 Looking through one-atom-thick crystals. a) Photograph of a 50-mm aperture partially covered by graphene and its bilayer. The line scan profile shows the intensity of transmitted white light along the yellow line. b) Experimental transmittance of white light of a suspended graphene layer measured by Nair et al.[10] And transmittance as a function of the number of graphene layers (squares). Figure reproduced from reference 10 with permission. Copyright © 2008, American Association for the Advancement of Science

The optically broad absorption of graphene nanoribbons spans from the ultraviolet (UV) region through the visible to the far-infrared and gives an ultrafast response time. It is also reported that the optical response of graphene is tunable into the terahertz regime by an applied magnetic field.[52] This marvelous property makes graphene a promising solution to the increasing ongoing quest of controlling light in tiny circuits and suppression of losses. That is, to squeeze light and propagate it through nanoscale electronic building blocks. Optical circuits and devices provide signal processing and computing much faster, but the propagating light needs a realatively large amount of space (at least half its wavelength). The emerging graphene plasmon materials show that the wavelength of light captured by it can be strongly shortened by a factor of 10 to 100 compared to light propagating in free space.[53,54] As the light propagating along the graphene layer is strongly confined, it fits into the desire of nanoelectronics nowadays.

2.2.1. Micromechanical cleavage

The simplest method to isolate 2D materials is to exfoliate their parent bulk materials into individual layers. For example, high-quality (nearly single-crystalline) graphite typically requires a growth temperature over 3,000 K, while the exfoliation can be carried out at room temperature. Performing the exfoliation procedure is like our daily-life experience in using a pencil, since drawing with a pencil essentially involves exfoliation of graphite. The conventional techniques that exfoliate these materials, however, do not allow exfoliation to reach monolayer limit. The true breakthrough to isolate large-area monolayer sheets was first made by Novoselov et al.,[47] and is known as the Scotch-tape method as shown in Fig. 2.5. When the adhesion of the bottom layer (the layer in touch with the substrate) to the target substrate is sufficiently strong to overcome the interlayer interactions, a layer of 2D material can be transferred onto the substrate, producing extremely high-quality 2D crystals. This technique also suggests that when the 2D material considered has a stronger interlayer interaction (or higher surface tension), it becomes more difficult to obtain monolayer sheets using this method, e.g. MoS_2. [55]

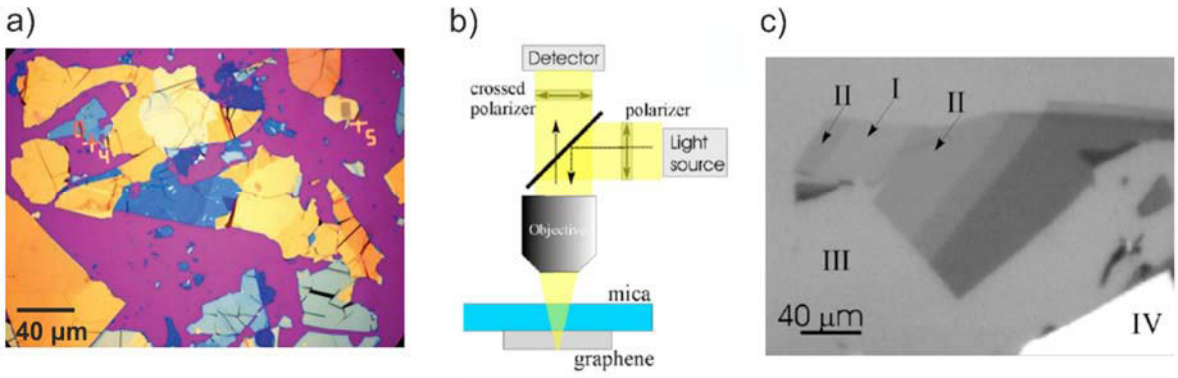

Figure 2.9 a) Thin graphitic flakes on a surface of Si=SiO_2 wafer (300 nm of SiO_2, purple color). The different colors correspond to flakes of differing thicknesses. b) Schematic of optical detection setup for exfoliated graphene on mica. The sample is imaged in reflection using a Zeiss Axioskop with a 20x objective. Illumination was carried out with light from a 50W halogen lamp passed through a linear polarizer. Light reflected from the sample was passed through a crossed linear polarizer [56]. c) Optical micrograph of graphene flakes of different thicknesses on a mica substrate. Monolayer (I) and bilayer (II) graphene appear darker than mica (III). Figure a) adapted with permission from reference 48. Copyright © 2011 WILEY-VCH Verlag GmbH & Co. KGaA, Weinheim b) and c reproduced from reference 56 with permission by AIP Publishing LLC through Copyright Clearance Center.

Even though it is a simple method, it was extremely difficult to identify the single layer graphene in the first early experiments due to this very small scale and low yield process. The development of finding graphene on Si/SiO_2 (with a 300 nm SiO_2 layer)[47], which provides an optical contrast of up to 15% for some wavelengths of incoming light was revolutionary. However, with the aid of tape to press graphite flakes to any arbitrary substrate, it also brings some contamination and influence to the surface. A later evolved method called the ”tape-free” method - bringing graphite flakes onto the desired surface and removing the extra layers with tweezers[57] or simply rubbing a fresh surface of a layered crystal against another surface (similar to “drawing by chalk on a blackboard”) [58]- results in the most clean quality of graphene. An optical method of identifying graphene on transparent mica emerged later, allowing scientists to diversify the substrate support of graphene whilst identifying graphene layers by means of the optical reflection mode (Fig. 2.9 b). This imaging of single graphene on the bottom of a bare transparent substrate such as mica provides a high contrast of more than 12% for visible light. It can be explained with the destructive interference of light reflected from the substrate-graphene and graphene-air interfaces. Fig. 2.9 c) shows the different thicknesses of graphene reflect different amount of light under a microscope.

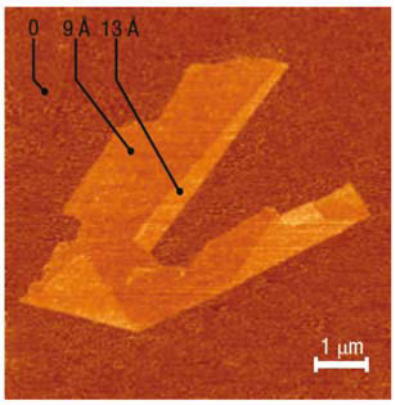

Figure 2.10 An SFM image shows micromechanically cleaved graphene on an oxidized Si wafer (300 nm SiO_2) Note that 2D crystallites were often raised by an extra few angstroms above the supporting surface, probably because of a layer of absorbed water. In such cases, the pleated and folded regions seen on many SFM images and having the differential height matching the interlayer distance in the corresponding 3D crystals help to distinguish between double layer crystals and true single sheets such as those shown here. Figure reproduced from reference 58 with permission. Copyright (2005) National Academy of Sciences.

2.2.2. Chemical vapor deposition (CVD)

Chemical vapor deposition (CVD) is a controlled chemical process that grows solid thin films on specific substrates from gaseous reactants, representing the most promising route to synthesizing 2D materials on a large scale. The primary method of growing graphene with CVD involves catalytic reactions of methane under hydrogen on copper or nickel (Fig. 2.11 a). [59-61] An important feature of CVD-grown graphene is that it enables large-scale transfer onto arbitrary substrates. As shown in figure 2.11, the transfer process involves spin coating the as-grown graphene with a sacrificial layer of polymer (often poly(methyl methacrylate), or PMMA), followed by removing the underlying metal using an etching solution. The plastic film, with graphene attached, can therefore be transferred onto the target surface (in this case, the TEM grid).

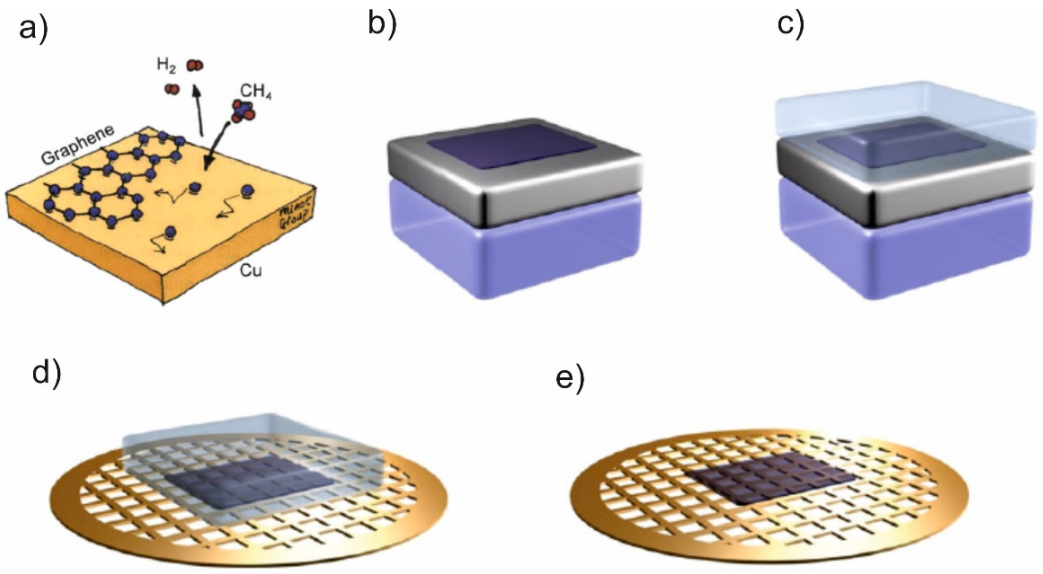

Figure 2.11 Chemical vapor deposition of graphene and the transfer process. a) Schematic of the catalytic process of CVD grown graphene on copper foil. Figure adapted from reference 62. (b) The as-grown graphene on a catalytic metal thin film. c) Spin-coating a sacrificial layer of polymer onto the substrate. d) After removing the bottom metal layer, the entire plastic film, with graphene attached, is transferred to the TEM grid. e) Upon removal of the sacrificial plastic layer. Figure adapted from reference 49 with permission. © 2011 Nobel Foundation, Published by The American Physical Society

2.2.3. Other methods

Although the exfoliation of 2D materials using the micromechanical cleavage method can provide high-quality monolayer sheets, it suffers from low yield and throughput. In addition to the CVD method, other possible solutions are under development. Liquid-Phase

Exfoliation[63] involves exfoliating and dispersing the bulk 2D materials in specific solvents or surfactant aqueous solutions in the presence of ultrasonic waves, thereby producing large quantities of dispersed nanosheets. This strategy is similar to the widely used ways of dispersing quantum dots and single-walled carbon nanotubes. The choice of the surfactant and the solvents depends on its surface energy relative to that of graphene, which is the key to managing this process. In 2008 liquid phase exfoliation of layered materials including graphene by using efficient solvents N-methyl-pyrrolidone was first reported.[63] In 2013 diverse layered materials such as MoS_2 and WS_2 exfoliated in the liquid phase were also obtained. [64]

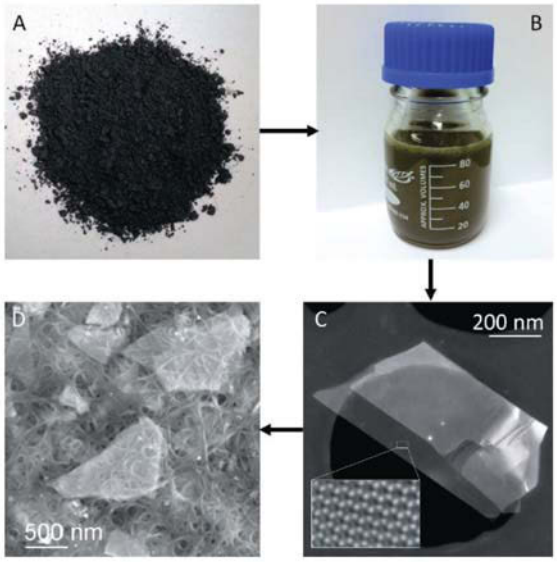

Figure 2.12 Liquid exfoliation of layered crystals allows the production of suspensions of two-dimensional nanosheets, which can be formed into a range of structures. (A) MoS_2 powder. (B) WS_2 dispersed in surfactant solution. (C) An exfoliated MoS_2 nanosheet. (D) A hybrid material consisting of WS_2 nanosheets embedded in a network of carbon nanotubes. Figure reproduced from reference 64. Copyright © 2013, American Association for the Advancement of Science.

Although micro cleavage and CVD growth methods can produce graphene with a relatively perfect structure and excellent properties, the chemical method of graphene production, reduction of Graphite Oxide, also attracts certain research interest due to two important characteristics: (1) it can be produced using inexpensive graphite as a raw material by cost-effective chemical methods with a high yield, and (2) it is highly hydrophilic and can form stable aqueous colloids to facilitate the assembly of macroscopic structures by simple and cheap solution processes, both of which are important to the large-scale production of graphene. [65, 66]

2.3 Raman spectroscopy of graphene and graphene layers

Even though the graphene can be prepared easily via mechanical exfoliation, the identification and counting of graphene layers is a major hurdle. Monolayers are only present as a small minority amongst all of the exfoliated flakes. Graphene is often only visible under an optical microscope when it is deposited on oxidized Si substrates (typically, 300 nm SiO_2) or by the special use of back light reflection from transparent mica.[56] SFM is an alternative way to characterize single and few layers, but it is time consuming. Moreover, the obtained single layer thickness is unreliable in height due to different surface properties between graphene and the substrate. [67]

Raman spectroscopy emerged and appeared to be an exclusive solution to identify graphene on the various substrates as the electronic structure of graphene can be uniquely captured in its Raman spectrum. It is capable of differentiating single, double and few layers of graphene, since the G and 2D Raman peaks change in shape, position and relative intensity with the number of graphene layers. Figure 2.13 a) plots the first-phonon Brillouin zone of graphene and figure 2.13 b) plots the optical phonon dispersions of single layer graphene (SLG). There are two atoms per unit cell, thus six normal modes (two being doubly degenerate) at the Brillouin zone center **Γ** : $A_{2u} + B_{2g} + E_{1u} + E_{2g}$ (Fig. 2.13 b). There is one degenerate in-plane optical mode, E_{2g} (Raman active) and one out-of-plane optical mode B_{2g} (Raman and IR inactive). The G peak corresponds to the high-frequency E_{2g} phonon at **Γ**, and represents the bond stretching of all pairs of sp^2 atoms in rings. The D peak with a frequency of approximately 1350 cm^{-1} results from the breathing modes of rings (Fig. 2.13 c), and requires a defect for its activation. Figure 2.13 e) shows the comparison of Raman spectra of pristine and defected graphene. The D peak is active by double resonance, and is strongly dispersive with excitation energy (Fig. 2.13 g). A very prominent feature to distinguish single layer graphene from few layer graphene is the 2D peak since it is very sensitive to the stacking order along the perpendicular direction. The 2D peak is the overtone of the D peak. Because its origin lies in a process where momentum conservation is satisfied by two phonons (TO) with opposite wave vectors, no defects are required for its activation. The intensity is stronger than that of the G peak due to the double resonant process and enhanced electron-phonon coupling. A G* peak in the vicinity 2450 cm^{-1} also stems from a double resonant process, but involves a transverse optical (TO) and a longitudinal acoustic (LA) mode. There is also a peak, the C peak (Fig. 2.13

f), reflecting the number of layers, but it is limited by instrumentation since many notch and edge filters cut off here.[68, 69]

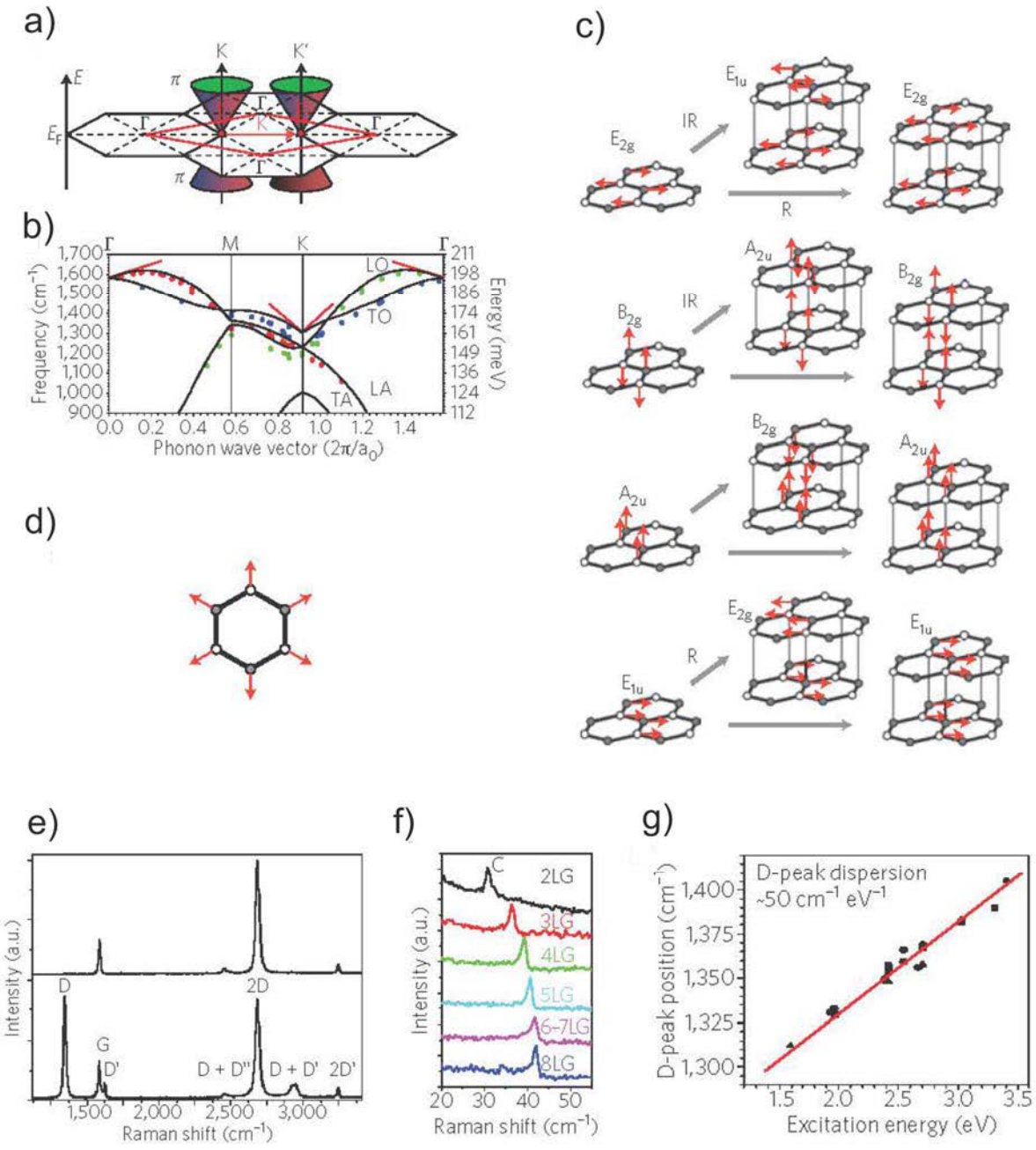

Figure 2.13 Electrons, phonons and Raman spectra of graphene. a) Electronic Brillouin zones of graphene (black hexagons), and electronic dispersion (Dirac cones). b) The black curves represent the dispersion of in-plane phonon modes in graphene in the energy and frequency range relevant for Raman scattering. The red lines represent Kohn anomalies. c) Γ-point phonon-displacement pattern for graphene and graphite. Grey arrows show how each phonon mode in graphene gives rise to two phonon modes of graphite; IR and R labels show IR-active and

Raman-active modes, respectively. Unlabelled modes are inactive. d) Atom displacements (red arrows) for the A_{1g} mode at K. e) Raman spectra of pristine (top) and defective (bottom) graphene. The main peaks are labelled. f) C peak as a function of number of layers (g) D-peak position as a function of excitation energy. Figure adapted from reference 68.

The 2D peak is a very prominent feature to characterize single layer graphene from few layer graphene since it is very sensitive to the stacking order. Figure 2.14 a) shows the two intense peaks of graphene and graphite, and its peak ratio drastically changed, b) shows a significant change in the shape and intensity of the 2D peak of graphene compared to bulk graphite, where a single Lorentz peak evolves to two components $2D_1$ and $2D_2$. Figure 2.14 c) and d) plots the evolution of the 2D band as a function of the number of layers at 514.4 and 633 nm excitations. It indicates that with the increase of layer numbers, the 2D peak is upshifted and broader with respect to graphene. Indeed, e) shows the 2D peak of bi-layer graphene can be broken down to four components.[70]

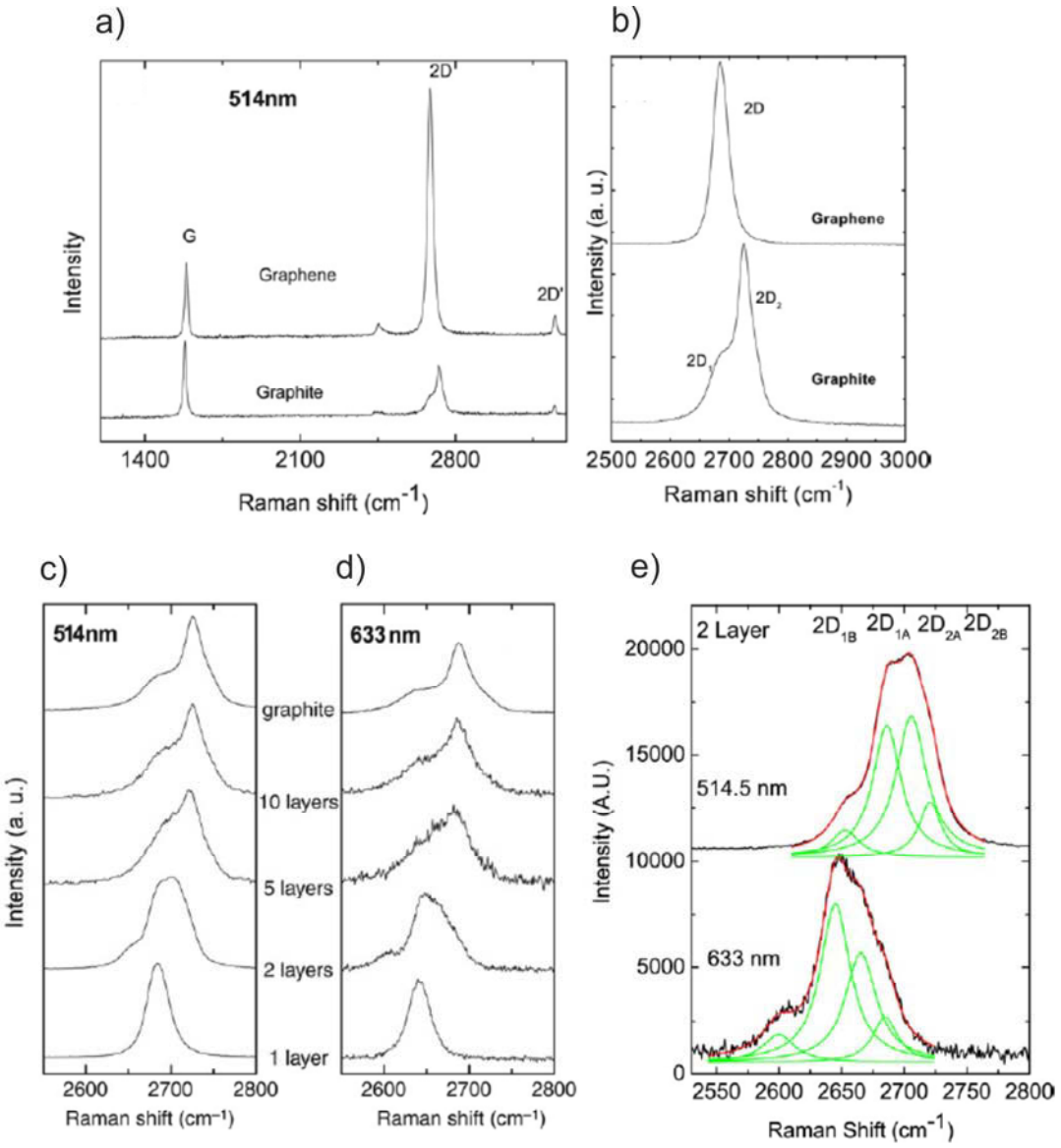

Figure 2.14 (a) Comparison of the Raman spectra of graphene and graphite excited at 514.5 nm, (b) comparison of the 2D peaks in graphene and graphite, (c) and (d) evolution of the 2D peak as a function of number of layers for 514 and 633 nm excitations, and e) the four components of the 2D peak in bi-layer graphene. Figure adapted from reference 70. Copyright © 2007 Elsevier Ltd.

2.3.1 Doping

The ability to control dope *n* or *p* doping is key to fabricating graphene devices. Raman spectroscopy also allows the quantification of strain and doping in graphene. It is reported that the G peak position increases and FWHM(G) decreases for both electron and hole dopings. (Fig. 2.15 and Fig. 2.16 a and b). The stiffening of the G peak is due to the nonadiabatic removal of the Kohn anomaly at **Γ**. The FWHM sharpening is due to blockage of the phonon decay into

electron-hole pairs due to the Pauli exclusion principle, when the electron hole gap becomes higher than the phonon energy. [71] FWHM(G) sharpening saturates when doping causes a Fermi level shift bigger than half the phonon energy. Meanwhile, the 2D peak can also be used to assign *p* or *n* doping, which upshifts for *p*-doping and downshifts for *n*-doping. Figure 2.16 d) plots the variation of the intensity ratio of the G and 2D peaks (I(2D)/I(G)) as a function of doping. It exhibits a clear dependence on the electron concentration, and can therefore be used to monitor the level of doping in graphene-based devices. While figure 2.15 and 2.16 also show that the position of the G peak and I(2D)/I(G) vary with the doping density, it is noted that these two parameters should not to be used to estimate the number of graphene layers. To conclude, it is the shape of the 2D peak that is the most effective way to identify a single layer.

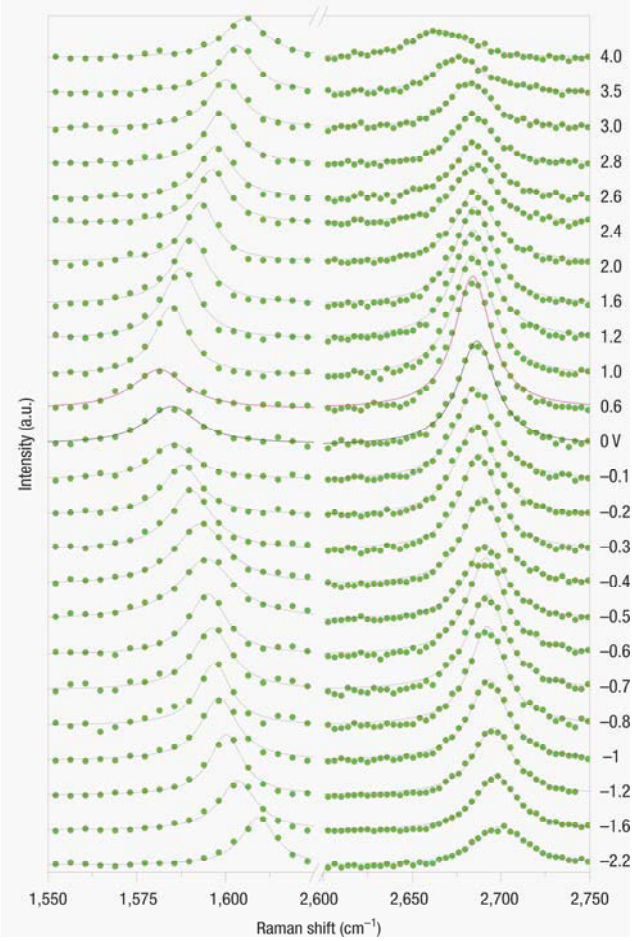

Figure 2.15 Raman spectra of graphene as a function of gate voltage between -2.2 V and +4.0 V. The dots are the experimental data, the black lines are fitted Lorentzians, and the red line corresponds to the Dirac point. The G peak is on the left and the 2D peak is on the right. Figures reproduced from reference 72 with permission. Copyright © 2008, Nature Publishing Group.

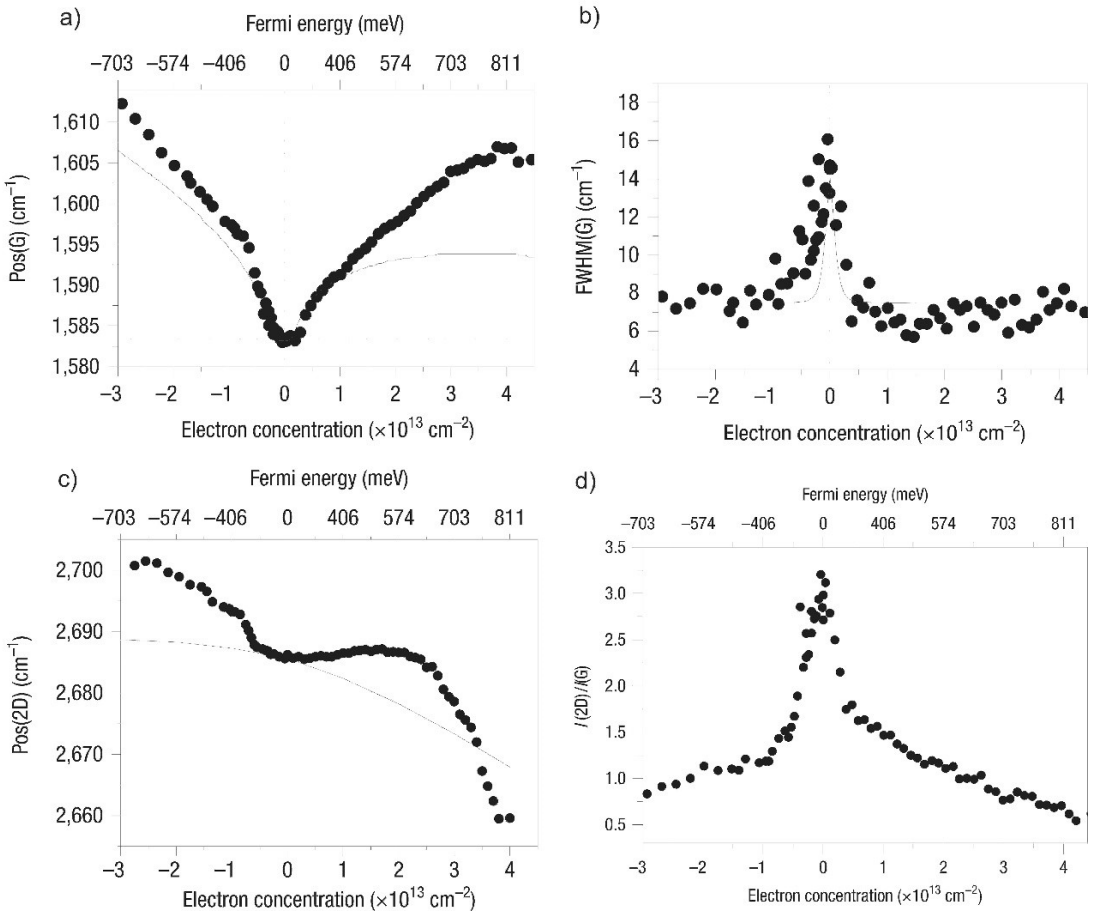

Figure 2.16 a) Pos(G) and b) FWHM(G) as a function of electron and hole doping. The solid blue lines are the predicted non-adiabatic trends from [73] c) Pos(2D) as a function of doping. The solid line is adiabatic DFT calculation. d) The influence of hole and electron doping on the 2D and G peaks. Figures reproduced from reference 72 with permission. Copyright © 2008, Nature Publishing Group.

2.4 Graphene-enhanced Raman scattering (GERS)

Graphene, as an atomically flat, chemically inert material with unique electronic properties, provides a flat platform on which to study Raman enhancement. The discovery of graphene-molecule interactions can be traced back to 2009, when Xie et al. observed that the spectral behavior of molecules changed when rhodamine 6G (R6G) and protoporphyrin IX (PPP) were put on a graphene surface. Since graphene is a good electrical conductor, the fluorescence quenching effect for minimal R6G adsorbed on graphene was found to be substantial and an estimated quenching factor on the order of 10^3 was reported (Fig. 2.17). [74] The subsequent year, Ling et al. observed many unexpected bands of mechanically exfoliated graphene when it is treated with organic solvents.[75] It was then speculated that graphene might have a Raman enhancement effect for the trace amount of residue matter. A systematic study with popular SERS probes, phthalocyanine (Pc), R6G, PPP, and crystal violet (CV), were therefore implemented (Fig. 2.18). The Raman enhancement factors were also reported as being quite different for different peaks, changing from 2 to 17. The enhanced efficiencies are dependent on the number of graphene layers.[75]

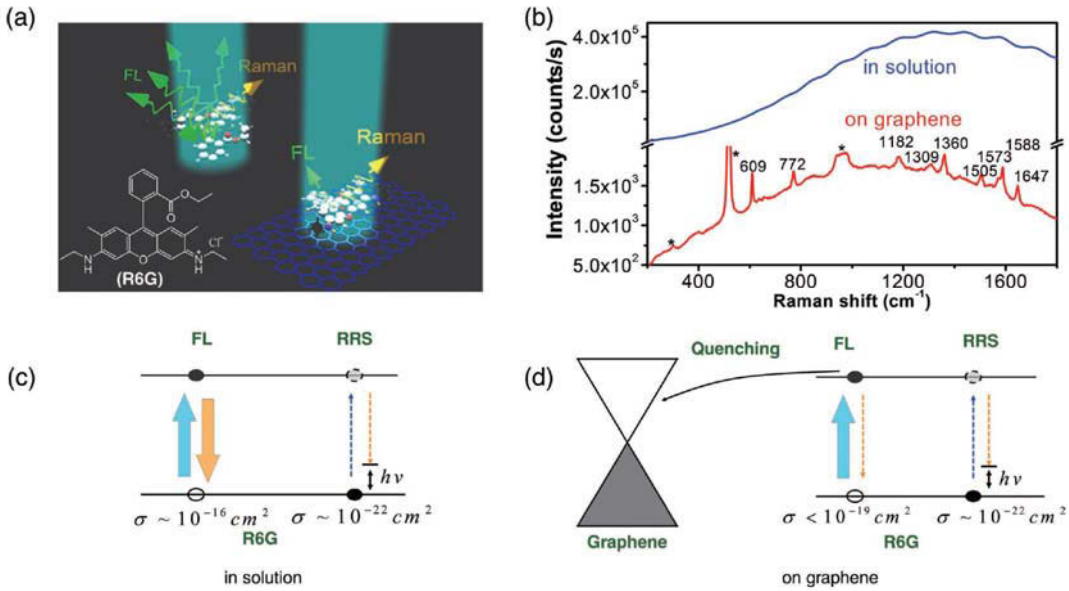

Figure 2.17 The fluorescence quenching effect of molecules adsorbed on graphene. a) Schematic diagram of graphene as a substrate for quenching fluorescence of R6G molecules. b) Comparison of Raman spectra of R6G in water (10 μM) and on a single layer of graphene at 514.5 nm excitation. "∗" marks the Raman signals of the SiO_2 /Si substrate. c,d) The estimated photoluminescence cross-section of R_6G in solution and on graphene, respectively. Reprinted with permission from reference 74, 76. Copyright (2009) American Chemical Society.

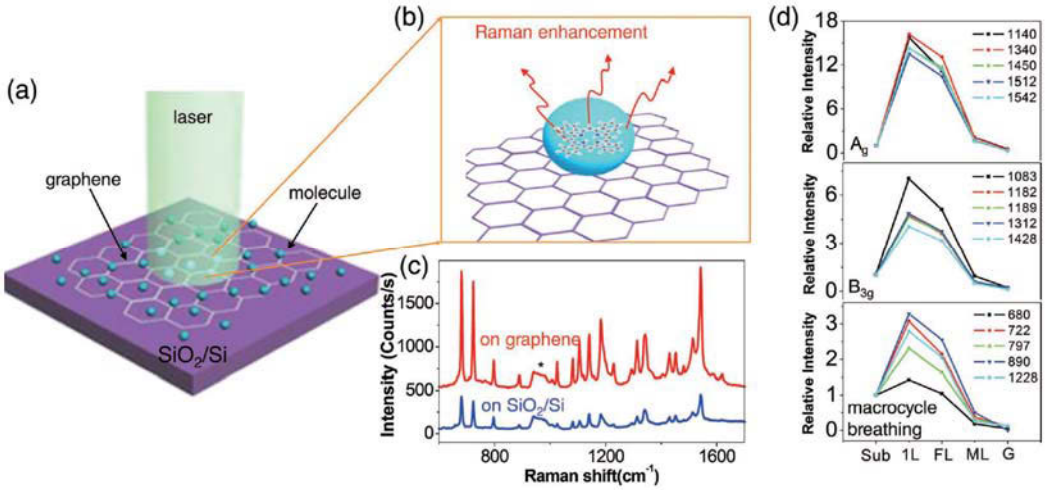

Figure 2.18 The GERS effect. a,b) Schematic illustration of the molecules on graphene and a SiO_2/Si substrate, and the Raman experiments. c) Comparisons of Raman signals of phthalocyanine (Pc) deposited on graphene (red line) and on the SiO_2/Si substrate (blue line) using vacuum evaporation at 632.8 nm excitation. "∗ " marks the Raman signals of SiO_2/Si substrate. d) The relative Raman intensity of Pc deposited on different surfaces using vacuum evaporation. The different spectral lines represent the different peaks of Pc labelled in the right top corner. The signals on the SiO_2/Si substrate are set to "1". Reprinted with permission from reference 9, 75. Copyright (2010) American Chemical Society

As a recently emerging material for use as a surface enhanced Raman scattering substrate, graphene helps to resolve the over decades debated issues regarding SERS mechanisms, where the chemical enhancement mechanism (CM) and electromagnetic mechanism (EM) operate multiplicatively, and CM is usually covered up by the strong EM. The synergistic action of graphene in SERS provides a new pathway to understand the SERS mechanism. Since the optical absorption of graphene is only 2.3% and the intrinsic graphene plasmon is in the THz frequency region that is far from visible, the current consensus is that the GERS effect is considered to be lacking an EM contribution. Following the large number of studies on GERS, it is well accepted in the scientific community that GERS mainly relies on the chemical mechanism. A series of experiments were designed in order to gain better understanding of CM theories, including the first layer effect,[77] Fermi level modulation,[78] wavelength-scanned experiments in GERS,[17] and surface selection rules.[79]

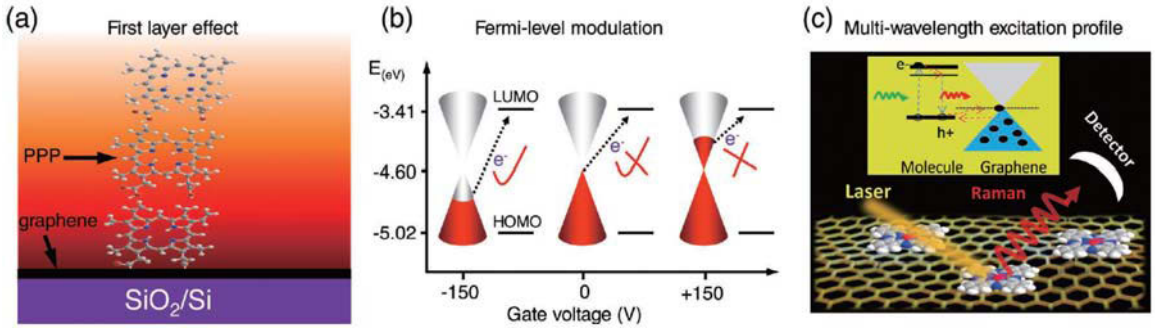

Figure 2.19 Chemical mechanism based features of GERS. a) First layer effect in GERS. Reproduced with permission.77 Copyright 2010, Wiley-VCH. b) Fermi-level Reprinted with permission from reference 78. Copyright (2011) American Chemical Society modulation of GERS. c) Wavelength-scanned excitation profile of GERS. Reprinted with permission from reference 17. Copyright (2012) American Chemical Society.

The close distance effect experiment was carried out with ordered PPP molecules prepared by the Langmuir–Blodgett (LB) technique. Samples with mono- and multi- layers of PPP adsorbed on SLG were investigated to verify the short-range effect, which is a known feature for CM (Fig. 2.19 a).[77] The results show that 1) the Raman enhancement is greater in the first layer, and almost no observable additional enhancement is observed beyond the third layer; 2) the Raman enhancement is dependent on the molecular configuration in contact with graphene, in which the functional group of PPP in direct contact with graphene has a stronger enhancement than other groups. These are two widely used indications for CM.

The underlying mechanism of CM is generally believed to be the photoinduced metal-molecule charge-transfer (CT) model, and the enhancement is related to the Fermi level of the substrate. There are two requirements in this regard; one is direct contact between the probe molecule and the substrate, thus the CT process occurs only for the first layer of molecules on the SERS substrate, and the other is energy alignment between the molecular energy level (HOMO, LUMO) of the molecules and the Fermi level of the substrate. Herein tuning the position of the Fermi level of graphene using an external voltage source can, in principle, drive the entire system in and out of CT resonance. A series of metal phthalocyanine (M-Pc) molecules (M=Mn, Fe, Co, Ni, Cu, Zn) with different molecular energy levels were used as probe molecules and their GERS enhancement performance under different gate voltages were investigated (Fig. 2.19 b).[78] The results show that the Raman intensities of all these M-Pc molecules become weaker when the graphene Fermi level is up-shifted by applying a positive gate voltage, while they become stronger when the graphene Fermi level is down-shifted by applying a negative gate voltage. [78]

In addition to the Fermi level tuning of the substrate, the CT mechanism based GERS can also be influenced by the energy of the incident laser light. The Raman excitation profiles of GERS were obtained in the range of 540-660 nm. The results suggest the charge transfer in GERS to be a ground state charge transfer mechanism since the profiles were fitting well with the function of the normal Raman intensity under resonant condition, but no excited state charge transfer resonance was observed in the profiles.[17]

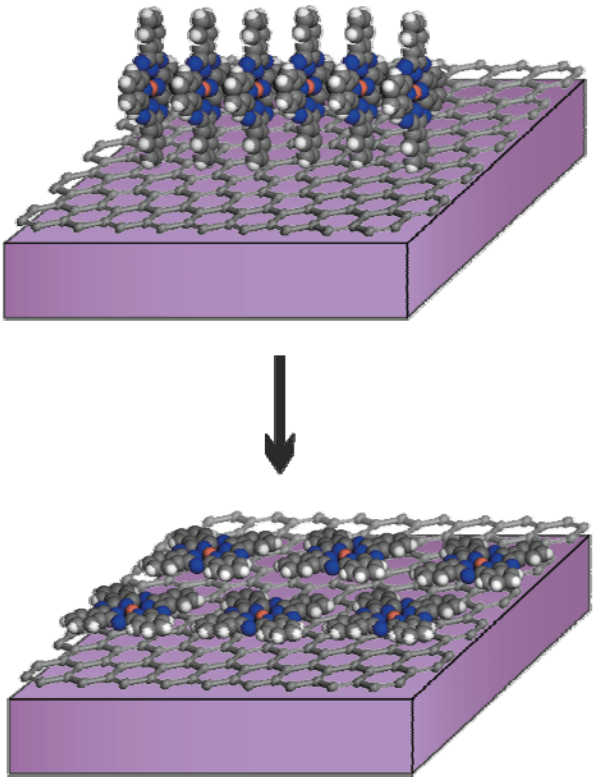

Figure 2.20 Schematic illustration of molecular orientation changes relative to the graphene surface. (Molecule: CuPc).

Besides the energy level matter, the molecular orientation dependence was also investigated in GERS. With the aid of the LB technique and annealing, upstanding and flat-lying molecular orientations were prepared.[14] GERS was found to be highly dependent on the molecular orientation, with a much larger enhancement for the flat-lying molecular orientation (Fig. 2.20). The chemical enhancement factors of the different vibrational modes in CuPc were calculated by comparing the different molecular orientations.[14] Additionally, two classes of different molecules with either similar molecular geometries or molecular energy levels were chosen to investigate the molecular selectivity of GERS. The studies suggest that a remarkable GERS enhancement requires strong molecule−graphene coupling to give effective

charge transfer between the molecules and graphene. These results showed promise to evaluate the interaction between graphene and the molecules.

2.5 Tip-enhanced Raman spectroscopy (TERS)

According to Abbe's theory developed in 1873[1, 80], the resolving capability of an optical object is ultimately limited by light diffraction, and expressed by the Rayleigh criterion:

$$d = \frac{0.61\lambda}{NA}$$

where λ is the wavelength in vacuum, and NA is the numerical aperture for the optical object. This formula indicates the resolution is limited to 200-400 nm for the range of visible light with highest NA objectives.

Later the near-field concept was conceived and developed gradually over one hundred years to yield subdiffraction spatial resolution. Synge in 1928 proposed the idea of using a very small aperture (well below the optical diffraction limit) placed very close to a sample surface, and rastered over a surface while illuminated, acting as a near-field light source.[81] This would result in obtaining images with sub-diffraction limit spatial resolution. It is also the beginning of the concept of "scanning near-field optical microscopy" (SNOM).[82] This concept further developed by Wessel in 1985, who suggested combining a single metal nanoparticle with a scanning probe microscope that could be rastered over a surface. The experimental realization was achieved in 2000, where a technique known as "Tip-enhanced Raman spectroscopy" (TERS) was demonstrated independently by the Anderson[83], Kawata[84], Pettinger[85] and Zenobi[86] groups. With the aim of realizing ultrahigh spatial resolution and circumventing the problems of SERS, TERS has developed its own important applications in nanoscale chemical analysis within 16 years such as for carbon nanotubes, graphene, polymers and biomolecules. In general, the tip is prepared from a plasmonic Au or Ag material with a radius of about 10-50 nm and illuminated with a focused laser; the surface plasmons can thus be excited at the tip apex acting as a nanoanntena. The tip is then brought into the vicinity of the substrate of interests and regulated by the feedback control (SFM or STM principle).[87] An enhanced electromagnetic field at the tip is generated that causes enhanced local incident and radiated fields, and thus significantly increased Raman signals of the molecules underneath the tip. The technique holds the outstanding features of *simultaneously* acquiring spectroscopic information and topographical features below the optical diffraction limit. Although there are many analytical tools which can characterize the surface morphology of materials with atomic

resolution, it remains challenging to investigate the chemical composition and surfaces structures at the same time.[7]

Regarding the spatial sensitivity of TERS, the enhanced field is highly localized to the tip apex, and therefore it offers the local chemical information at a spatial resolution of about 10 -15 nm.[88-90] This, however, under specific conditions, can reach very high sensitivity down to single molecules[26, 91-94] or even submolecular[95]. It was indicated that when the well-confined nanocavity plasmon between tip and metallic surface matches the molecular vibronic transitions, subnanometer resolution can be achieved. It was also further confirmed theoretically that the optical transition matrix of a molecule is dependent on the position and spatial distribution of the plasmonic field. It is necessary to point out that, in contrast to SERS, TERS offers only one hot spot for Raman enhancement, hence its detection sensitivity is much lower than that of SERS. Moreover, since the tip and the probe molecules are not in contact, only electromagnetic enhancement is considered to be the mechanism.

2.5.1 Geometry

With the development of TERS over a decade, the configuration of the instruments is versatile in practice, such as top, side, and bottom illumination. Top illumination can utilize an objective with NA as large as 1, which allows tight focusing of laser light and also the focusing is in a symmetric fashion leading to a more predictable adjustment of alignment. In this geometry, the far-field background is also smaller compared to side-illumination. Since the objective is placed on top of the tip and the substrate, the gap-mode enhancement (see chapter 2.10.3) is feasible. However, as the tip is sitting between the objective and the substrate, this means a certain amount of incident and radiated light can be blocked by the tip. The substrates are not limited.

Bottom illumination is the type that the earliest versions of TERS in 2000 all employed. [83, 84, 86] It allows the highest NA≥1.4 to give a tighter focusing of a laser, higher collection efficiency and a smaller illuminated background area. Glass substrates are often used as a sample support due to the limitations of the transparent sample in this geometry. Indium tin oxide (ITO) or thin gold films can also be used serving as conductive substrate.

Side illumination was designed to overcome the limitation of needing a transparent sample in the bottom illumination geometry.[96] The laser beam is focused using long working distance objectives (with NA between 0.28-0.7) onto the tip end at angles usually between 45–70°. The laser focus is asymmetric and further enlarged to approximately 2-3 μm in this

geometry due to the angle between the focal plane and the sample surface. This might increase the demand for the laser power. The intrinsic benefit of this geometry is that the sample can be opaque or transparent. When a metallic surface is used, the gap-mode TERS can be constructed, and additional enhancement can be achieved to overcome the loss of low N.A.[87]

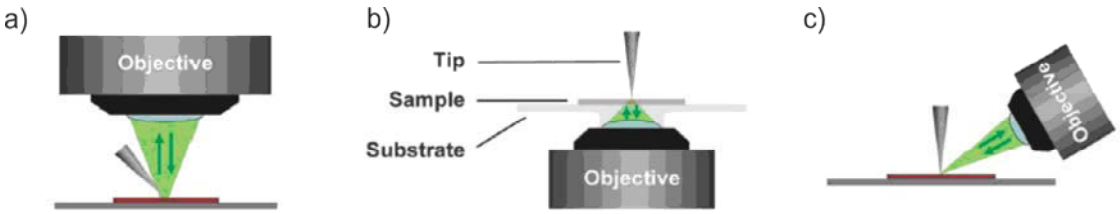

Figure 2.21 Illustration of the different possible illumination and detection geometries for tip-enhanced Raman spectroscopy, a) top illumination, b) bottom illumination and c) side illumination. Figures adapted from reference 87 with permission. Copyright © 2011, Royal Society of Chemistry

2.5.2 Tip lifetime

The common coated or etching materials for preparing TERS probes are gold and silver. Gold is rather stable in air and can be kept for a week once prepared. The downside is lower field enhancement compared to that of silver. However, silver tips are known to be prone to corrosion under atmospheric conditions due to their reaction with sulfur compounds. In addition, the mechanical instability is also of concern in TERS experiments; for example, the desorption of the hot spot from the coated tip due to the adhesion of Ag or Au to the silicon material is undesirable, or the deformation of the etched tip due to the applied voltage in a feedback loop is a problem. This results in lifetimes of silver tips being less than 12 hours once etched. [97] There has been much research dedicated to the protection of the tip. [97-99]

2.5.3 Gap-mode TERS

When a metallic surface is to be investigated, gap-mode TERS can be utilized between the tip and the surface since metal surfaces also have their own plasmon resonances. In these circumstances, due to the small distance between tip and surface, the excited plasmon at the tip apex can couple with the plasmon from the substrate surface, and change the resulting

plasmon resonances. This is similar to a system of very closely placed plasmonic nanostructures. The surface plasmons from two objects can interact with each other, inducing particular polarization states of the initial waveguide modes and converging to a new one. This creates a strongly localized and enhanced EM field in the gap between tip and surface, and is stronger than that of the tip or substrate alone. This is also how the much higher sensitivity and better spatial resolution can be reached in some research work. [7, 44]

Chapter 3

Experimental part: setups and materials

3.1 NT-MDT

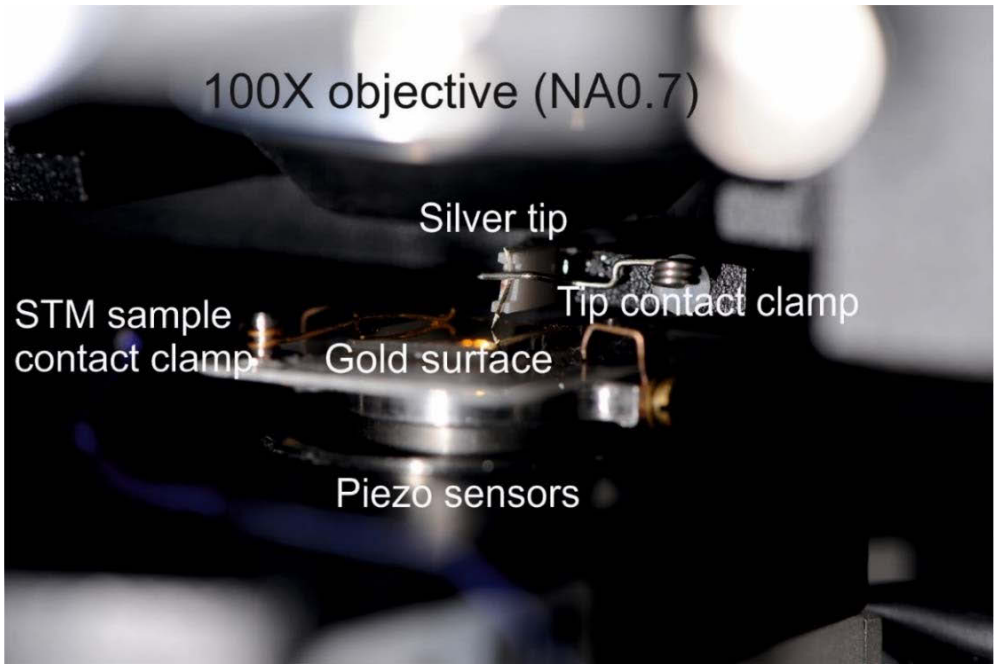

Figure 3.1 Photograph of the NT-MDT sample stage during an STM-TERS experiment. Photo credit: thanks to Lothar Opilik and Carolin Blum.

TERS instruments are generally comprised of two main parts: 1) a scanning probe microscope and 2) a Raman spectrometer. The NT-MDT Ntegra Spectra Upright in the Zürich laboratory has a an xyz sample scanner (100 µm x 100 µm x 10 µm) based on a piezo-ceramic tube in the platform and capacitance sensors for closed-loop operation in the first part of the instrument. The sample is placed on the scanner to perform SFM or STM. A measuring head with an incorporated objective (NA 0.7, W.D. 6 mm, 100x, Mitutoyo, Japan) and an attached SFM laser photodiode detector in the upper part of the head allows easy exchange of tip holders for SFM and STM tips via their respective adapters.

The second part of the instrument is a Raman spectrometer from Renishaw, which is equipped with an adjustable pinhole, a neutral density filter and a photomultiplier tube (PMT) for detection of the back-reflected/elastically scattered light in a confocal laser scanning microscope configuration. This detector is useful to quickly gather information about the reflectivity of the tip and later to locate a hot spot with the aid of a piezo scanning mirror in the beam path. Two visible lasers are coupled to the instrument by means of fiber optic cables.

One of them is a Helium-Neon laser with a wavelength of 632.8 nm and an output power of 10 mW (LGK 7627, Siemens, Germany). The other one is a diode-pumped solid-state laser (DPSS, MLL532, CNILaser, China) with a wavelength of 532 nm and an output power of 50 mW. Both laser beams are sent through a rejection filter and brought to the same optical axis by means of beam splitters. Motorized rotation of a circular variable neutral density filter (optical density 0-3.1) allows for continuous attenuation of the laser power on the sample stage.

Full-spectral imaging times can be shortened by taking advantage of the cropped sensor mode and the internal memory of the EMCCD camera. The silver tip was etched and mounted on the tip holder of the NT-MDT system, and stable tunneling feedback was established. The focused laser beam was scanned over the tip while Raman spectra were collected at every position to localize the hot spot.

3.2 AIST-NT OmegaScope

The TERS instrument in the Berlin laboratory was purchased from Horiba Scientific. It combines a SPM AIST-NT OmegaScope (AIST, USA) with a Raman spectrometer XploRA ONE™ (Horiba Jobin Yvon, Paris, France).

AIST-NT's OmegaScope (Fig. 3.2) includes Smart-SPM, which was designed to be integrated easily with optical instruments, such as a Raman spectrometer. The design of OmegaScope allows TERS measurements to be carried out in top-illumination or side-illumination mode. Since side illumination has higher enhancement, the work done here employed the side-illumination geometry. There is a top objective (10X, 0.28NA, Mitutoyo, Japan) to locate the tip onto an interesting area of the sample and illuminate with laser light from the side objective (100X, 0.70NA, Mitutoyo, Japan). There is a knob associated with the mirror in the laser beam path, to direct the laser either in the top or side objective. The alignment of the laser is checked firstly in the Xplora stage. Afterwards the laser beam is directed to OmegaScope in the top optical path to check the symmetry of the laser by focusing and defocusing. If the laser from the top is misaligned, the OmegaScope needs to couple well by adjusting the three feet of the Omegascope with screwdrivers. Since the side alignment is independent of the top, if the laser from the top is not significantly misaligned, one can adjust the focus of the laser in the side optical path by tuning the mirror. The mirror is situated inside the box next to the top-side switch. Lastly, the alignment in the side optical path can be checked by the symmetry of a laser exciting from the side objective and also the center of white light illumination should overlap with the center of the laser spot.

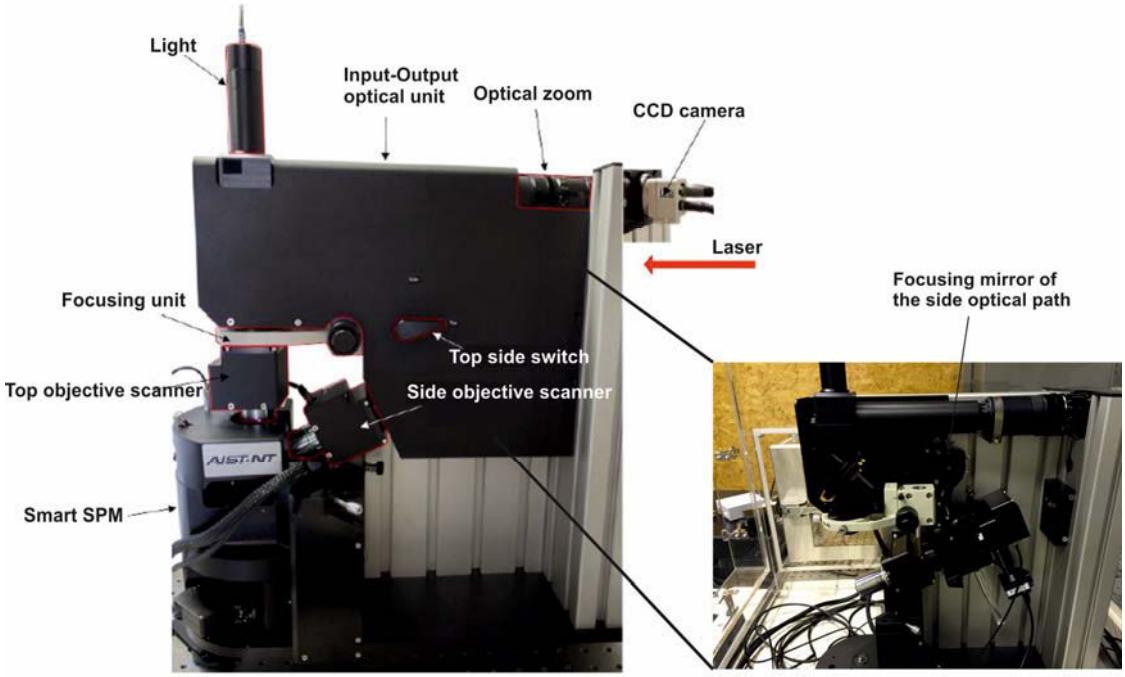

Figure 3.2 Photograph of the AIST-NT Omegascope designed to couple Raman and a smart SPM, which offers SFM and STM modes. Inset is the view of the inner mechanical parts.

It is necessary to bring the tip to the focus of an objective and also to the TERS alignment. This can be done with the aid of a rough disk in the sample stage regulated in SFM or STM feedback and reflecting the laser spot to the top camera view and side camera view, respectively. The position can be adjusted with the side screws (X, Y axis) and the bottom screw (Z axis) of the Smart SPM. The sample chosen to scatter light effectively is a magnetic plate due to its rough surface.

3.3 AIST-NT Smart-SPM

Smart-SPM is a modern multifunctional measuring system. The Smart-SPM provides an opportunity for measurements in ambient, liquid and controlled atmosphere environments. The software for Smart-SPM includes all the standard techniques of scanning force microscopy (SFM), scanning tunneling microscopy (STM), and a wide range of additional and special techniques, such as conductive SFM, turning fork, kelvin probe force microscopy (KPFM) and nanolithography, etc.. The instrument was implemented with a high level of automation, which includes automatic laser and photodiode positioning for aligning the SFM cantilever. The motorized approach of sample to tip is in 20 mm range (Z axis) and the motorized sample

positioning ranges 5x5mm. The piezo in sample stage offers a scanning range of 100 µm x 100 µm x 15 µm. Another key feature is that the head includes a 1300 nm photodiode laser for SFM mode, which allows the elimination of the cross-talk with the most popular Raman lasers up to 1064 nm. The IR registration laser also allows one to work with visible light-sensitive semiconductor and biological samples.

SFM

The instrument SmartSPM is more designed for SFM daily use than STM. Hence it offers multiple modes in the SFM system. It is sensitive enough to obtain molecular resolution in SFM mode easily. First, make sure the probe holder is in good focus with the diode laser, otherwise proceed calibration as below.

Use a STM holder to discharge the surface of a sample. Select the automation of finding a tip in the photodiode laser. The SUM of the reflectivity should reach 20,000. If not, the diode and the SFM laser can be recalibrated by first loosening the locking screw and adjusting the screw on the tip holder in the position between 0.3-0.5. Click “look around” in the software, and repeat this process until the image of the tip reflection in the software becomes clear. When the SUM reaches 20, 0000, the system is in good focus.

To obtain SFM molecular resolution operation: approach the surface and check the oscilloscope phase. In the window of curves view, conduct a z sweep between 15 and -2 nm. Ensure the Mag value in the Y axis of the curves view lies in the negative zone indicating a repulsive force between tip and sample. Increase the amplitude from 20 nm, to 30 nm, or 45 nm, and decrease the setpoint to reduce the distance between tip and sample.

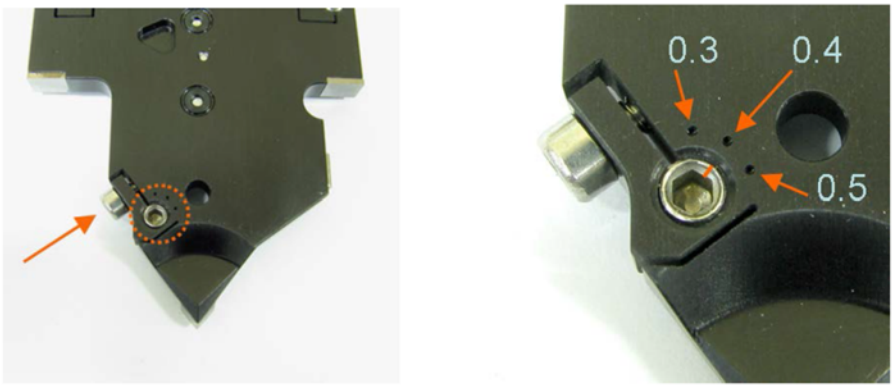

Figure 3.3 Left: SFM probe holder. The front set screw and the arrow points to the locking screw. Right: The marks on the probe holder. (Figure credit: Horiba Scientific).

STM

The atomic resolution of this Smart-SPM instrument is shown with PtIr tip on a standard sample of highly oriented pyrolytic graphite (HOPG).

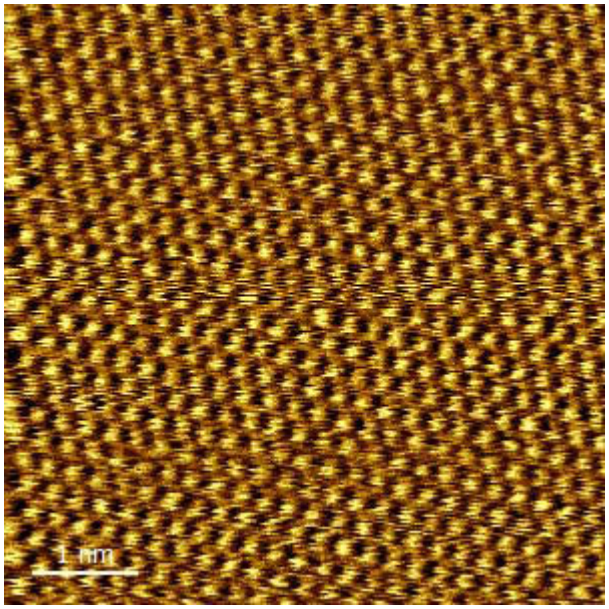

Figure 3.4 An STM image acquired with PtIr tip on HOPG, scan size in 5.5x5.5 nm^2.

3.4 Xplora

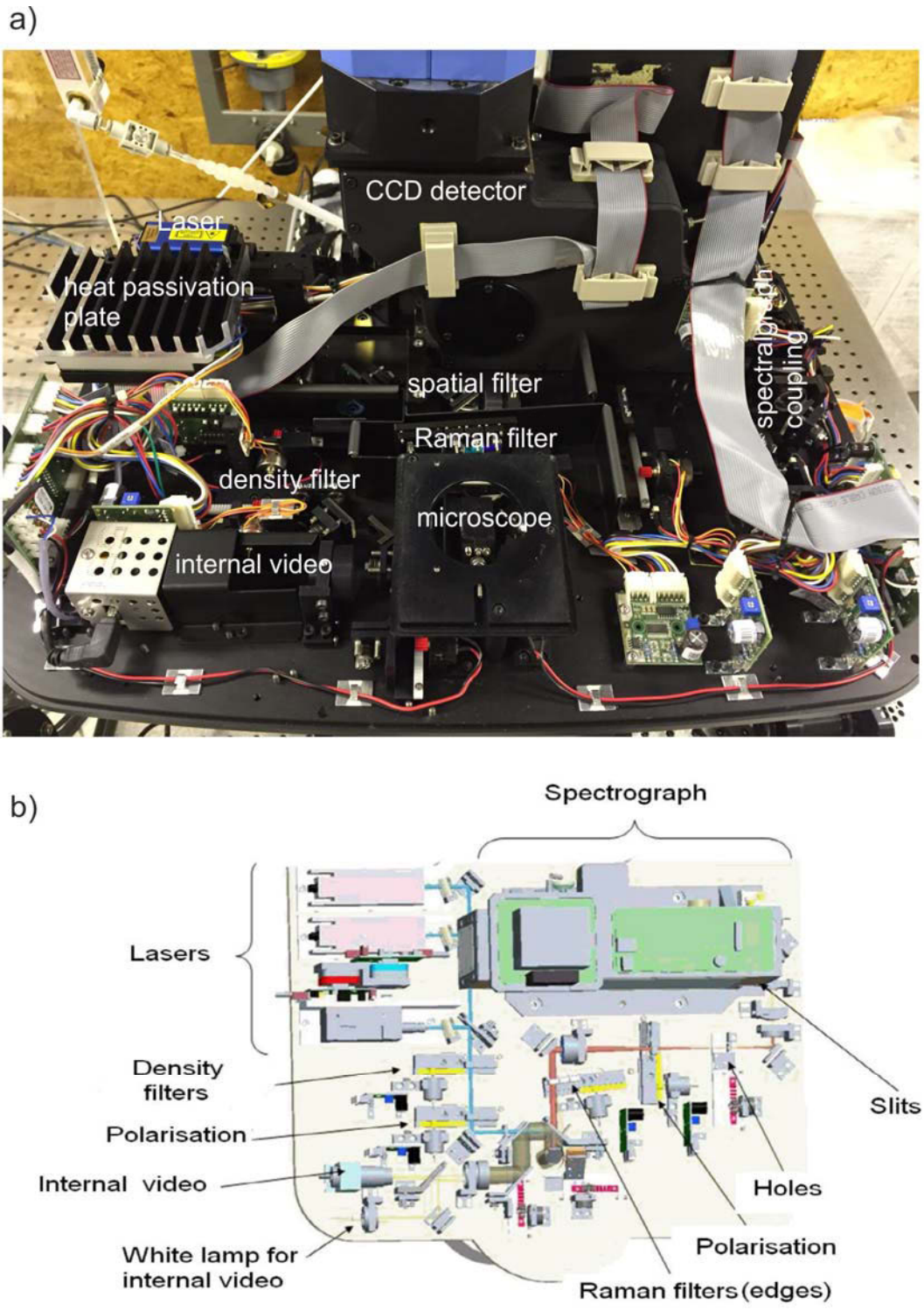

Figure 3.5 a) Photograph of the XploRA ONE™ internal components., b) optical components of Xplora (figure b) credit: Horiba Scientific)

The XploRA ONE™ (Horiba Jobin Yvon, Paris, France) is an integrated confocal Raman microscope system. The confocal microscope is coupled to a full Raman module equipped with laser sources, a motorized turret with 4-gratings, and a detector. There are three different excitation wavelengths supplied: 532 nm (output power 100 mW, Laser-Export Co. Ltd, Moscow, Russia), 633 nm (output power 35 mW, Innovative Photonic Solutions), and 785 nm (output power 100 mW, Innovative Photonic Solutions) for illumination. The four motorized gratings for full resolution are 600, 1200, 1800 and 2400 grooves/mm. Two objectives from Olympus Microscope with 10X (NA 0.25, WD 10.6 mm) and 100X (NA 0.9, WD 0.21) were mounted on the microscope to focus the laser beam onto the sample and collect the scattered light. The optical path is split into two parts, the illumination path and the collection (Raman signal) path. On the incoming laser path, the laser beam is reflected towards the microscope by the use of a special filter (dielectric edge rejection filter). It is used in injection/rejection mode which firstly directs the laser into the microscope and then filters out the Rayleigh scattered light as it returns to the spectrograph allowing only the Raman scattered light alone to be transmitted through to the confocal hole and the entrance of the spectrograph. The spectrograph itself is used to disperse the various multichromatic Raman spectral lines onto the CCD detector for detection. The Horiba Scientific CCD detector (1024x256 pixels) is kept cool at -70°C. The density filter provides 6 positions: 0.1%, 1%, 10%, 25%, 50% and 100% to attenuate the illuminated laser power. The motorized slit (50-150 µm) and pinhole (100-500 µm) can be controlled by LabSpec software. The polarization option is regulated by two motorized devices which select vertical (default without optic), horizontal, or circular polarization for the laser and vertical, horizontal, or unpolarized (without optic) for the scattered beam.

The alignment of the laser can be checked by the confocality, where the signal intensity of Si should yield more than 60% signals in the 100 µm pinhole compared to the 500 µm pinhole.

3.5 TERS probe

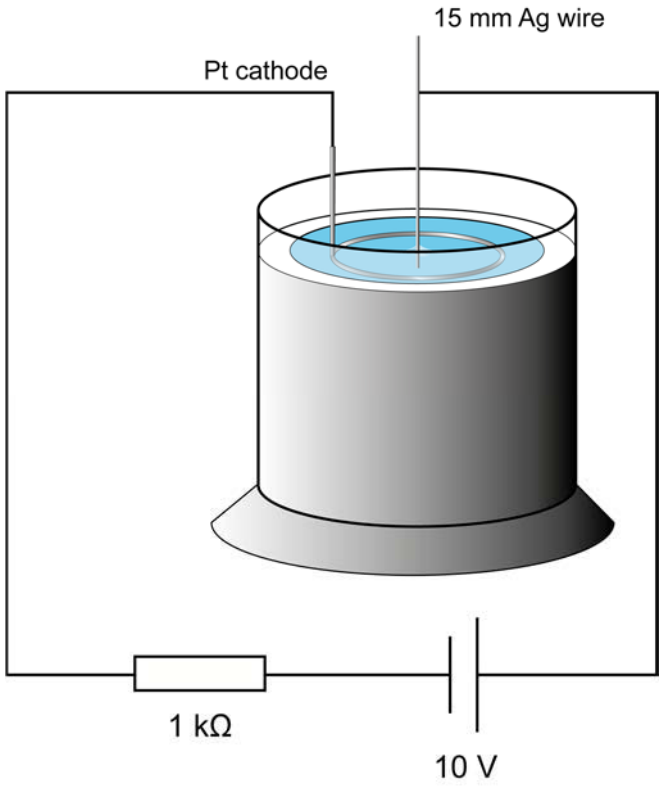

Figure 3.6 Scheme of a Ag etching set up. Figure based on reference 100.

Silver wires (diameter 0.25 mm, 99.99% purity, Alfa Aesar, Germany) were electrochemically etched in a 1:4 (v/v) mixture of perchloric acid (70%, Sigma Aldrich, Buchs, Switzerland) and ethanol (p.a., Sigma Aldrich, Buchs, Switzerland), similar to the procedure previously described by Blum et al.. A voltage of 10 V is applied and a 1 kΩ resistance provides the etching current of approx. 10 mA. Ethanol is added to prevent bubble formation. A platinum wire (Ø 0.5 mm) ring electrode with an inner diameter of approx. 13 mm is immersed in the etchant. It should be fully immersed in the etchant, however, close to its surface. The silver wire with a length of 15 mm is immersed in the etchant up to 2 mm. The etched tips were rinsed with ethanol and water, and checked for their sharpness with a Nikon 360xstereo microscope.

3.6 Substrate

Au(111) on mica (4x4 mm, #20020020, from Phasis, Geneva, Switzerland) was used.

Chapter 4

Tip-enhanced Raman spectroscopic imaging shows segregation within binary self-assembled thiol monolayers at ambient conditions

The material presented in this chapter has appeared as a peer-reviewed publication: W.-I. Lin, F. Shao, B. Stephanidis, and R. Zenobi, *Anal Bioanal Chem*, 2015, **407**, 8197-8204. Adapted with permission through Copyright Clearance Center. Copyright © 2015, Springer-Verlag Berlin Heidelberg. DOI:10.1007/s00216-015-8840-x

4.1 Introduction

Self-assembled monolayers (SAMs) on gold or silver surfaces are widely employed to generate tailored surfaces, for example, to influence surface wetting properties[101, 102], change rates of charge transport [103] and for chemical functionalization[104]. By utilizing a variety of thiols with different end groups and variable chain length, many properties on the surface can be custom-designed. Binary SAMs formed on a surface permit tuning of electronic properties such as the work function [105, 106]. If binary SAMs form domains, an alternating order of different thiol monolayers with distinct chemical properties on the surface is created, allowing interesting applications, for example, dual-affinity biosensors [107, 108]. Phase segregation of two-component thiol monolayers has been observed for functionalized and unfunctionalized thiols [109-111] and was found to occur only when certain mixing ratios were used [112]. For example, in the case of mixing 4-aminothiophenol (4-ATP) and *n*-octadecanthiol (ODT), a clear phase segregation occurred for a 60 % 4-ATP molar ratio, with 10 to 100 nm 4-ATP islands. If the molar fraction of 4-ATP increased above 60%, homogeneous mixing occurred. However, domain formation in mixed thiol SAMs is still relatively poorly understood. This, in part, is because there are many different thiols that are being used for such experiments, all exhibiting different adsorption behavior and intermolecular forces. Moreover, methods for their investigation on the nanometer length scale are scarce and typically lack chemical specificity.

Mixed thiol SAMs are known to be more disordered compared to pure alkanethiolate monolayers, where a crystalline structure is often observed.[113, 114] To investigate multifunctional surface structures, for example at molecular recognition sites of sensors or artificial receptors, it is necessary to visualize them on a nanometer length scale.[112] Some

research groups have attempted to use conventional scanning probe microscopy (scanning tunneling microscopy, STM or atomic force microscopy, AFM) to distinguish domains but failed to discern different chemisorbed molecules based on their height, [112, 115] although friction force SFM did reveal contrast. [112] Characterizing the molecular structure of SAMs is possible with high resolution STM imaging at ambient conditions, [116] however, even in a pure SAM, many packing patterns could be observed, [117] which means that the height measured by SPM can hardly identify the compounds in a mixed SAM. Additionally, the tunneling current in STM reflects not only the tip-sample distance but also the local electronic structure of the surface, which will require further complex data processing to reveal the domains.[118] The fact that there is hardly any literature available on characterizing mixed SAMs by SPM methods confirms the severe technical difficulties. Methods other than SPM including spectroscopic techniques[119, 120] contact angle measurements,[121] and mass spectrometry[122] have also been applied to characterize SAMs. Global spectroscopic methods provide precise structural/molecular information, however, they are limited in spatial resolution. Therefore, a method to analyze complex SAMs with chemical specificity and nanoscale spatial resolution is needed.

Tip-enhanced Raman spectroscopy (TERS) is a combined SPM and Raman technique, which allows one to simultaneously acquire spectroscopic fingerprint information and topographical features with ≈ 9-15 nm spatial resolution[88, 123, 124] at ambient conditions. Invented in 2000, [83, 86, 125] this near-field optical technique breaks the optical diffraction limit by employing a nanoantenna as a Raman signal amplifier. TERS allows one to obtain signals from a small number of sample molecules, rendering monolayers [115, 126, 127] and sometimes even single molecules on surfaces spectroscopically visible[26, 91, 92]. Early work using TERS to study SAMs was reported by Picardi[128]. An important finding was that the tunneling parameters in STM-TERS can strongly influence the enhanced Raman signal intensities. Chemical imaging by means of TERS was also used to identify the distribution of two patterned isomeric thiols on a gold surface, where STM cannot distinguish them, but spectral imaging does [115]. TERS has also recently been used to study binary SAMs on a gold substrate.[129, 130] Picardi *et al*. [129] showed that the subsequent exchange of molecules within a SAM by a second thiol occurred preferentially at grain boundaries of the gold substrate, and Horimoto et al. [130] showed a gradual change of the molecular composition of the original SAM with increasing immersion time in the second thiol solution.

There are two methods to prepare binary SAMs: (i) coadsorption and (ii) partial exchange of molecules in a pure SAM. In the present study, binary SAMs produced by coadsorption are studied by TERS for the first time. Whether the molecules chosen for this study form domains was previously unexplored. If binary SAMs indeed form domains, TERS should potentially be able to visualize this domain formation. Domains have been reported with sizes ranging from 10 nm to conjugated patches (i.e. stripelike domains) [131, 132]. With an appropriately chosen pixel size, it should be possible to see nanoscale domains with TERS. In addition, based on TERS mapping on a binary SAM and acquisition of spectra at different locations on the sample, statistical data evaluation is in principle possible to describe the nanoscale composition of the monolayers. Performing point measurements rather than mapping, for example, does not answer the question whether the molar ratio of thiols in solution is reflected in the molar ratio in the SAM.

Here, I demonstrate full spectroscopic mapping of binary SAMs, with a pixel size down to 2 nm. An oligomeric phenylene-ethynylene (OPE) was chosen for this study since conjugated phenylene-ethynylene oligomers are of interest for molecular electronics and have tunable functionality. I chose S-[4-[2-[4-(2-Phenylethynyl)phenyl]ethynyl]phenyl] thioacetate to represent an OPE system and produced mixed monolayers with thiophenol (PhS). The mixture of these two thiols is appropriate for TERS studies because they are both good Raman scatterers, have similar polarities, but distinctly different physical heights; if they form domains, the only prominent intermolecular forces, i.e., van der Waals forces, govern the molecular packing at ambient conditions.

4.2 Experimental methods

Setup. TERS measurements were carried out on a commercial combined STM/Raman microscope (NTEGRA spectra Upright, NT-MDT, Zelenograd, Russia) as described previously [88]. A HeNe laser (632.8 nm) was utilized for illumination, with a typical laser power of 95 µW on the sample stage. The acquisition time was chosen between 1 s and 3 s. STM images were recorded with the same tip before or after TERS mapping. STM measurements were performed in constant current mode with a setpoint of 0.1 nA and a bias voltage of 0.1 V. High resolution STM images with a smaller scan range (less than 500 x 500 nm^2) were recorded with a table-top STM (Easyscan, Nanosurf, Liestal, Switzerland).

TERS tips. Silver wires (diameter 0.25 mm, 99.99% purity, Alfa Aesar, Germany) were electrochemically etched at a voltage of 10 V in a 1:4 (v/v) mixture of perchloric acid (70%,

Sigma Aldrich, Buchs, Switzerland) and ethanol (p.a., Sigma Aldrich, Buchs, Switzerland), see chapter 3.5. The etched tips were rinsed with ethanol and water, and checked for their sharpness with a Nikon 360xstereo microscope. The tip was afterwards mounted on the tip holder of the NT-MDT system, and stable tunneling feedback was established. The focused laser beam was scanned over the tip while Raman spectra were collected at every position. Details of this procedure ("hot spot localization“) were given previously in chapter 3.1.

Samples. Thioacetic acid S-[4-[4-(phenylethynyl)phenyl]ethynyl]benzene-thiol ester (as an OPE) (Sigma Aldrich) and thiophenol (Acros, USA) were purchased. Deprotection of OPE was accomplished by hydrolysis of thioacetate in ethanol (0.5 mM) by adding NaOH to the solution (10 µL, 1N) as a hydrolyzing agent. Thiophenol (PhS) was prepared as 10 mM solution in ethanol. Au (111) on mica (4x4 mm, #20020020, from Phasis, Geneva, Switzerland) was immersed in the ethanolic thiol solution for 24 h at room temperature. I used three different mixing ratios of PhS and OPE (corresponding to the molar ratio of the molecules in solution), i.e. PhS:OPE = 10:1, 2:1 and 1:1, with the intention of obtaining binary SAMs with different domain sizes[133]. The concentration of PhS was chosen to be higher than that of OPE because the latter is the stronger Raman scatterer.[126]

Data processing. Spectra were processed in Matlab (version R2014b, MathWorks, Natick, Massachusetts, USA). The procedure included background subtraction followed by smoothing (moving average and a robust version of locally weighted scatter plot smoothing, LOWESS). In order to investigate the spatial distribution of the two thiol molecules, the intensity ratio of the peaks at 1129 cm^{-1} (”Peak 1“) and 1077 cm^{-1} (”Peak 2“) was calculated at every position of the map. Only pixels with a signal-to-noise ratio higher than 3 for either of the evaluated peaks were taken into account. Pixels containing only noise in the map are marked as such. I could also have chosen the peak of the triple bond band as an OPE marker, which appears only in the OPE spectrum, but peaks 1 and 2 are much closer to each other in the spectrum, less affected by variations in background and any possible wavelength dependence of the enhancement, which should be a more reliable measure of the local composition. Besides the ratio map of Peak1/Peak2, the absolute intensity of the peak at 2214 cm^{-1}, the signal due to the triple bond, is also shown for comparison.

STM images were processed with gwyddion (a modular program for SPM data analysis [134]), and 2D-plane subtraction (slope correction) and line mean corrections were carried out.

4.3 Results and discussion

An atomically flat gold surface was used for this study. An STM image of a bare gold substrate is shown in Figure 4.1. The measured step height is 0.2 nm between adjacent gold terraces, close to the expected height of an atomic step on Au [135]. An OPE SAM on gold was then investigated with STM and TERS; the STM topography shows that imaging the structure of single thiol SAMs at ambient conditions reveals little information (Fig. 4.2).

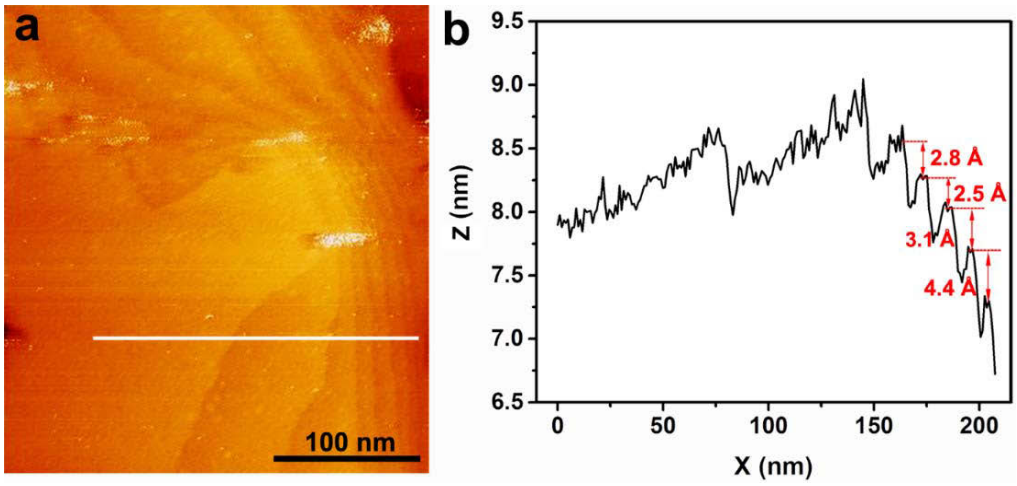

Figure 4.1 A STM image of a bare gold surface showing atomically flat terraces. Clear step-edges corresponding to the height of a single gold atom were observed in the cross-sectional profile. The observed flat, 300-400 nm wide terraces are in accordance with reported surface features of Au.

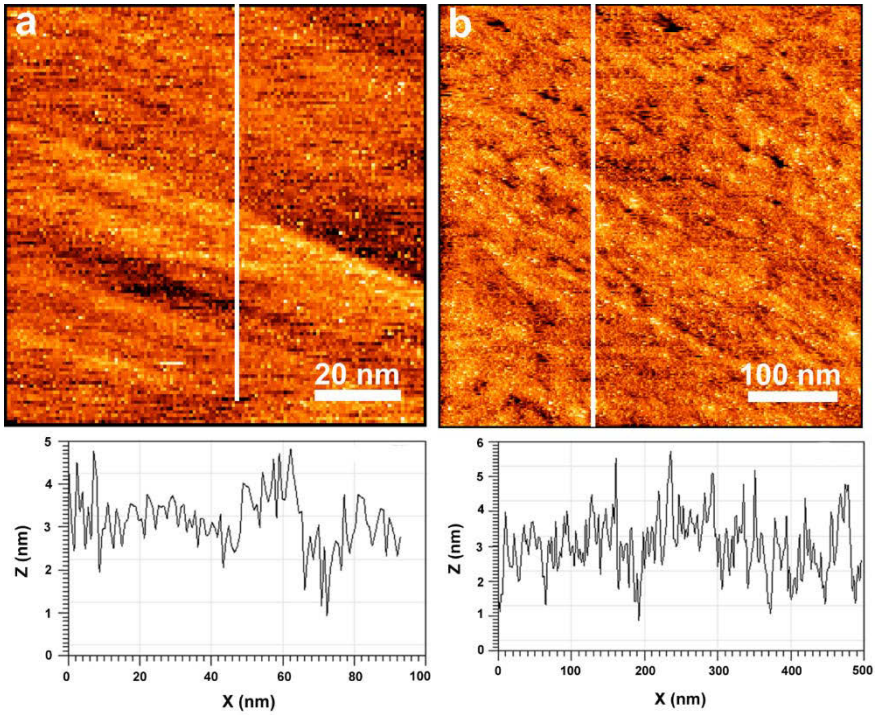

Figure 4.2 STM image of pure OPE SAM sample on Au surface and the cross-sectional profile of the white line in the topography a) an area of 100x100nm^2, 128x128 points b) 502x502 nm^2, 256x256 points. One can see there is a variation of height difference between islands, which span over 20 nm.

A high-resolution STM scan of a mixed SAM sample prepared with a 10:1/PhS:OPE molar ratio in solution is shown in Fig. 4.3 A. The corresponding height profile (Fig. 4.3 B) exhibits a low noise level (rms: 0.0064 nm). The maximum expected height difference of the two thiols is 1.6 nm, but no areas with a height difference of that order are visible in the profile. One reason for this may be that PhS and OPE exhibit different adsorption angles on Au(111) such that even if domains form, no height difference is evident. In other words, it can be tricky to characterize mixed adsorbates by STM alone. Consequently, TERS maps were acquired to study the phase segregation of binary SAMs on an Au surface.

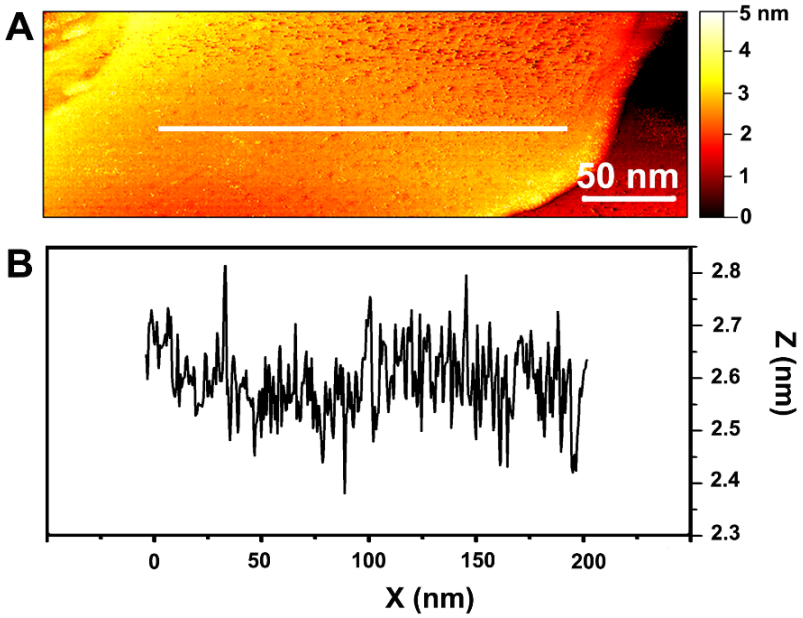

Figure 4.3 A) STM image (area 340x110 nm^2) of a PhS/OPE binary SAM on Au(111). B) As can be seen in the cross-sectional profile, the measurement fails to discern molecular domains via their expected maximum height difference of 1.6 nm.

The thiols chosen, OPE and PhS, have quite different Raman spectra. TERS spectra of pure OPE and PhS are shown in Fig 4.4. The peaks at 1002, 1023, 1077, and 1580 cm^{-1} are signals due to aromatic ring vibrations. Whilst the peaks at 1002, 1077 and 1580 cm^{-1} are visible both in OPE and PhS, the peak at 1129 cm^{-1}, assigned to a ν(C-H) in-plane mode [136], is only observed and particularly strong in the OPE spectrum. This mode is pronounced only in molecules with three phenyl rings [126, 137] , hence it can be used as a marker band for OPE when studying the distribution of OPE and PhS on the surface. While the peak at 1023 cm^{-1} is exclusively observed in PhS spectra, its intensity was too close to the noise level in many of the spectra. This ruled out its use as a marker band for PhS. In order to investigate the spatial distribution of these two thiol molecules, the intensity ratio of the peaks at 1129 cm^{-1} and 1077 cm^{-1} was therefore calculated at every position of the TERS maps.

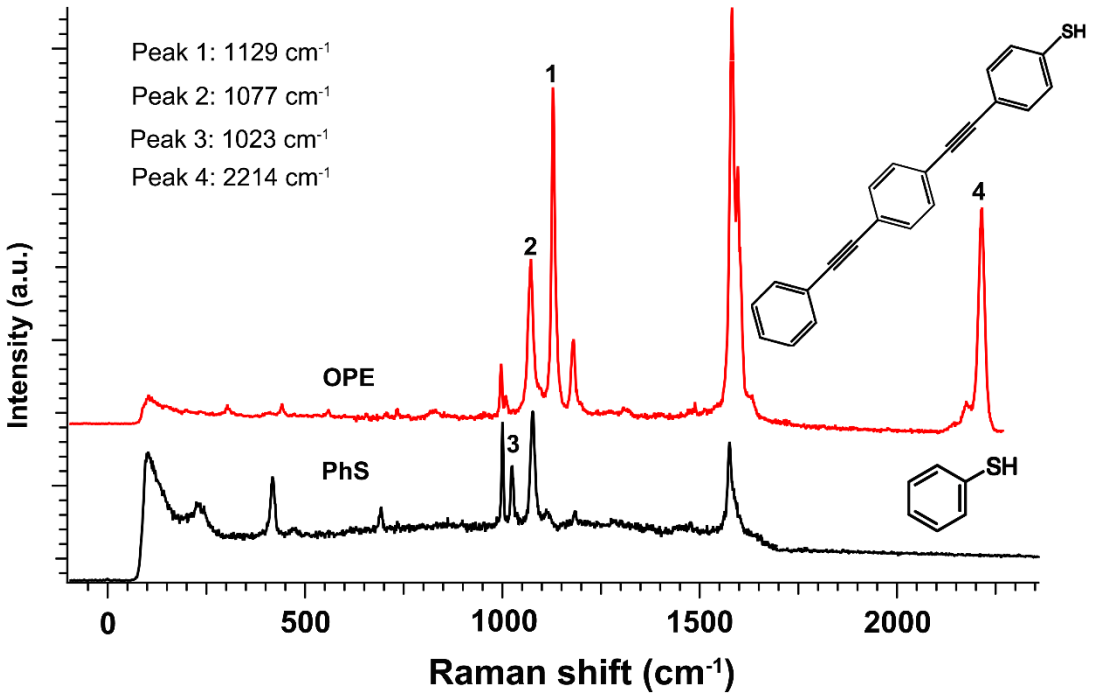

Figure 4.4 TERS spectra of pure thiols forming SAMs on a gold surface. The black spectrum is from a SAM of thiophenol (PhS) and the red spectrum from a SAM of OPE on gold.

A TERS map of a pure OPE sample with 4092 points was measured and the peak ratio was plotted (Fig. 4.5 A). The histogram in Fig. 4.5 B shows that the ratio of the two marker bands (1129/1077 cm^{-1}) exhibits a Gaussian distribution, with a mean value of 2.51 and a standard deviation of 0.47. The variation of this ratio may result from the angle of the molecules relative to the surface, which directly affects the orientation of the Raman scattering tensor. OPE is the larger molecule and can thus sample a larger range of distances to the surface if it assumes different orientations. [126] Additionally, since the peaks at 1129 and 1077 cm^{-1} are both CH in-plane bending modes, [136] they will only be excited at the same time, which eliminates another possible systematic error if the intensity ratio of these two peaks is used[138]. From this data it can be concluded that a pure OPE TERS spectrum exhibits a peak ratio between 2.04 and 2.98 with 68% probability and between a ratio of 1.57 to 3.44 with 95% probability. The peak at 1129 cm^{-1} is only observable in the OPE spectrum, hence if a spectrum of a binary SAM has a peak ratio significantly above 2, such a pixel contains mostly OPE molecules. In contrast, if the 1077 cm^{-1} peak becomes stronger, which means that there is a large contribution from PhS molecules, the peak ratio will drop to less than 2. Taking somewhat arbitrary thresholds for the peak ratios, I consider pixels with a ratio between 1 and 2 to contain a considerable amount of PhS, and predominantly PhS molecules if the ratio is

between 0.5 and 1, while pixels with a peak ratio of less than 0.5 imply essentially a pure PhS island. Employing the peak ratios to compare the amount of components in a mixture has been reported before [127, 130, 139, 140]. Accordingly, all TERS maps below are shown with the false color scale as depicted in Fig. 4.5 A, with red representing pure OPE. Nevertheless, I have to caution that it is difficult to determine accurate surface coverages of the two thiols from peak ratios by TERS.

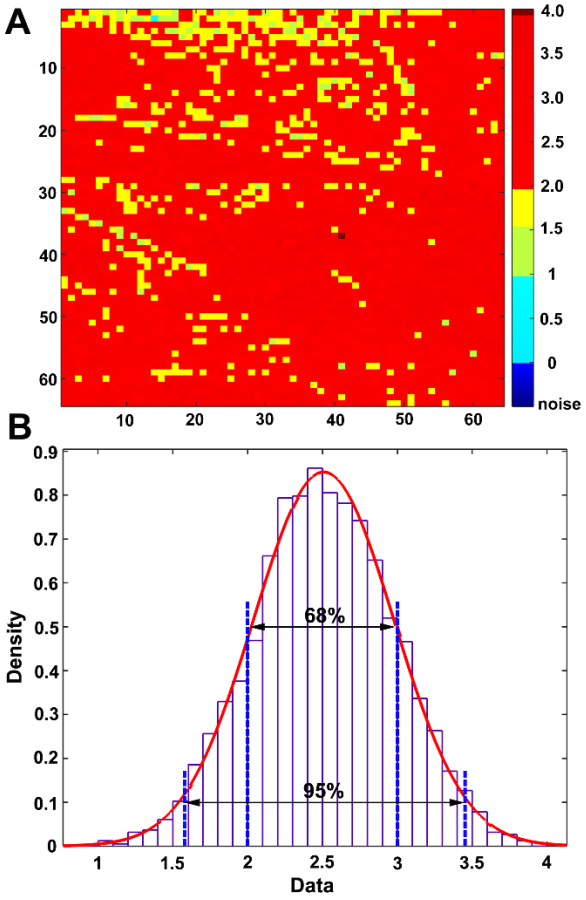

Figure 4.5 A) A TERS peak ratio map of a pure OPE SAM (showing the intensity ratio of peak 1129 cm^{-1}/ peak 1077 cm^{-1}) measured over a 304 nm x 304 nm area with 64 x 64 points; the color coding of the peak ratio map in all figures is the same. B) A histogram of peak ratios in 4096 points fitted with normal distribution, showing that 68% of the data is in the range of 2-3 ratio value.

Fig. 4.6 A shows a TERS map (512x512 nm^2 and 32x32 pixels) of a binary SAM prepared with a 1:1 ratio. Large domains of OPE and PhS can be easily seen from the map, i.e., phase segregation clearly takes place. PhS is, for example, dominant in the blue area in the bottom right of the map. The size of the largest PhS domain is bigger than 64x240 nm^2, and additionally smaller islands with a length of 48 nm (3 pixels) are visible. OPE also shows two pronounced

domains colored in red on the map with few isolated pixels dispersed in the yellow area, where PhS is interfacially present but OPE is dominant. This shows that the determination of domains is not an artifact from the feedback (the STM was operated with a fast X scan and a slow Y scan). Also, variations in the distance between the tip and the surface can have a significant influence on the signal intensity, [129] but should have no effect on peak ratios.

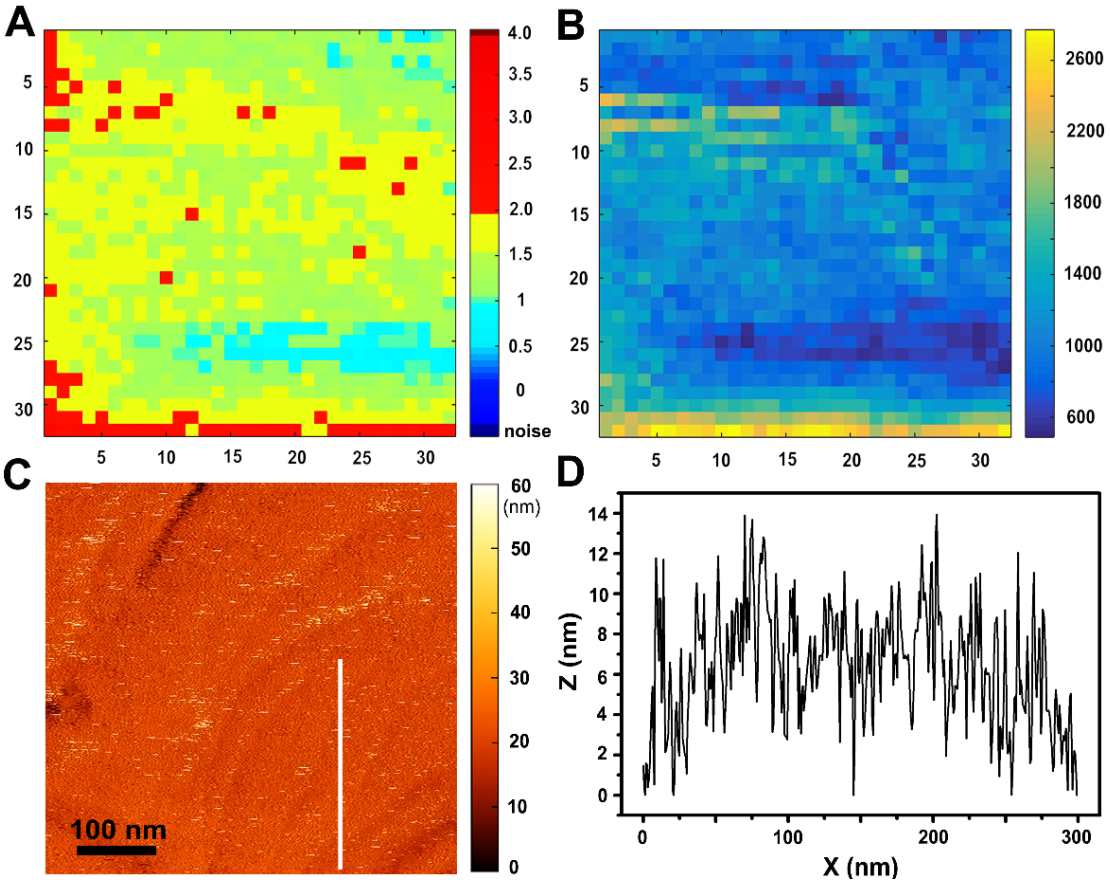

Figure 4.6 A) TERS peak ratio map of a binary SAM (with a 1:1 ratio). An area of 512x512 nm^2, 32x32 pixels (16 nm/pixel) was measured. B) An intensity map of the 2214 cm^{-1} peak (triple bond). C) STM image acquired in the same area after the TERS measurement. Several domains are included but not visible as the height differences in the STM data. D) Cross-sectional line profile showing the variation in height across a PhS island. Note: the 100 nm scale bar applies to all maps in Fig. 4.6 A, B and C.

A corresponding map of the absolute intensity of the triple bond is also shown in Fig. 4.6 B. The area where OPE is abundant (bright yellow in Fig. 4.6 B) shows a high triple bond intensity, whereas in the area where PhS domains are located (peak ratio less than 1), the triple bond signal intensity is low (dark blue), which coincides very well with the ratio map of the two marker bands. The absolute intensity distribution map of the peak 2214 cm^{-1} shows features that are consistent with the peak ratio map. I hypothesize that this is because the modes corresponding to the peaks at 1129 and 2214 cm^{-1} are of the same symmetry[138]. This supports the method of using peak ratios of the same symmetry to compare the relative amount of the two thiol molecules.

An STM image is shown in Fig. 4.6 C with 512 x 512 points (512 x 512 nm^2) recorded right after the TERS imaging experiment. The STM image does not show any clear height differences. Atomic steps of the underlying gold substrate seem to be observable, but domains in the binary SAM were not discernable based on height differences. A cross-sectional line profile is shown in Fig. 4.6 D (spikes were removed), which in this case shows an rms height variation of 2.85 nm. This again illustrates the difficulty and inconvienence in defining domains by STM height alone.

Fig. 4.7 A shows a 3x3 μm^2 STM topographic image of a binary PhS/OPE SAM on Au(111) prepared with a 10:1 molar ratio in solution. Several large gold grains (500-1000nm) with rather smooth surfaces can be seen. The TERS map in Fig. 4.7 B was measured over the whole area using 32x32 points with a 96 nm pixel size. Phase segregation can again be observed in the map. Two domains with a peak ratio >2 can be discerned, with a size around 0.5x1 μm^2 and 1x1 μm^2. Compared to the STM image, these two OPE-rich domains seem to cover the surface of the gold grain underneath. In the upper part of the image there is a large area with a peak ratio below below 0.5 (dark blue, the peak at 1129 cm^{-1} has very low intensity), indicating a domain of pure PhS with a dimension of ≈ 2.5x0.5 μm^2. When zooming into an area of this map (red rectangle), an STM image was first recorded (Fig. 4.7 C), followed by a TERS map (Fig. 4.7 D). However, the segregation distribution does not reproduce the image in Fig. 4.7 A. The domain size of OPE now appears to be ≈ 290x580 nm^2.

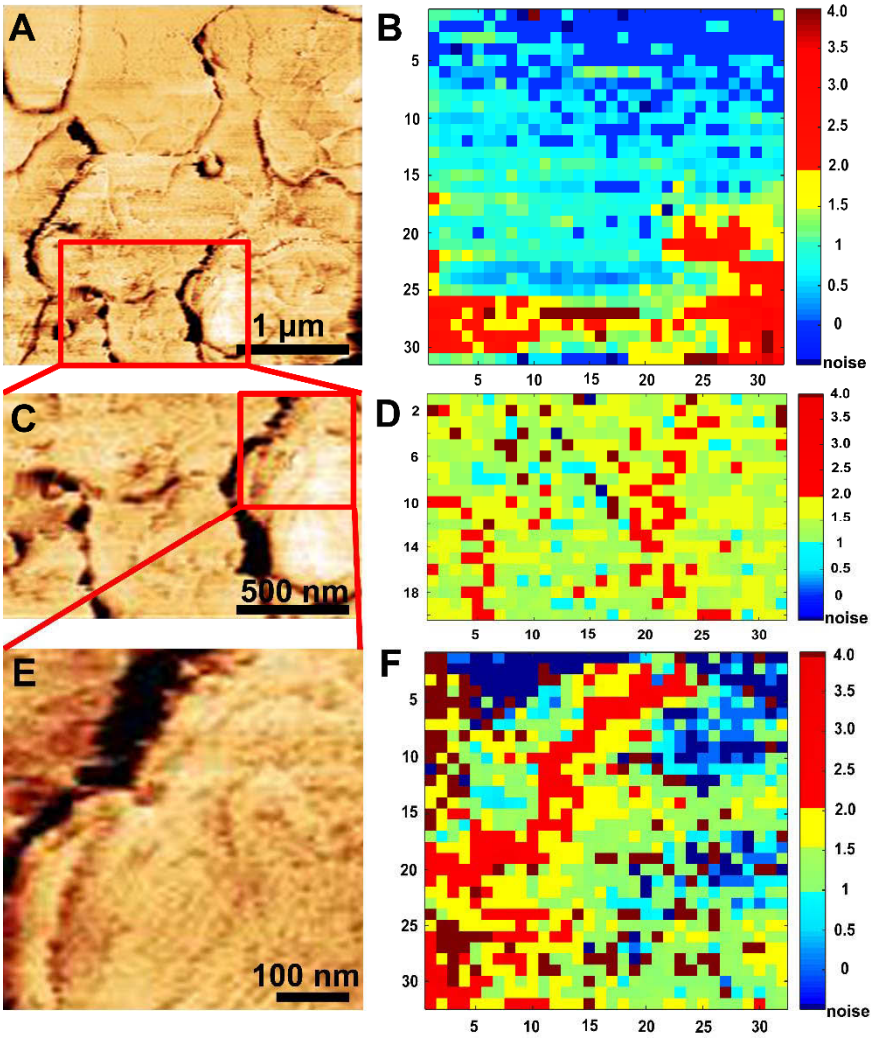

Figure 4.7 A) STM topography image (3x3 µm^2). B) A TERS peak ratio map of a binary SAM (with a 10:1 ratio), 32x32 pixels on the same area as a (96 nm/pixel). C) Zooming into the red rectangle, an STM image was first acquired with 1.5 µm x 1.0 µm before TERS. D) The TERS peak ratio map corresponds to the area in C, 48nm/pixel. E) an STM image by zooming into the red square in C. F) The TERS peak ratio map corresponds to the area in E, 16 nm/pixel. Pixels in brown and dark blue have signals at the noise level.

Domains of PhS and OPE are easy to distinguish in these three TERS maps, which reveal two-component SAMs to be segregated instead of intermixed. An STM image acquired during the TERS map (Fig. 4.7 D) is also available (Fig. 4.8 A) to prove that sample drift is insignificant. At first glance it seems strange that the size of the molecular domains is reduced in TERS maps recorded with smaller pixel size. This phenomenon can be rationalized by the TERS enhancement radius, which is usually estimated to be 6-15 nm (if the tip radius is 20-50 nm, and the tip-sample distance is 1-2 nm [130]), being significantly smaller than the pixel size in

Figure 4.7 B. When the pixel size used is larger than 15 nm, the area between two pixels is not being scanned completely by the TERS tip. In other words, the signal only comes from a ≤15 nm radius below the TERS tip. Therefore, a pixel size larger than 15nm can introduce errors in defining domain sizes. This is reflected in our TERS maps, where the features recorded with a coarser pixel size (Fig. 4.7 B) are not reproduced in Fig 4.7 D. Additionally, along the gaps between gold grains, TERS shows a higher relative peak ratio for OPE. I interpret this to be due to preferential adsorption of one of the two species, OPE in this case, and also its preferred molecular orientation in these gaps. These edges of gold grains thus show unique features. This is further confirmed by zooming into the same area with a 512 nm map, (32x32 points, Fig. 4.7 F), where the Raman spectra of the gap show evidently higher absolute intensity in the TERS map. (Fig. 4.8 C)

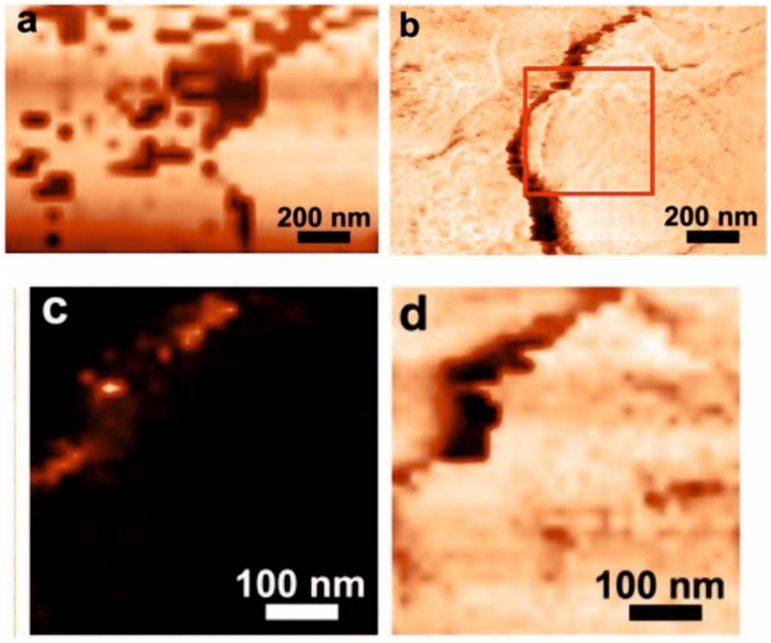

Figure 4.8 A) A lower resolution STM height image acquired during the TERS scan (Fig. 4.7 D). B) STM image recorded before zooming into the red square area, C) the TERS absolute intensity is plotted, where the brighter zone has higher intensity. D) STM image acquired simultaneously with the TERS measurement.

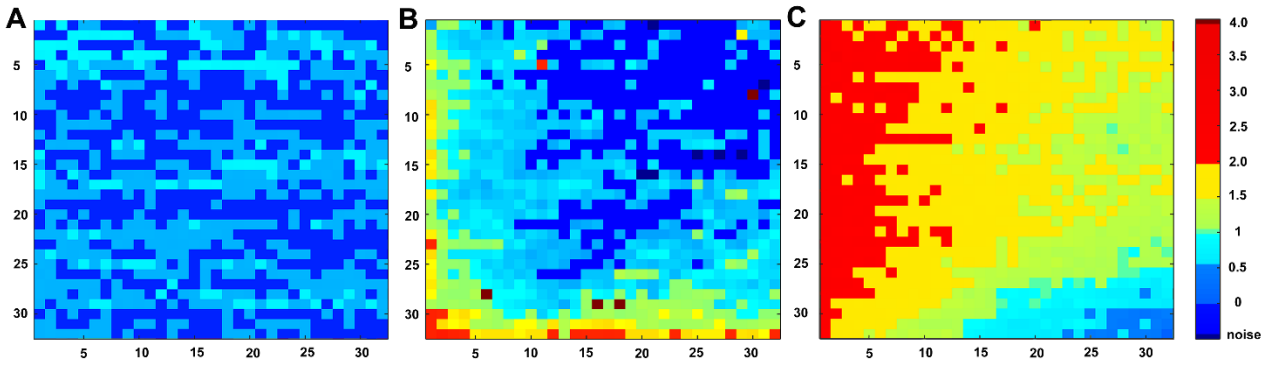

Figure 4.9 TERS peak ratio maps of binary SAMs measured with 8 nm/pixel, samples were prepared in a ratio of A) 10:1, B) 2:1, C) 1:1, respectively.

The segregation effect of mixing OPE and PhS were also explored and compared with samples prepared with different molar ratios, 10:1, 2:1 and 1:1, respectively, in solution. TERS peak ratio maps were measured with 8 nm/pixel. Fig. 4.9 A shows islands containing predominantly PhS with a size around 50x50 nm^2 (dark blue). The light blue pixels imply that in these areas some OPE is also present. A larger area map (512x512 nm^2) of the same sample is shown in Fig. 4.10 A, which confirms this. Fig. 4.9 B was acquired in an area of 250x250 nm^2, the essentially pure island continuously spans over a size of 80x160 nm^2, while there is some OPE distributed around the PhS domain. The segregation is very strong, and agrees well with a TERS map (measured with 2 nm/pixel) that was acquired with the same ratio (Fig. 4.10 B), where the TERS tip landed inside a PhS domain, which was wider than 128 nm. The binary SAM prepared with a ratio of 1:1 measured with 8 nm/pixel also exhibits an essentially pure PhS island larger than 40x320 nm^2 on the bottom of the map, while an OPE domain is located on the left side of the map (depicted in red, Fig. 4.9 C).

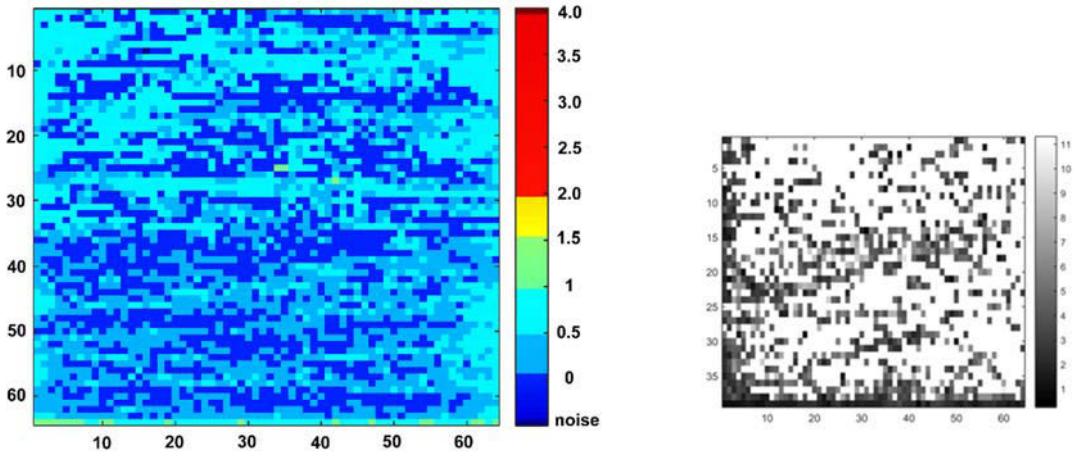

Figure 4.10 a) 512x512 nm^2 TERS map showing the peak ratios of a binary PhS/OPE prepared with a 10:1 ratio using 8 nm/pixel; and b) High-resolution TERS peak ratio map of a binary PhS/OPE prepared with a 2:1 ratio using 2 nm/pixel in a 124 nm x 78 nm area. The peak ratio was calculated reversely, with $1077cm^{-1}/1129cm^{-1}$. The peak ratios in this map are all above 1, indicating that the TERS tip landed inside a PhS domain, and that the PhS domain size is more than 128 nm wide.

Because TERS mapping yields many data points, it is conceivable to use it to answer whether the molar mixing ratio of thiols in solution reflects the fraction of adsorbed thiols on the surface. Fig. 4.11 shows the histograms of the TERS peak ratio for samples prepared with different thiol molar ratios. The total number of data points in each map was 4096, 1024 and 4096, respectively. Histograms (Fig. 4.11) show that samples prepared with a ratio of 10:1 and 2:1 exhibit a large fraction of pure PhS pixels (the peak 1129 cm^{-1} has very low intensity, so the ratio is close to 0), while samples prepared with a ratio of 1:1 yields significantly more points with a peak ratio larger than 1.5, which implies that OPE was predominantly adsorbed on the sample surface. These three maps show a consistent trend between the amount of the adsorbed molecules and the molar fraction in a solution, although a complete quantitative agreement was not reached.

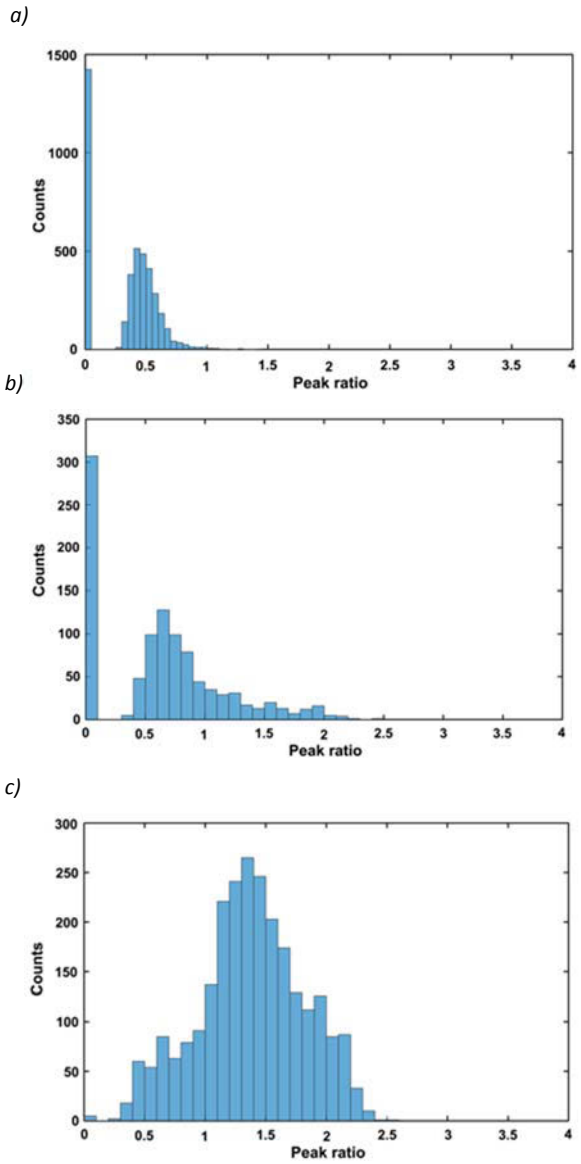

Figure 4.11 Histograms of TERS peak ratio values with samples prepared with a ratio of a) 10:1, b) 2:1, and c) 1:1, respectively. The trend of OPE amount is significantly increasing with the corresponding molar fraction in a solution while PhS is predominant in the sample with a ratio of 10:1 and 2:1. This implies a strong relationship of adsorbed molecules onto the surface with the molar fraction in a solution.

4.4 Conclusion and outlook

TERS, a nano-spectroscopic method, provides a powerful tool for spatially resolved (≈10 nm) chemical analysis of surface adsorbates, in cases where STM is ”blind“. I showed that full spectroscopic mapping of mixed thiol SAMs is possible via TERS, and that ratios of marker peaks can be used to discern segregation within the monolayer. If the molecular domains are larger than 15nm, TERS can give a reliable domain size by using a pixel size in the range of a few nm. Histograms generated from many data points were also compared, giving complementary insight about the composition of the SAMs. This is the first time that maps with full chemical information have demonstrated phase segregation in coadsorbed thiols.

Chapter 5

Strongly enhanced Raman Scattering of Cu-Phthalocyanine between graphene and flat Au (111)

The material presented in this chapter has appeared as a peer-reviewed publication: W.-I. Lin, M.F. Gholami, P. Beyer, N. Severin, F. Shao, R. Zenobi, and J.P. Rabe, *Chem Commun*, 2017, **53**, 724-727. Adapted with permission from The Royal Society of Chemistry. DOI: 10.1039/C6CC08672A

5.1 Introduction

Surface-enhanced Raman scattering (SERS) is a sensitive spectroscopic method for microanalysis and trace species detection. It is attributed to two contributing factors: the electromagnetic field mechanism (EM) and the chemical mechanism (CM).[3, 4] While the EM has been thoroughly investigated through theoretical and experimental studies, the CM is still a matter of debate in the literature.[141, 142] Direct experimental studies of the CM are challenging because of its typically small contribution compared to the enhancement by the EM effect. The recently demonstrated graphene-enhanced Raman scattering (GERS) [75, 76, 143] has been viewed as a valuable model to uncover details of the CM since flat graphene, due to its optical properties, has been argued to provide mainly chemical enhancement of the Raman scattering of molecules near its surface.[17] Flat gold is also known to provide CM-dominated SERS enhancement. An interesting open question in this context is whether the combined chemical enhancements provided by the two different materials could add to each other for a molecule sandwiched between them.

Many aspects of GERS have been investigated such as the charge transfer mechanism,[17] the dependency on the number of graphene layers, [144] and the orientation of the molecules.[14] Also the effect of adsorbed and intercalated molecular species on graphene, particularly on the first molecular layer,[77,145] and the molecular selectivity.[79] However, to the best of my knowledge there is no study of the GERS effect on a substrate that itself has been argued to provide CM-dominated Raman enhancement. Different but somewhat related is the work on metal nanoparticles covered by graphene, effectively preventing the adsorption of molecules onto the metal surfaces. In this case the enhancement effect was dominated by the EM due to the metallic nanoparticles underneath graphene.[146]

Here I address the question whether the chemical enhancement from GERS can be improved further by a flat SERS substrate providing also only chemical enhancement. Particularly, I report on sandwiched Cu-phthalocyanine (CuPc) molecules between Au(111) and graphene. CuPc has a large Raman cross-section, which allows the detection of its Raman spectrum in ultrathin films, even in the absence of any surface enhancement. In addition, CuPc is a planar and π-conjugated molecule, stable at ambient conditions and not fluorescent.[147] Its deposition onto an Au(111) surface results in mainly flat lying molecules,[148, 149] and also graphene induces CuPc to lie flat on it[13]. The good electronic coupling of a flat lying CuPc molecule to the "aromatic" two-dimensional graphene allows one to dwell also on the high molecular selectivity of the GERS effect[79]. In fact, CuPc can provide novel and intrinsic molecular junctions at the nanoscale[150]. On the other hand, graphene is chemically inert, optically highly transparent, and impermeable to small molecules, thereby acting as a perfect barrier to, e.g., oxygen and water.[11] The use of graphene as a quencher for electronic and vibrational excitations has also been reported[74]. Similarly, flat gold is known to be a fluorescence quencher and it shows SERS efficiency[18]. Therefore, the sandwich structure – CuPc between graphene and atomically flat gold – provides a well-defined platform for the investigation of optoelectronics on the nanoscale, including photo-induced electron transfer. In particular, it allows one to address the question, whether the mainly CM-dominated GERS-effect can be enhanced further through a flat SERS substrate.

I carried out Raman investigations of a system of graphene mechanically exfoliated onto an Au(111) surface, which had been pre-coated with vacuum evaporated CuPc molecules (Fig. 5.1). This has the advantage that the CuPc molecules are in contact with both graphene and gold, allowing for electron transfer in both directions.

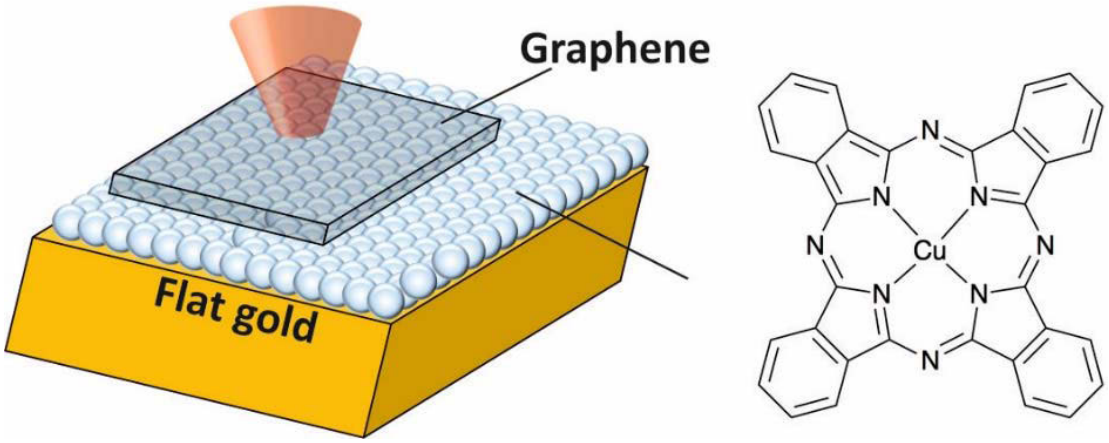

Figure 5.1 Scheme of a sandwiched graphene-CuPc-gold sample structure

5.2 Experimental methods

Materials

As a substrate, Au(111) with 200 nm thickness on mica (4x4 mm, #20020020) was purchased from Phasis, Geneva, Switzerland. The substrate is partially covered with gold (as Fig. 5.2). The sample of Graphene-CuPc-gold was prepared on the substrate surface coated with gold, while the Graphene-CuPc-mica sample was prepared on the same substrates on mica. This allows the molecular film to be prepared from the same batch in vacuum evaporation. Graphene is produced from HOPG (obtained from Momentive Performance Materials Quartz, Inc. OH 44149, United States) by mechanical exfoliation with a contamination-free method[57]. CuPc was purchased from Sigma Aldrich with 99.95% purity. CuPc molecules were vacuum evaporated onto Au (111) and mica. In order to remove contaminations and promote the formation of large gold crystals on the surface, the substrates were flame annealed before introducing them into a vacuum chamber. Following this, a second annealing step (770 K, 1 h) was performed in vacuum before starting the film growth. Afterwards the molecules were thermally evaporated from a resistively heated quartz crucible at a rate of 0.9 $nm \cdot min^{-1}$ to obtain single monolayer films according to the methods[151,152] The base pressure in the vacuum chamber during annealing and evaporation was $1 \cdot 10^{-8}$ mbar. Since mica and gold have similar sticking coefficients, i.e. nearly a value of almost 1, I assumed that the amount of sample on the surface may be considered similar.

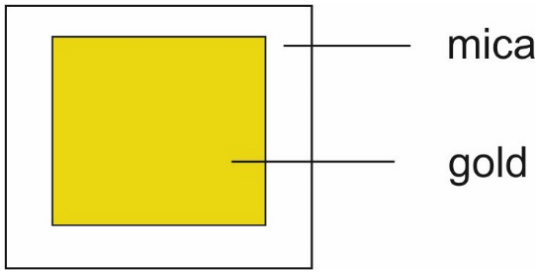

Figure 5.2 Substrate structure of Au(111) on mica.

Setup

Raman measurements were carried out on a confocal Raman microscope (XploRA ONE™, Horiba Jobin Yvon, Paris, France) with a 633 nm laser for illumination and with an 1800 cm^{-1} grating. A 532 nm laser was used for illumination coupled with a 2400 grooves/mm grating to determine the single layer graphene peak position and FWHM, which yields 2 cm^{-1}

uncertainties in measurement. A 100x objective lens (Mitutoyo, Japan) was used to focus the laser beam on the sample. The acquisition time was 30 s with a typical laser power of 2 mW at the sample stage.

Scanning force microscope (SFM) images were acquired with an AIST-NT scanning probe microscope on a bare gold surface. A medium-soft silicon cantilever from Olympus with frequency ≈ 80kHz was used for contact mode-SFM and images were recorded at 1 Hz.

Later, to establish a better understanding of the samples, samples were investigated using SFM imaging in quantitative imaging (QI) mode using Nanowizard III (JPK GmbH) operated with a 20x20 μm^2 scanner. QI images were recorded at a typical rate of 5-17 min per image. Silicon tips on silicon nitride cantilevers with a tetrahedral base were used with a typical resonance frequency of 70 kHz and a spring constant of 1.7 N/m. The tips exhibited a typical apex radius of 7 nm with an upper limit of 10 nm, having a tip cone half angle of 18 degrees, as specified by the manufacturer (Olympus Corporation). Experiments were carried out under ambient conditions. Deflection sensitivity was calibrated by acquiring force-distance curves on a clean sapphire surface (Bruker). Cantilever spring constants were calibrated using the thermal noise method.[153] Cantilevers were calibrated using spring constant and thermal noise calibration over a clean sapphire surface. QI images were made at approach and retraction speeds of 50-150 µm/s. Set points of 1 to 5 nN were used to image graphene over the gold surface coated with CuPc molecules. The SFM images were processed and analyzed with JPK supplied image-processing software.

Calculation of the enhancement factor

Here the assembled substrates effect (EF_1) was calculated by taking the intensity of CuPc sandwiched between GERS on the gold substrate and dividing by the intensity of CuPc deposited on mica. To compare solely the GERS effect (EF_2), I divide the intensity counts of individual molecule peaks of CuPc sandwiched between graphene and mica to the uncovered molecules on mica. Last, the GERS effect on gold (EF_3) was calculated by dividing the individual peak intensity of molecules under the graphene by the intensity of that peak of uncovered molecules on gold. EF_4 illustrates the substrate effect: enhanced signals from the gold substrate compared to that on mica.

5.3 Results and discussion

An important feature of the gold substrate is its flatness, needed to guarantee that the SERS-effect is CM-dominated. STM images (Fig. 5.3) revealed large grains and discrete single atomic layer step heights, reflecting the crystallinity of the employed Au (111) surfaces. Also SFM images (Fig. 5.4) confirm their flatness.

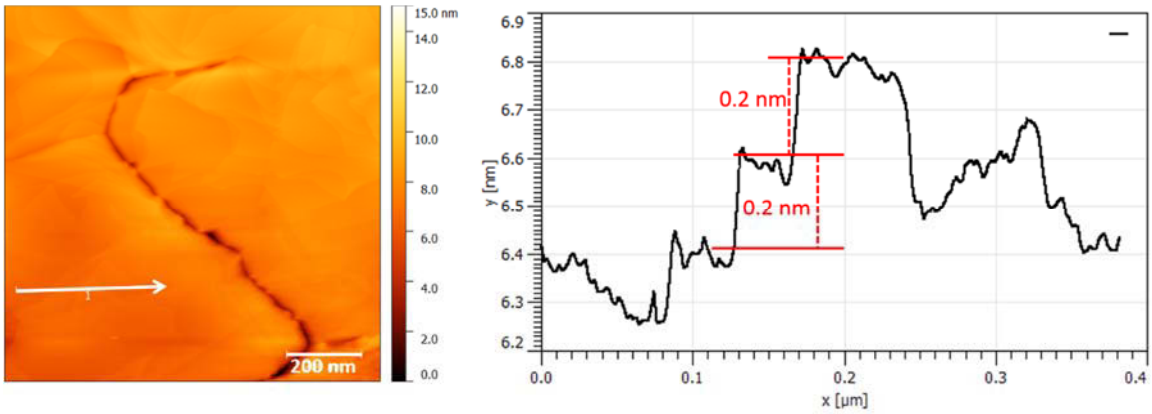

Figure 5.3 a) 1x1 µm² STM image of bare Au (111) surface. b) Cross-section profile indicated with arrow in a) showing the atomic steps of gold terrace.

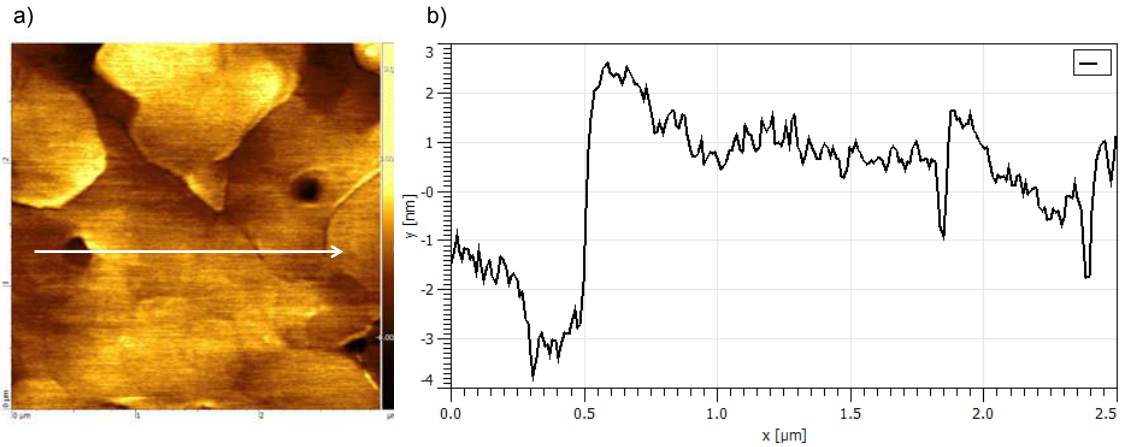

Figure 5.4 a) 3x3 µm² SFM image of bare Au(111) surface obtained in contact mode. b) Cross-section profile indicated with arrow in a) showing the flatness of the substrate.

The SERS-effect of the gold substrate is demonstrated in Fig. 5.5 a) and a figure with an enhanced scale is shown in Fig. 5.5 b). With respect to CuPc on mica, the Raman intensities were enhanced by a factor of 2-4, depending on the vibrational mode of the molecule. This relatively small enhancement factor indicates that the underlying mechanism is dominated by chemical enhancement on a flat gold surface.[18] The Raman spectrum of CuPc sandwiched

between single layer graphene and gold is plotted red in Fig. 5.5 a). By comparing intensity counts of the molecular peak at 1530 cm^{-1} (illumination at 638 nm), I observed a 68-fold signal enhancement for sandwiched CuPc between gold and graphene (combined GERS and SERS, red line), compared to the bare molecules on mica (no enhancement, green line). To compare the combined graphene and gold effect, I also measured the molecules on mica covered with exfoliated single layer graphene (GERS only, black line). Fig. 5.5 b) provides a blown-up scale to show the GERS-effect on mica and the substrate effect on enhancing molecules.

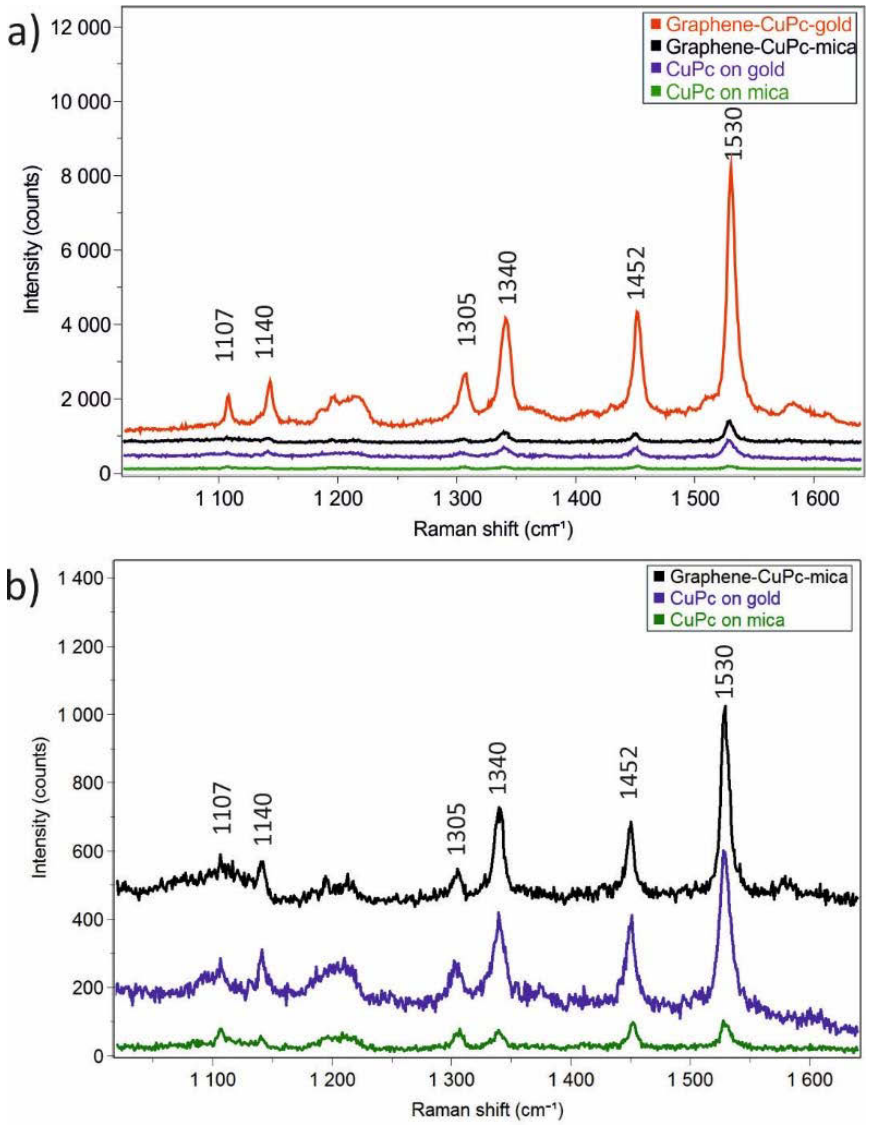

Figure 5.5 a) Raman spectra of CuPc sandwiched between graphene and gold (red line) as well as between graphene and mica (black line), CuPc on bare gold (blue line), and CuPc on mica (green line), all illuminated at 638 nm. b) Enlarged spectra of graphene-CuPc-mica, CuPc on gold and CuPc on mica, for better visibility to compare GERS and the substrates' effects. The spectra in a) and b) have been offset along *Y-axis* for clarity.

The enhancement factor (EF) of our work was obtained by using the signal intensities of nearby uncovered molecules to normalize the enhanced molecular signal intensities under the coverage of graphene,[154] similar to other GERS work[75].

In order to identify areas covered with single-layer graphene (SLG) and to probe their homogeneity, reflection microscopy[56] confocal Raman microscopy and scanning force microscopy in quantitative imaging mode (SFM-QI)[155, 156] were employed.

Raman spectroscopy is a powerful method to readily distinguish SLG from multilayers of graphene via the ratio of I_{2D}/I_G and the width of the 2D peak.[70] Fig 5.6 shows the Raman spectrum of single-layered and multi-layered graphene exfoliated on gold substrates and illuminated by light at 532 nm. The homogeneity of the CuPc distribution on the gold surface over 50 µm was confirmed with 60 pixel measurements, yielding only a 5% fluctuation in intensity (Fig 5.7). Since CuPc absorbs in the red spectral range,[157] it shows a resonance Raman-effect at 638 nm (Fig. 5.8). This hampers and interferes with the observation of the graphene peak intensity; hence I rely on the 532 nm illumination to verify the SLG features.

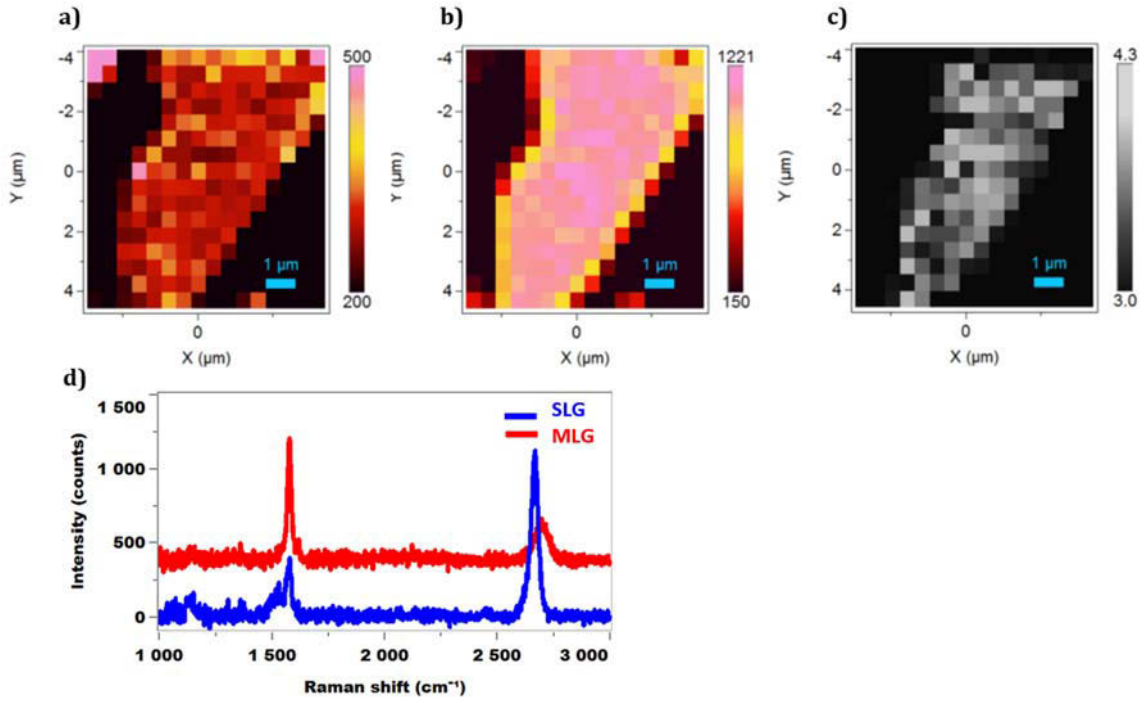

Figure 5.6 Raman spectroscopy of mechanically exfoliated single layer graphene on gold. Maps of integrated a) G-peak intensities, b) 2D-peak intensities, c) I_{2D}/I_G, and d) comparison of Raman spectra of single layer graphene (blue line) and multi-layered graphene (red line) illuminated by 532 nm light.

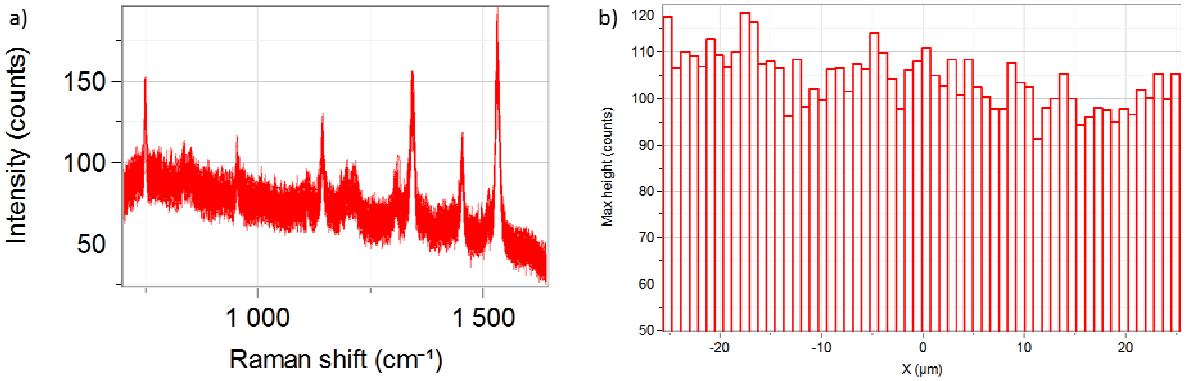

Figure 5.7 The signal homogeneity of CuPc coated on gold. a) The measured raw data over a 50 µm length scale with 60 spectra. A higher background at lower Raman frequencies is observed due to the gold substrate. b) The histogram of intensity counts of the peak at 1530 cm^{-1} yields an average value of 105 and a standard deviation of 6.13. (Peak was treated with background subtraction and single Lorentzian fitting). Illuminated with 638 nm light for 10 seconds.

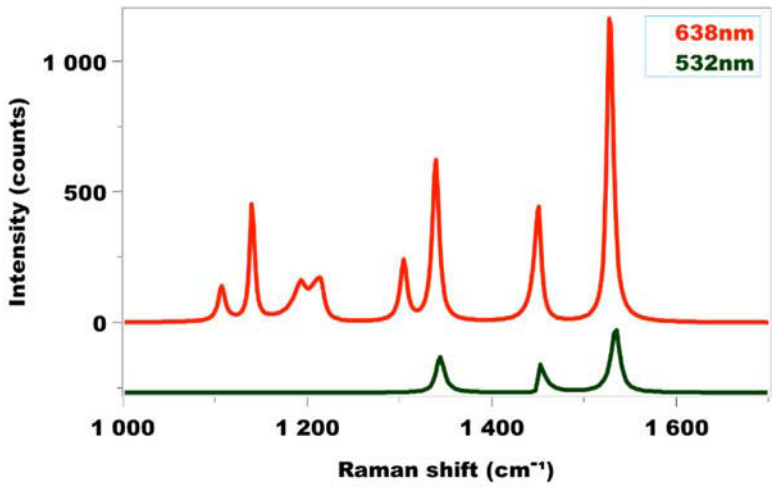

Figure 5.8 Spectra of CuPc on gold were acquired by illuminating with laser light at different wavelengths (638 nm and 532 nm). Upon excitation with the 638 nm laser, the peak intensities are much stronger than for the 532 nm laser excitation due to the resonance Raman effect. The fluorescence background from gold was subtracted to fit the baseline.

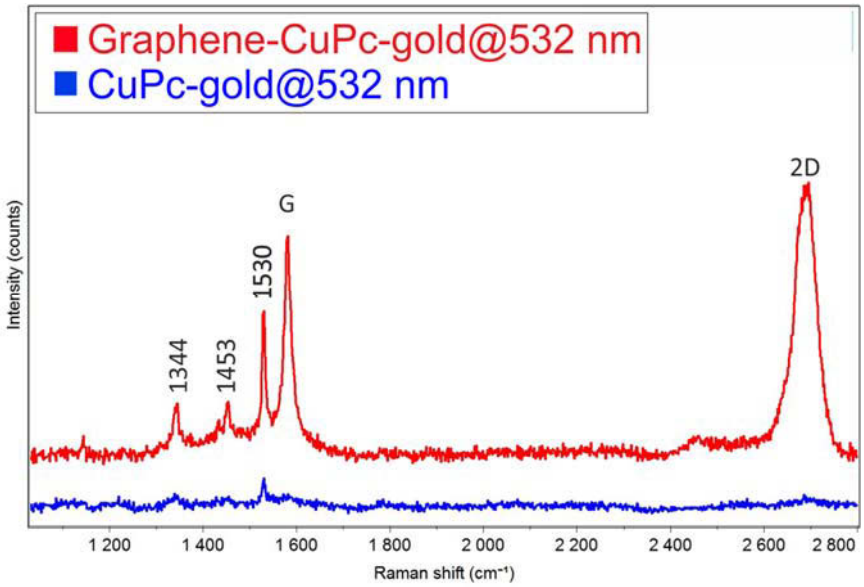

Figure 5.9 Raman spectrum of a single layer of graphene covering a CuPc-coated gold surface (red line) and spectrum of uncovered nearby molecule (blue line), using the same acquisition time and illumination (532 nm) conditions.

Fig. 5.9 shows the Raman spectrum of a SLG covering a CuPc-coated gold surface, illuminated by 532 nm light. The ratio of the integrated peak intensities I_{2D}/I_G is 1.43 for SLG on CuPc coated gold. The value is smaller than for undoped graphene[158] and the value of 3.0 for SLG exfoliated on gold (Fig. 5.6 c). I attribute this to charge transfer to the graphene and, concomitantly, a change of the electronic structure of the molecules below graphene. It was argued that the charge transfer between a molecule and graphene is the underlying mechanism of the GERS effect[17], thus generating enhanced Raman scattering. Furthermore, I find the 2D and G peak positions in our measurements to be 2691±2 cm^{-1} and 1584±2 cm^{-1}, respectively. However, with the presence of strain, it is difficult to separate the doping effect[72] from the strain effect[159] on the peak shift of graphene. Besides the peak shift, the widths of the G and 2D bands also show an effect of the deposition upon the molecule. The fitted FWHM of the G peak is 19 cm^{-1} and the FWHM of the 2D peak is 46 cm^{-1}. The peak broadening can be attributed to an inhomogeneity of doping and/or strain at the nanoscale. Therefore the measured resulting Raman spectrum of graphene reflects local fluctuations in the individual carrier densities and strain within the laser spot.[160,161,162]

Figs. 5.10 a), b) and c) display a full Raman mapping by measuring an area of 6.0x5.6 μm^2 with 15x14 pixels under illumination at 532 nm. (The same area illuminated with 638 nm was shown in Fig. 5.11. By integrating the Raman intensity of one selected peak at 1530 cm^{-1},

I get the distribution of the enhanced signals of CuPc (Fig. 5.10 a). The integrated intensity maps of the G (Fig. 5.10 b) and 2D (Fig. 5.10 c) bands confirm the presence and distribution of single layer graphene, where the integrated intensity of 2D band is larger than the one in the G band. Our mapping shows that that the distribution of CuPc is homogeneous and the graphene sheet can effectively enhance molecular signals. The enhanced CuPc signal in Fig. 5.10 a) corresponds well with the G and 2D maps in Fig. 5.10 b) and 5.10 c), and also with the SFM-QI image in Fig. 5.10 d). SFM-QI imaging demonstrates the material adhesion (snap-in) contrast based on the difference in the force of adhesion during approach of the tip to the surface, as extracted from force-distance curves. Fig. 5.10 d) distinguishes the areas coated with graphene (small adhesion) from uncoated areas (large adhesion). A zoomed height image and a stiffness image (slope of force-distance curve) along with the height analysis are shown and discussed in Fig. 5.12.

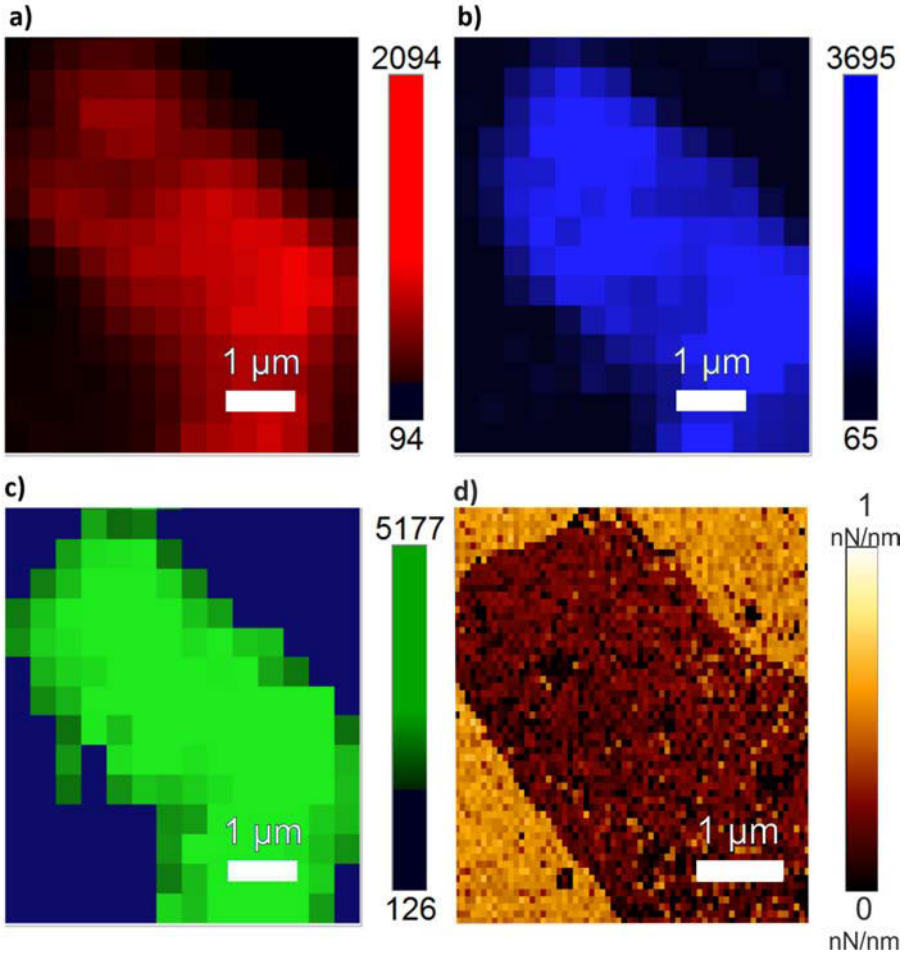

Figure 5.10 Integrated intensity map of a) one of the CuPc bands (1530 cm^{-1}). b) The G band of graphene and c) the 2D band of graphene under 532 nm illumination. Each pixel is 0.4x0.4 μm^2. d) SFM-QI imaging, showing slope image at setpoint force of 1 nN.

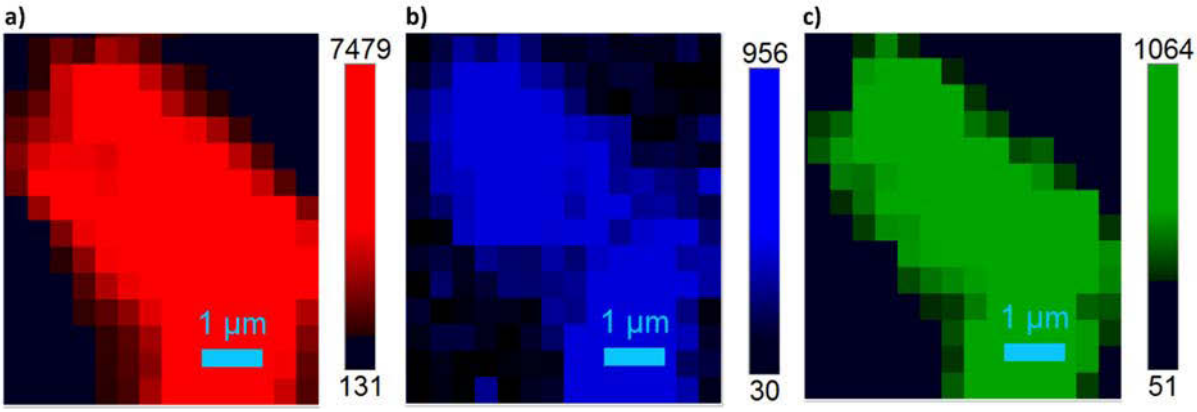

Figure 5.11 Integrated intensity map of a) molecule distribution (red), b) the G band (blue) and the 2D band (green) of a SLG sheet, illuminated at 638 nm for 30 seconds.

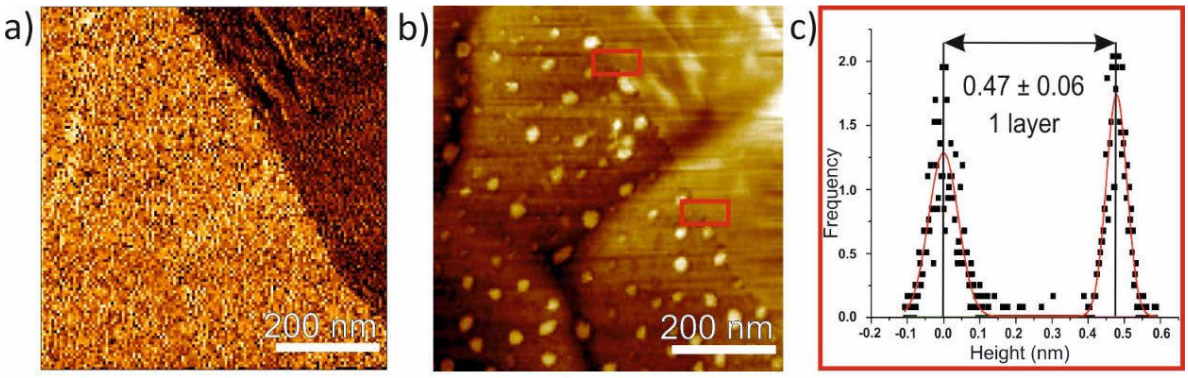

Figure 5.12 SFM-QI imaging. a) slope image at setpoint force of 1nN. b) Height image at contact point. c) Histogram of the height distribution from the selected areas in b) marked in red.

Fig. 5.12 a) with slope of force-distance curve at a setpoint force of 1nN allows one to distinguish the areas coated with graphene from uncoated areas. Fig. 5.12 b) presents a height image at the contact point with the sample, showing a region of the gold coated with CuPc and partially covered by a single layer graphene sheet. Upon fitting this to two Gaussians I obtained the histogram displayed in c), revealing a height difference of 0.47 ± 0.06 nm (error including standard deviation and instrument uncertainty in vertical piezo movement). The value is close to the interlayer distance of graphenes in graphite (0.34 nm). However, I do not exclude the unknown contribution of the interaction between graphene and substrate. I therefore attribute the corresponding area to a single layer of graphene. Note that there are also some particles appearing in the height images, which inevitably evolve from the ambient environment before or during the measurement. However, they do not influence our

measurements significantly, since the Raman intensity counts of the CuPc coated on gold corresponding to our laser spot size show good homogeneity in Fig. 5.7.

Table 1 Comparison of the enhancement effect. EF_1 is the factor of combined graphene and gold relative to mica. EF_2 is the GERS effect on mica, EF_3 is the GERS effect on gold and EF_4 is the substrate effect. Data were acquired with 638 nm light under the same acquisition conditions.

Raman shift (cm^{-1})	EF_1= combined graphene and gold effect	EF_2 = GERS on mica	EF_3 = GERS on gold	EF_4 = substrate effect (gold to mica)
1107	**11.3±0.4**	**3.0±0.5**	**4.3±1.0**	**2.7±1.3**
1140	**26.3±2.2**	**4.5±0.5**	**7.7±0.8**	**3.4±1.0**
1305	**20.7±1.4**	**1.7±2.8**	**5.6±1.0**	**3.7±1.7**
1340	**44.9±4.5**	**5.4±0.4**	**15.1±3.3**	**3.0±0.0**
1452	**32.5±2.7**	**3.0±1.0**	**8.3±4.2**	**3.9±1.1**
1530	**68.6±6.6**	**7.0±1.1**	**15.4±4.2**	**4.5±0.2**

Both graphene covered samples show that the enhancement depends on the vibrational mode. I calculated the enhancement factors to compare the enhancement effect of the substrates and the vibrational mode dependency for illumination at 638 nm (Table 1). To confirm the reproducibility of the GERS effect, the standard deviation was also calculated by extracting all data points in the Raman image. The variation in enhancement of molecular signals of the same peak could be accounted for the different local field polarizations of the molecule on the surface.[18]

The effect of the sandwich structure on gold shows extraordinary enhancements compared to that on mica. The observed EF is as large as 68 for the molecular peak at 1530 cm^{-1}, which corresponds to the estimated enhancement range for chemical enhancement.[163] It exceeds the previously reported highest value for GERS with CuPc as a probe of 47.3.[79] The enhanced GERS scattering on gold (EF_3) was found to be larger by a factor of 15.4 and the GERS on mica yields an enhancement factor of 7. The peak at 1530 cm^{-1} exhibits the most enhanced scattering, while 1340 cm^{-1} shows the second greatest. Both peaks are A_{1g} modes, corresponding to the symmetric isoindole ring vibration mode. The higher EF of these two peaks indicates that the isoindole ring is lying flat on the surface, such that the system exhibits a good coupling. As the GERS effect depends on the precise interaction of the molecules with graphene, the enhancement is molecule selective and vibrational-mode

dependent.[79] The GERS effect is stronger when the aromatic molecules have a molecular symmetry matching to that of graphene, where π-π interactions of graphene and the molecules in AB or AA stacking to the graphene exhibit strong molecule-graphene coupling and induce a relatively large interfacial diploe.[79]

According to calculations using time-dependent perturbation theory for the Raman scattering of molecules interacting with two-dimensional materials,[79] a strong GERS effect occurs when the phonon energy is close to the energy difference between the Fermi level of graphene (E_F) and either the HOMO or the LUMO states of the molecules ((ii) of Eq. (15) in ref. 151). This can be increased further when the laser excitation energy is close to the HOMO/LUMO energy gap of a molecule. [79] This may explain why the Raman peaks at higher wavenumber are enhanced more strongly. [79]

Our results confirm that sandwiching CuPc between graphene and gold can strengthen the chemical enhancement. This may be attributed to the fact that the employed laser photon energies of 1.9 eV (at 638 nm) and somewhat less so at 2.3 eV (at 532 nm) are close to the energy difference between the work function of gold (around 5.3 eV) and the LUMO of CuPc (around 3.5 eV),[79] since this allows for a photo-induced charge transfer between the metal surface and the molecules. On the other hand, the GERS effect has been attributed to a ground state charge transfer between graphene and the molecules. The chemical enhancements are expected to be multiplicative, [79] which may explain the very strong enhancement observed for the combination of both effects.

5.4 Conclusion and outlook

In conclusion, I have reported Raman scattering enhancement by a sandwiched molecular junction. By exposing the desired molecule to two mainly chemical enhancement dominated substrates at the same time, I demonstrate that the individual chemical enhancements can be increased further. An enhancement factor as large as 68 has been observed. I also revealed that the GERS effect still functions on a conductive substrate with an enhancement factor of 15, while the GERS on mica has an enhancement factor of 7. For the first time, the combined effect of two chemical enhancement-dominated substrates has been experimentally investigated. For a system where both enhancements occur simultaneously, I proved that the enhancement effects can add to each other.

Chapter 6

Graphene-enhanced Near-Field Raman Scattering

6.1 Introduction

Imaging with a resolution beyond the diffraction limit has been a long-standing goal in the field of optics.[1, 81, 164] The advent of Tip-Enhanced Raman Spectroscopy (TERS), which affords nanoscale spatial resolution has provided one solution to this goal.[83, 84, 86] TERS is a technique that combines the rich chemical information from Raman spectroscopy with the nanoscale lateral resolving capability of STM/AFM. The nanoscale imaging is enabled by the local field enhancement provided by a plasmonic tip with a nanosized apex, which is excited by a focused laser beam. This technique provides molecular resolution and sensitivity down to 15 nm at ambient conditions,[88] and even down to single molecules[26, 91-94] or submolecular spatial resolution[95] in ultrahigh vacuum. A tip with a single hot spot generates a strong electromagnetic field, and the enhancement factors of TERS can easily reach 10^4 and can be up to 10^7 under some circumstances.[83, 86, 165] To date, the use of TERS to study graphene has been applied to investigate the number of layers,[166] nano defects,[19, 20] edge boundaries,[21] local strain[22, 23, 167] etc., since Raman spectroscopy captures a large amount of information about graphene.

Graphene, a single-atom thick and two-dimensional flat material, exhibits a unique combination of optical and electronic properties. It is transparent but highly conductive. It is flexible but mechanically strong. It is chemically inert and the thinnest known material but impermeable to small molecules, thereby acting as a perfect ultrabarrier to, e.g., oxygen and water.[11] Furthermore, graphene has recently emerged as an enhancement material in Raman scattering, providing enhancement to molecules in its proximity.[17, 75] The large surface area of graphene inherently affords a marvelous platform for strong light-matter interaction. The unique features of graphene plasmons compared to noble-metal plasmons lie in their much tighter confinement, longer propagation distances, as well as being highly tunable via electrical gating.[168, 169] The use of graphene in microscopy is growing. For example, graphene can provide enhancement in subsurface and subwavelength imaging,[15, 170, 171] or act as a protection layer for a virus in water in infrared nanospectroscopy.[172] The expanding studies on graphene-enhanced Raman scattering (GERS) reveal that graphene is a promising material in the field of optics. [9, 173]

With previous chapter it has been shown that GERS can be improved further by employing a flat gold surface as the substrate for a molecular layer. A particularly high surface enhancement was observed through the use of two surfaces, Au (111) and graphene, implying the surface enhancements provided from two individual materials can be added to each other. Herein, I want to combine the merits of TERS and GERS to study graphene-covered molecules on a flat gold surface, since molecules trapped under a graphene sheet are well protected from chemical and physical degradation, and TERS - with its highly localized field - may possibly improve the Raman enhancements further to yield even higher Raman sensitivity or spatial resolution.

Even though TERS is on the verge of becoming a widespread analysis tool nowadays, it is known that with the scanning probe microscopy (SPM) method it is based on, the sample molecules are often physically moved or damaged. Incorporating graphene in TERS measurements allows one to immobilize the molecules since graphene is highly flexible so that it replicates macromolecules underneath[12, 174] and protects molecules from mechanical damage by the tip. Also, TERS generates a strong local field with locally increase temperature due to focused laser illumination, and may burn or cause the degradation of the underlying molecules. The use of graphene in TERS, as a good thermal conductor, provides favorable heat diffusion characteristics and protects molecules from chemical degradation under ambient conditions. In addition, TERS spectroscopy often suffers because the tip can pick up sample molecules; this may also benefit from the protection of a graphene layer.

Moreover, this novel approach may impact future research on single molecule detection, since in this fashion the molecules encapsulated by graphene are unlikely to diffuse across the surface, and perhaps even higher enhancements may be provided due to the additional enhancement from GERS effects. Also, very high spatial resolution might be possible, because temperature-induced or field-induced diffusion and reorientation of the molecules trapped under the graphene might not be an issue.

In the present study, I carried out TERS measurements on a self-assembled monolayer of oligomers (thioacetic acid S-[4-[4-(phenylethynyl)-phenyl]ethynyl]benzene-thiol ester, as an OPE) on gold, covered with a single layer of graphene (Scheme 1). Since graphene has been shown to provide additional enhancement of Raman signals of nearby molecules,[75] I wondered whether I could excite graphene plasmons through the evanescent field[168] generated from the tip. This geometry would also make graphene a promising candidate for encapsulation of molecules for TERS investigations.

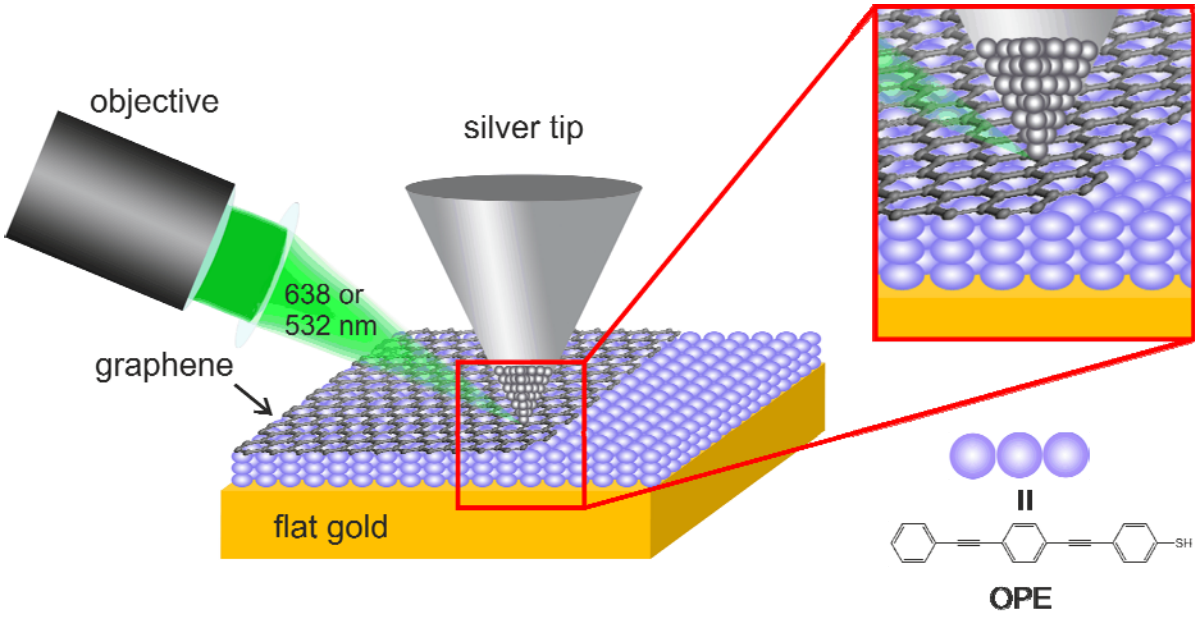

Scheme 1. The sample and the method.

6.2 Experimental methods

Sample preparation

OPE modified gold surface. Au (111) on mica (4x4 mm, #20020020) was obtained from Phasis, Geneva, Switzerland. Thioacetic acid S-[4-[4-(phenylethynyl)phenyl]ethynyl]benzene-thiol ester (OPE) was purchased from Sigma Aldrich. Deprotection of OPE was accomplished by hydrolysis of thioacetate in ethanol (0.5 mM) by adding NaOH to the solution (10 µL, 1N) as a hydrolyzing agent. Au (111) was immersed in the ethanolic thiol solution for 24 h at room temperature.

Transfer graphene on modified gold surface. Chemical vapor deposition (CVD) produced graphene on Cu foils was purchased from Graphenea, Spain. The graphene on Cu was covered with poly(methyl methacrylate) (950 PMMA, A4, MicroChem, MA, USA) by spin coating (20 rps, 1 min) and dried in air overnight. Graphene on the reverse side of the Cu sheet was removed by oxygen plasma cleaning (10W, 1min). The Cu-graphene-PMMA stack was placed on the surface of a Cu etchant (1M $FeCl_3$ in water). After completing the Cu etching (~30 minutes), the graphene-PMMA layer was scooped out with a clean glass into several sequential baths of deionised water for rinsing. Isopropanol was added to water (5%) to reduce the surface tension in the last batch before scooping it out with a gold surface modified with self-assembled OPE molecules. Finally it was dried in air overnight before immersion in several baths of clean acetone to dissolve the PMMA, followed by rinsing in isopropanol and drying with ultrapure nitrogen.

TERS tips. Silver wires (diameter 0.25 mm, 99.99% purity, Alfa Aesar, Germany) were electrochemically etched at a voltage of 10 V in a 1:4 (v/v) mixture of perchloric acid (70%, Sigma Aldrich, Germany) and pure ethanol (p.a., VWR, Germany), see chapter 3.5. The tip was afterwards mounted on the tip holder of the Horiba nano-Raman system, and stable tunneling feedback was established.

Methods

TERS. TERS was performed on the sample in air using the STM mode. A 100x objective lens (NA 0.7; Mitsutoyo) was used to focus light from the side onto the apex of an STM-type etched TERS silver tip at a 60° angle with respect to the sample plane. Laser excitation wavelengths of 532 nm and 638 nm were used for the TERS measurements to satisfy and compare the resonance conditions for plasmon coupling. The TERS signal was collected with the same objective lens used for the illumination and passed to a spectroscope inside an XploRA PLUS (Horiba, Ltd.) confocal Raman microscope. The TERS tip was mounted with its

axis parallel to the focal plane of the objective lens, which polarized the light parallel to the tip axis to achieve efficient plasmonic oscillation and suppress shadow effects caused by the tip itself. An acquisition time between 2 s to 60 s was used for the acquisition of each TERS spectrum. Hot spot localization was accomplished by scanning the objective over the tip apex. TERS near-field and far-field signals were obtained by focusing the laser on the hot spot of a tip and focusing 3 µm away from the hot spot along the X-axis, respectively.

STM The surface topography of the graphene-covered sample was imaged using the STM mode on a Smart-SPM (OmegaScope-R, AIST-NT, Inc.) microscope with a side-cut PtIr tip to check the cleanliness of transferred graphene and features of the surface.

6.3 Results and discussion

Figure 6.1 provides high resolution STM height (a and c) and current (b) images acquired with a PtIr tip to illustrate the surface features of the graphene covered OPE molecules on a gold surface. The large area, 4x4 μm^2 shows the clean surface of the transferred graphene and large flat gold grains. The crystallinity and flatness of a bare gold surface was confirmed with SFM and STM in chapter 4 and 5.

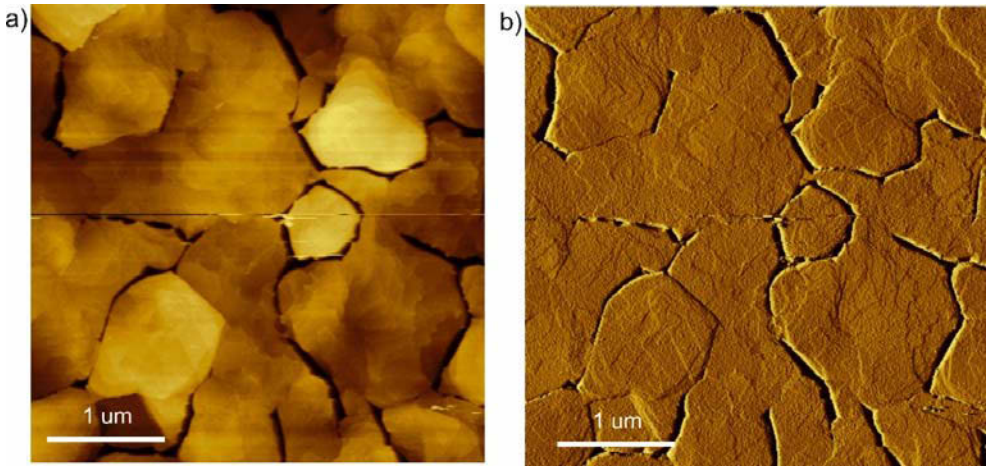

Figure 6.1 STM images of a transferred graphene layer covering OPE molecules self-assembled on a gold surface, acquired with a PtIr tip. a) STM height image, and b) tunneling current image of a large scale (4x4 μm^2). Images were acquired at 0.1V, 0.1 nA

Figure 6.1 a) indicates that the thin and highly flexible graphene follows the underlying surface features, which is mainly the gold substrate. It is known that self-assembled molecules growing on a gold surface adopt the structure of the surface due to chemisorption.[102, 175, 176] The morphology of self-assembled organic thiols acts as an adlayer to the crystal structure of the surface layer of gold. Defects at gold step edges or at gold grain boundaries, and vacancies of the gold surface can influence the adsorption of the molecules.[102, 177] Also, graphene is reported to replicate underneath molecules.[12, 178 179, 180] Figure 6.1 b) displays the tunneling current image corresponding to figure 6.1 a), and figure 6.1 d) plots the height profile along the white line in figure 6.1 c). It is hard to discern the molecular orientation and domains from high resolution STM images of molecules on a gold surface (not shown).

Raman spectroscopy provides high chemical specificity. In order to ensure a reliable system of a sample molecule, I measured a TERS map (fig. 6.2 a) to verify the consistency of OPE signal intensities. The chosen sample molecule OPE shows its characteristic bands in the TERS spectrum (fig. 6.2 c) at 1002, 1023, 1077, and 1580 cm^{-1}, which are signals due to

aromatic ring vibrations; the peak at 1129 cm^{-1}, assigned to a v(C-H) in-plane mode is only observed and pronounced in molecules with three phenyl rings.[136] The peak at 2214 cm^{-1} is due to the vibration of triple bonds. By integrating the signal intensity of the triple bond, I obtained the signal variations of OPE molecules in a map. Figure 6.2 a) shows a good homogeneity of the tip-enhanced Raman signal of OPE molecules at the nanoscale in a 500x500 nm^2 map. The signal intensities exhibited only 13 % fluctuations over the two flat grain areas of the gold surface. It is noteworthy that there are signal drops in the map, which corresponds to the gap between the two grains of gold, indicated by the STM topography image, displayed in figure 6.2 b). The STM topography was acquired simultaneously during TERS mapping. The boundary of two grains is visible even with low-resolution STM imaging. It is known that the TERS signal intensity is sensitive to the underlying features of a metallic surface.[181] A sharp 2 nm nanostep can influence one order of magnitude in signal intensities.[45]

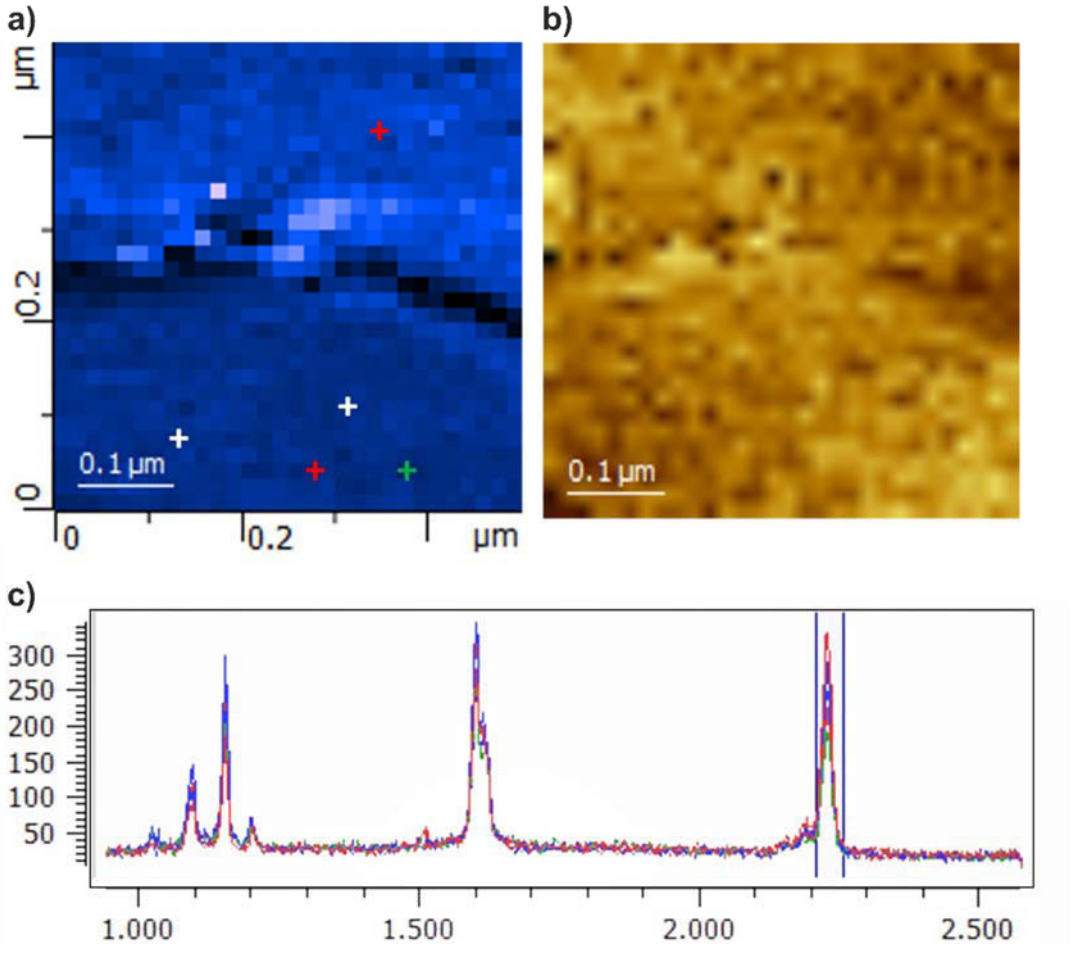

Figure 6.2 TERS mapping on self-assembled OPE monolayer on gold (111) with a Ag tip in an area of 500x500 nm^2, measured with 30x30 pixels, a) an integrated intensity map of the OPE peak corresponding to the triple bond, b) STM topography acquired at the same time, and c) randomly selected representative spectra of OPE. Illuminated by 638 nm, 500 µW, 2 sec.

Figure 6.2 c) displays the characteristic OPE spectra, randomly selected from the TERS mapping indicated with crosses in figure 6.2 a). The spectra show that there are some fluctuations of the peak ratio of ~1580/~2214 cm^{-1}around a value of one. The fluctuations of this peak ratio could be accounted for by molecular orientation with respect to tip and surface. However, the entire map still possesses rather good homogeneity of 2214 cm^{-1} peak intensities as mentioned above.

The strongest bands of the OPE molecule are at 1129, 1580 and 2214 cm^{-1}, which may be chosen as a marker of the molecule. Since the peak at 1580 cm^{-1} is overlapping with the Raman peak of graphene and the peak at 1129 cm^{-1} is too far from the 2D band of graphene for the detection range of any grating, 2214 cm^{-1} is selected to represent OPE molecules hereafter.

Raman spectroscopy is also a strong and nearly exclusive tool to identify graphene, and yields a high throughput in characterization. The Raman spectrum of graphene is characterized by three main fundamentally different phonon modes named as G band (~1580 cm^{-1}), 2D (~2700 cm^{-1}) band, and D band (~1350 cm^{-1}). The D band is due to a defect-induced vibration, which is only present at the edge or at defects within a graphene layer. The G band arises from all the in-plane sp^2 bond stretching in rings, while the 2D band corresponds to a second-order Raman process, originating from the in-plane breathing-like mode of the carbon rings.

Figure 6.3 shows a large area TERS mapping on the border of areas of graphene-covered OPE molecules and bare OPE molecules. Since the OPE molecules also have a peak at ~1580 cm^{-1} corresponding to an in-plane sp^2 carbon system, I integrate the 2D band to represent the distribution of graphene.

Figure 6.3 a) provides an integrated intensity map showing the fluctuation of molecules` intensities over a map, where the area with the weaker molecular signals corresponds well to the graphene-covered area in the integrated intensity map of the 2D band in figure 6.3 b). The bare molecular area exhibits stronger signals while the graphene-covered area shows much weaker and nearly no OPE signals. Figure 6.3 c) provides the STM height, which also displays a segregated border corresponding to the area with graphene and without graphene in the TERS map. As the STM topography was acquired with TERS mapping simultaneously, it is difficult to deduce the thickness of a single-atom thin layer of graphene. The underlying reasons are that the height profile is provided from coarse resolution over a wide area (i.e. 100 nm/pixel) and it may also contain the thermal drift resulting from long measurement times for TERS.

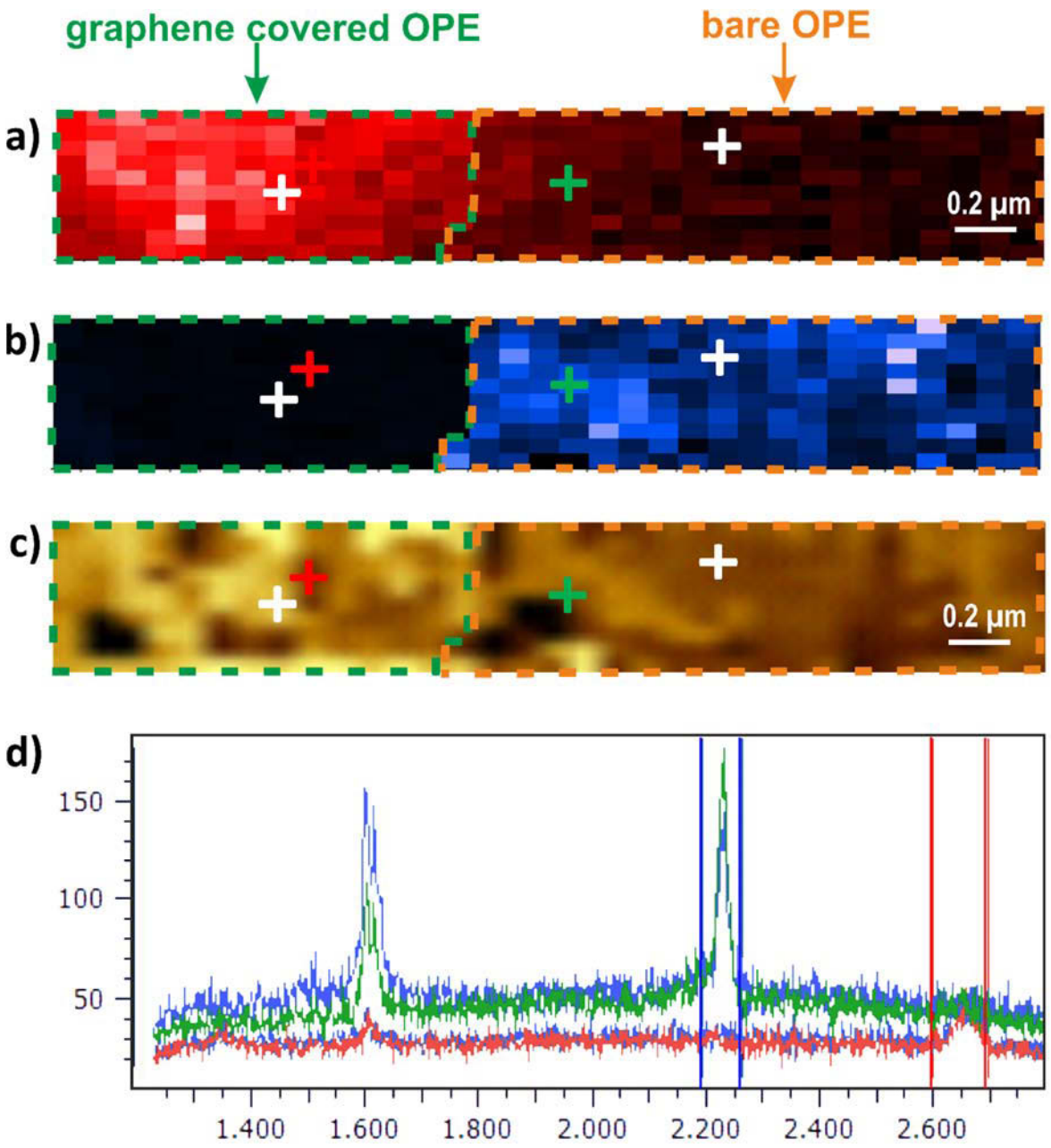

Figure 6.3 A TERS map of a 4.0x0.4 µm^2 area acquired with 40x10 pixels on the border of graphene-covered and bare OPE molecules assembled on a gold surface. Integrated intensity maps of a) graphene at 2D band, and b) OPE molecules at triple bond. c) Simultaneously acquired STM height, and d) representative spectra of some pixels in the TERS map. TERS is recorded under illumination at 638 nm, 500 µW, 2 sec at 0.1 V, 0.1 nA.

Figure 6.4 a) represents a typical TERS spectrum of bare OPE on a gold surface, which is classically referred to as gap-mode TERS. The characteristic band of OPE at 2214 cm^{-1} is strongly enhanced compared to the far field spectrum without the tip (Fig. 6.4 d)).

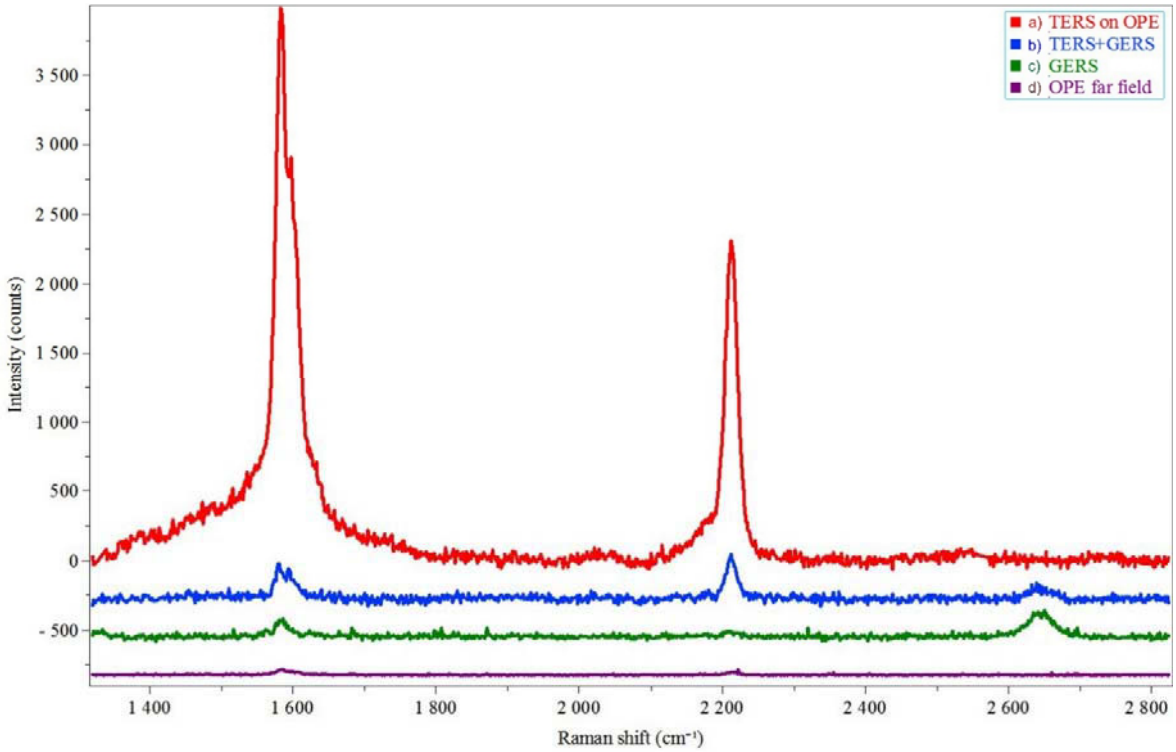

Figure 6.4 Raman spectra of OPE molecules assembled on a gold surface a) TERS on bare OPE area, b) TERS on graphene-covered area, c) Raman spectrum of graphene-covered OPE molecules without a tip and d) far-field Raman spectrum of bare OPE molecules. All spectra were obtained with illumination at 638 nm, 1.25 mW for 60s. Spectra were background subtracted and displayed offset along *Y-axis* for clarity.

Taking account of the far-field intensity and the near-field intensity produced by the molecules underneath the tip, this basically constitutes the contrast factor, defined as

$$C = \frac{S_{near-field}}{S_{far-field}} = \frac{S_{tip} - S_f}{S_f} = \frac{S_{tip}}{S_f} - 1$$

When the area and the depth of the focus of far-field and near-field contributing to TERS are also considered, an estimation of the TERS enhancement factor can be carried out.[165] Since the molecular layer here is sufficiently thin, one may normalize the illumination area by the square of the light focus diameter ratio $\frac{V_{ff}}{V_{nf}} \approx (\frac{R_{focus}}{R_{tip}})^2$. Thus the enhancement factor

for gap-mode TERS is found to be $= C(\frac{R_{focus}}{R_{tip}})^2 = 8.1x10^5$. Here, R_{focus} is taken as 1000 nm and R_{tip} as 15 nm. This EF corresponds well to the lower boundary of the reported TERS enhancement[83, 86] multiplied by the additional reported enhancement from gap-mode without molecules in resonance. Here the lower boundary of our measurement is compared with the lower boundary of the literature, since the EF is easily possible to over- or under-estimate due to variations in the tip's radius, focused laser radius and the angle of incidence. Figure 6.4 b) provides the TERS spectrum with the tip landing on a graphene-covered OPE molecules area. The molecular peak at 2214 cm^{-1} is stronger than the one without the tip (Fig. 6.4 c)). Similarly, I calculate the EF on the graphene-covered area with the tip and without the tip, which yields an $EF = 3.5 \times 10^4$. The tip with only a single hot spot can enhance the GERS effect further by four orders of magnitude. This combined enhancement from tip and graphene is sufficient to see weakly scattering molecules while being protected under graphene. [182,183]

Since TERS provides a tip-dependent enhancement, I carried out the same experiment with seven tips to compare the contrast factor C in graphene-covered and bare molecules areas (gap-mode TERS). The bare molecule area has a mean C value of 715 with a standard deviation value of 294, while the graphene-covered area has mean C value of 57 with a standard deviation value of 25. This implies that the enhancement effect of TERS on graphene-covered area drops by a factor of about 10.

The bare molecular area is the typical configuration for gap-mode TERS, which involves the coupling of a gold surface to a silver tip. A new surface plasmon resonance might be generated[184,185] and this coupled plasmon resonance provides a strongly localized and highly confined electromagnetic field between the tip and the gold surface. Figure 6.4 a) shows that the molecules sitting in this strong field make use of this confined EM field, manifested by strong Raman scattering. The incorporation of graphene into gap-mode TERS decreases the enhancement effect by a factor around 10, indicateing that graphene might exhibit some shielding effect or cause damping of the coupled plasmon of a silver tip and a gold surface. This is possible because the underlying mechanism of gap-mode TERS is mirror dipoles from the surface of the metallic substrate being induced by a metallic tip. Since the gold surface is easily polarized, a counter charge of the tip can be readily induced. On the other hand, graphene is not as polarizable as gold, therefore there are less dipoles induced. This might explain why the gap-mode TERS effect is less pronounced with the presence of graphene and why the graphene is showing some shielding effect to the gold surface.

Comparing figure 6.4 c) and d) gives the graphene-enhanced Raman scattering effect. The EF is a value around 2.5. Note that the GERS effect in my system here shows a relatively small EF in contrast to the reported values.[79] Since the GERS effect is highly molecule selective and dependent, as well as OPE being simple aromatic molecules and self-assembled with its long axis normal to the surface of gold and graphene, the induced interfacial dipoles are much weaker and the Raman scattering is less enhanced.

It is also known that TERS is a tip-surface distance sensitive technique.[186] I accordingly measured the OPE signal intensity variations with increasing separation of tip and surface to ensure the drop of the signal intensities is not a result of increased tip-surface separation. Figure 6.5 a) shows the bare OPE TERS spectra (waterfall plot) acquired as a function of the tip-surface separation distance. Figure 6.5 b) shows the signal intensity curve going to a plateau when the separated distance increased to 3 nm, producing three pronounced peaks. This means that the variations of the TERS signal intensities are due to the enhancement effect of the tip and the surface, instead of internal fluctuations of molecules. The decay features are in accordance with the reported data, where the curve also shows exponential decay and the signals go to a plateau at the increased separation distance at around 4 nm.[186] This is understandable since the employed molecules have different Raman cross-sections showing different Raman strength. Also, a comparison with the background profile (black curve) indicates that the enhancement effect reaches zero only when the separation is more than 10 nm.

Since with the presence of graphene, the OPE signal intensities drop by an order of magnitude, while with the separation of tip and surface separated by a distance of 0.34 nm, the bare OPE signal intensities only drop by 10 % as maximum. I then ruled out the concerns about the decrease of TERS enhancement as a result of an increased separation between tip and surface due to the introduction of a single atomic thin graphene layer. The study also shows that with the tunneling current the separation between graphene and the metal surface is slightly increased to 0.39 nm.[187] Though the tip-surface distance is raised with the same applied voltage and constant current conditions, the drop in enhancement effect far outweighs the distance effect.

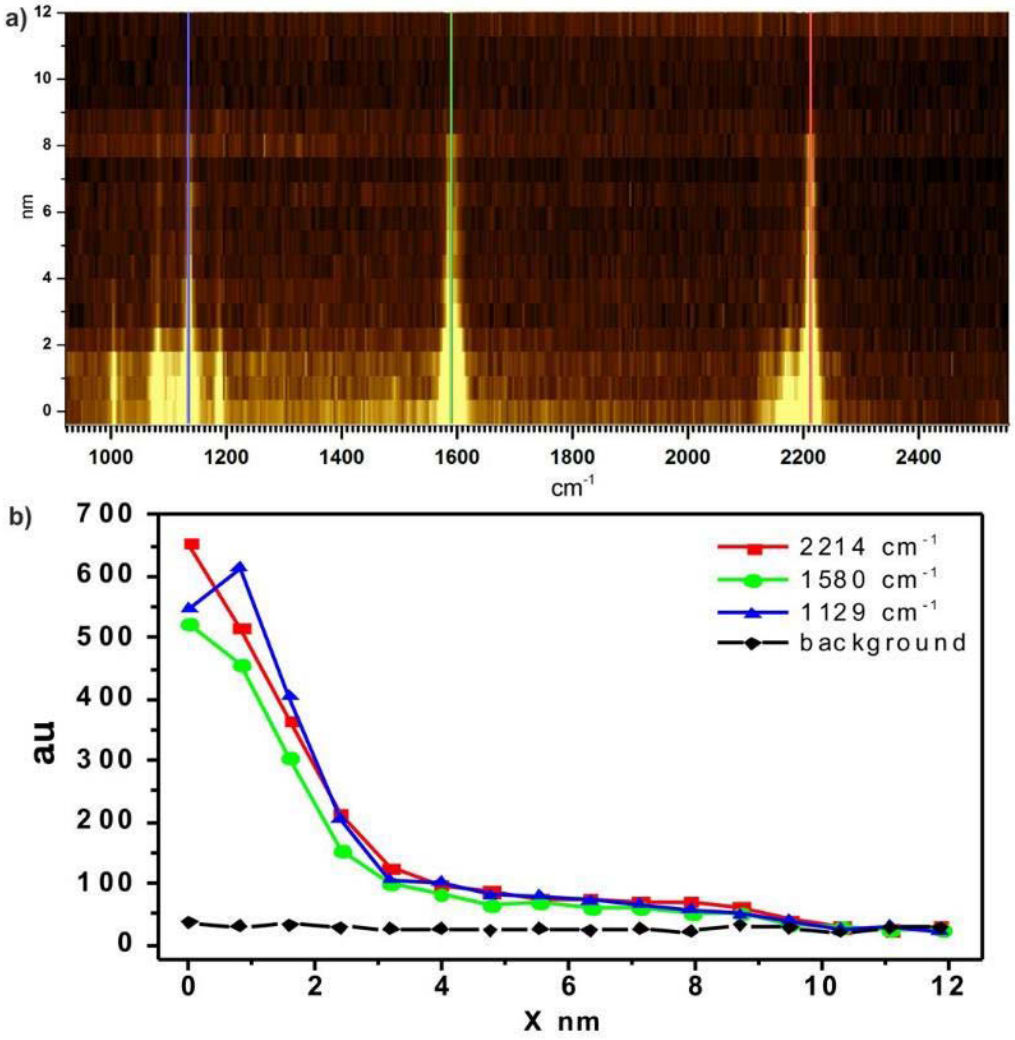

Figure 6.5 a) Bare OPE TERS spectra in a waterfall plot as a function of tip-surface separation. The three indicated straight lines are the intensity profile of the peak at ~1129 (blue line), ~1580 (green line) and ~2214 cm^{-1} (red line) shown in b). b) Intensity profile (peak height) with increasing distance between tip and surface from 0 to 12 nm. STM set point, 0.1 V and 1 nA. Illuminated at 638 nm for 2 s.

To reinforce the hypothesis of the shielding effect from graphene, I then, likewise, acquired the OPE TERS signal intensity variations in the graphene-covered area with the increased separation of tip-surface distance. The intensity is normalized to the initial point (by maximum peak height, black line) and, together with the bare OPE TERS spectra (red line), is shown in figure 6.6 to compare the signal decay as a function of the tip-surface separation distance. The curves were also addressed with linear fitting before the signals went down to a plateau. The slope of the black curve is 0.61 nm^{-1}, whereas for the red curve it is 0.29 nm^{-1}. This indicates that the molecular signals under the graphene cover drop faster and reach the

plateau sooner than without the coverage of graphene. The result shows that the decrease of signal intensities is not only due to the tip-sample separation being increased by the height of graphene, but also graphene exhibits some shielding effect to the gap-mode TERS. Therefore, the effective signals from the TERS effect are lowered in the same z range under the coverage of graphene.

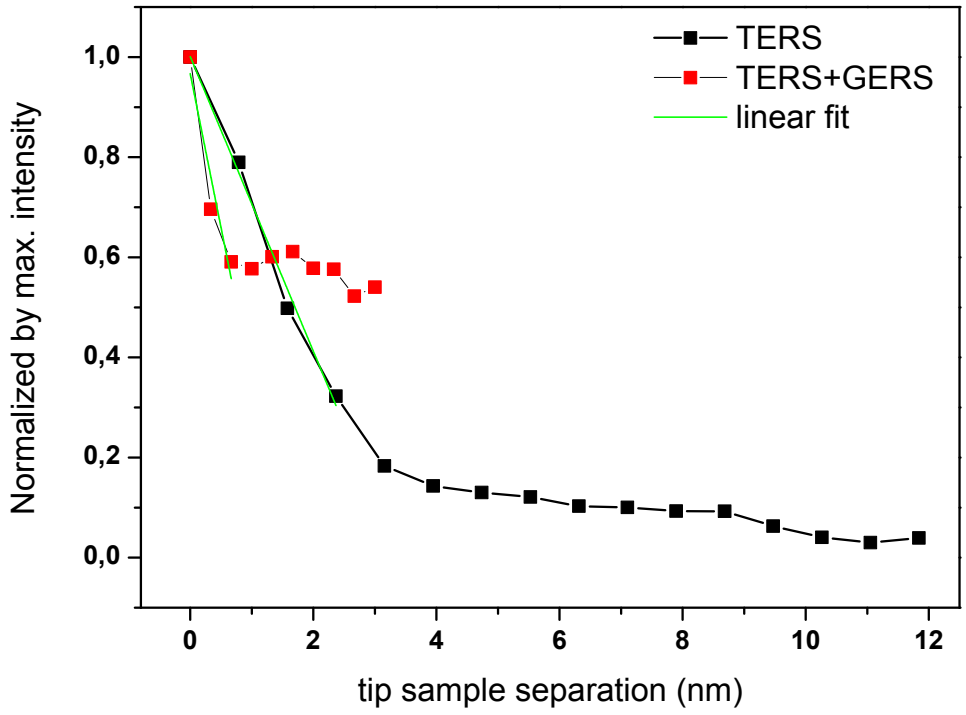

Figure 6.6 Normalized tip-approach curves with increasing distance between tip and surface. Black line represents the TERS spectra of bare OPE, and red line corresponds to the TERS spectra of graphene-covered OPE area. Illumination at 638 nm and set point at 0.1 V, 1 nA.

I also illuminated the system at 532 nm (fig. 6.7) to compare the resonance conditions with 638 nm. The EF is 6.8×10^4 for bare OPE in TERS compared to far-field OPE molecules, while $EF = 1.6 \times 10^4$ for a tip enhanced graphene-covered OPE area compared to without a tip. The results show that both wavelengths can enhance the Raman scattering further, and the illumination at 638 nm is generally better than at 532 nm within an order of magnitude. This trend persists with the coverage of graphene.

It may also be argued that there is a combination effect of graphene with the gap-mode TERS. It may couple the plasmon resonance of tip and graphene, or may not. The results imply that if there is plasmon coupling between the tip and graphene, the new generated plasmon resonance may have shifted to a new resonance position, thus the whole system does not demonstrate a strong resonance effect under a given visible wavelength excitation. It also confirms that the graphene plasmon band is not in the visible range. It is recently reported that the plasmon resonance between an 80 nm gold particle and a gold surface can be shifted by precise control of the layer number of graphene as a spacer.[53] Their result shows that with the separation of a single layer graphene in the confined space between a gold nanoparticle and a gold surface, the coupled plasmon resonance is red-shifted to the near-infrared range.[188]

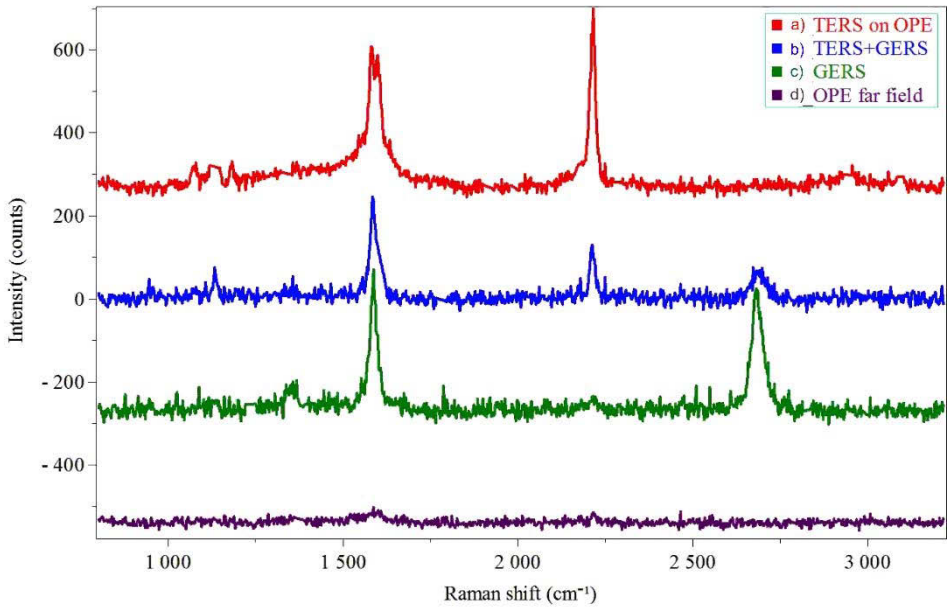

Figure 6.7 a) TERS spectrum of bare OPE molecules on gold, b) TERS spectrum of graphene-covered OPE molecules, c) Raman spectrum of graphene-covered OPE molecules without a tip and d) far-field Raman spectrum of a bare OPE molecules on gold. All spectra were illuminated with 532 nm light for 60 s. Spectra were background subtracted and displayed offset along *y-axis* for clarity.

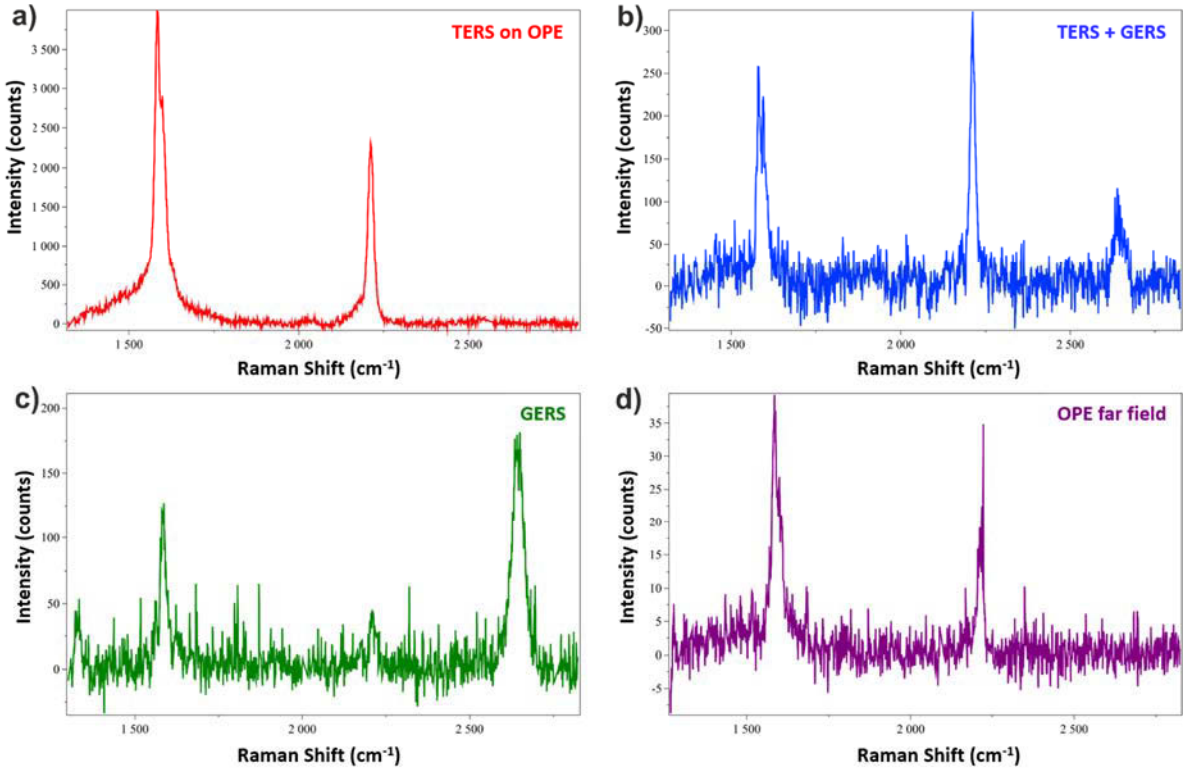

Figure 6.8 A blow-up scale of Raman spectra in figure 6.4, illumination at 638 nm.

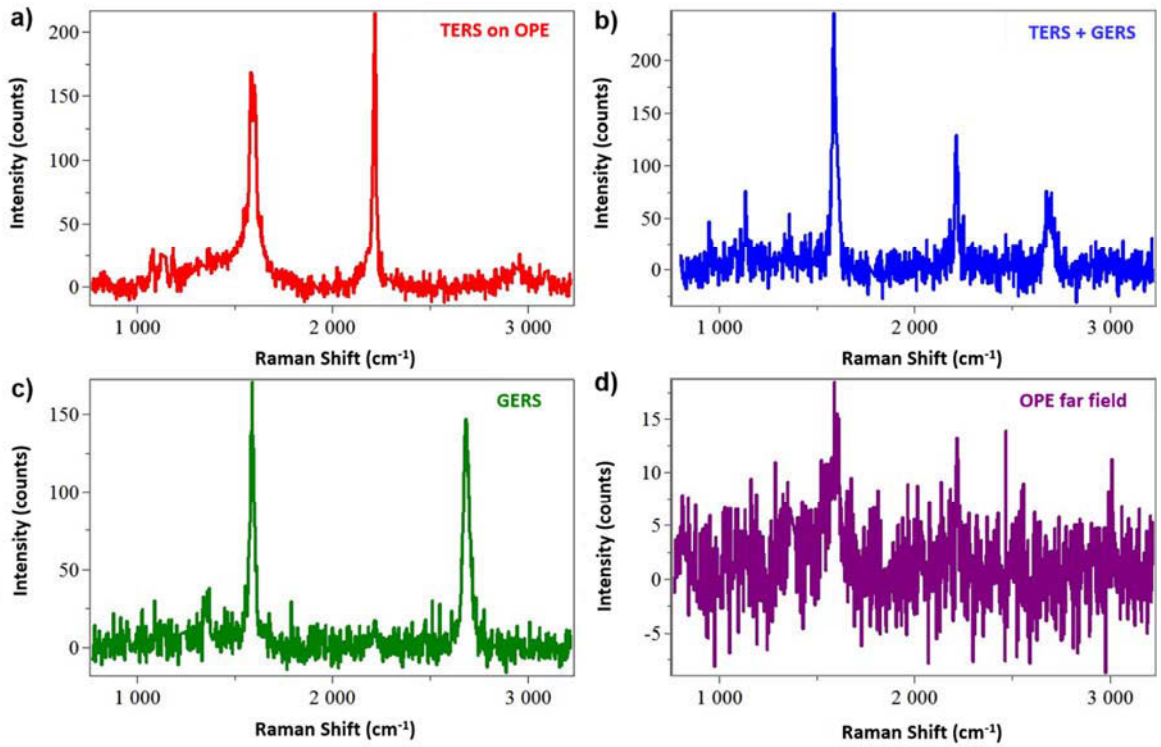

Figure 6.9 A blown-up view of the Raman spectra in figure 6.7, with illumination at 532 nm.

Figure 6.8 and figure 6.9 provide an enhanced scale of figure 6.4 and figure 6.7, respectively. The measured spot of graphene on a OPE modified gold surface gives a G peak at 1586 cm^{-1}, and a 2D peak at 2682 cm^{-1}, while tip-enhanced graphene shows the G peak and the 2D peak at 1586 cm^{-1} and 2687 cm^{-1}, respectively.

6.4 Conclusion

In this study, I transferred CVD grown graphene on top of a gold (111) surface modified with a self-assembled monolayer of OPE molecules. OPE is used as a sample molecule to monitor the strength of the Raman enhancement effect. The results show that the GERS enhancement factor is around 2.5 for OPE molecules bound to the gold surface. This EF is rather small compared to other reported GERS EFs, since OPE molecules are rather small molecules and are arranged normal to the graphene surface. Moreover, I employed TERS to investigate the possibility of further enhancements in addition to the graphene under visible light illumination: specifically, TERS is used to generate an evanescent field and can be expected to excite a plasmon in graphene through it. The results show that a sharp silver tip provides a large enhancement in the local electromagnetic field, both on a bare OPE and a graphene-covered OPE area. The tip can enhance the molecular signals under the cover of graphene by a factor of about 10^4 without using a resonance molecule, which is in accordance with the enhancement of TERS on glass with resonance molecules. This indicates that the EF is strengthened, and this strength is sufficient to be applied in future studies on molecules with small Raman cross-sections. However, I also note that with the presence of a graphene layer, the enhancement effect of classical gap-mode TERS is reduced, both at 638 and 532 nm illumination. This implies that graphene exhibits some shielding effect to induced dipoles in the gold surface for gap-mode TERS, and this may be due to inherently less polarizable features of graphene. With these facts, it may also appear like there could be a new generated plasmon band resulting from the coupling of a tip to the graphene and the gold surface, which is at a different resonance to the tip coupled with the gold surface. While TERS in gap-mode provides the strongest localized and most highly confined EM field between the tip and the gold surface, and it enhances molecules sitting in between the most, future studies on improving GERS enhancement at its resonance may lead to the same geometry for molecules between the tip and graphene under desired excitation wavelengths, where the strong resonance of a localized nanocavity can be created.

Chapter 7

Summary and outlook

The interaction between light and matter at the nanoscale may give rise to novel electronic and optical phenomena. When photons strike a metal surface, they excite plasmons in its vicinity and enhance the optical near-field. This thesis focuses on the study of enhanced Raman scattering of molecular systems in the vicinity of, or deposited on, a flat gold surface, graphene, a metallic tip, or a combination thereof. Individual enhancements by these materials were all measured independently, as well as for combinations of these materials. Graphene is a newly emerged surface enhancement material. Couplings of graphene to a flat gold surface and to a metallic tip were employed in novel ways, particularly by sandwiching molecules between graphene and a flat gold surface. The optical response of the molecules reflects the enhancement effect.

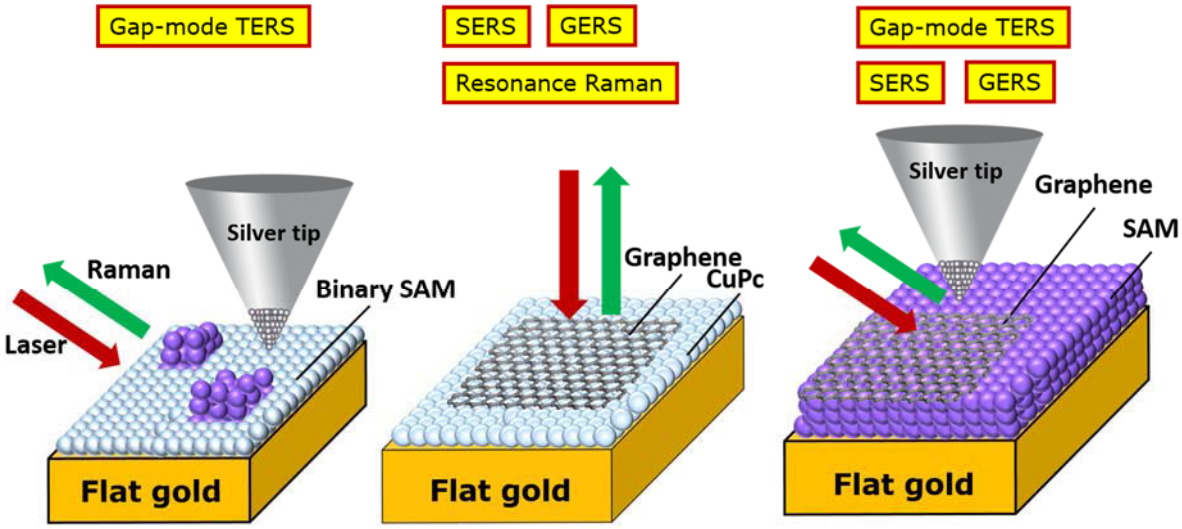

Figure 7.1 Schematic summary of the projects

In the first part of the thesis, the coupling of a silver tip to a gold surface was used to excite a strongly confined electromagnetic field by laser light, which was exploited to render a layer of molecules sitting on the surface spectroscopically “visible”. These molecules were prepared from a mixed solution of two thiols, by soaking a gold surface in the solution for 24 hours to allow molecules to self-assemble and re-order on the gold surface. These molecules were thioacetic acid S-[4-[4-(phenylethynyl)-phenyl]ethynyl]benzene-thiol ester (OPE; three

aromatic rings) and thiolphenol (with a single aromatic ring). The main difficulty to study such thin, self-assembled monolayers is their intrinsically very weak Raman scattering. However, when tip-enhanced Raman scattering (TERS) is used, in particular with the tip forming a junction with the metallic surface (a configuration often referred to as "gap-mode TERS") the Raman signal is enhanced by about 10^6 times. This technique therefore enabled me to detect molecularly thin layers of non-resonant molecules. Combined with the spatial resolution (≈ 10 nm) afforded by TERS, Raman maps with full spectroscopic information in each pixel could be recorded. These Raman images showed nanophase segregation with domain sizes from ≈ 30 nm to 240 nm. In contrast, imaging by scanning tunneling microscopy (STM) did not allow to discern the phase segregation through the molecular height difference and local electronic properties. Selected Raman peak ratios of the two molecules were evaluated to analyze their surface distribution. Different ratios of the mixing solution (10:1, 2:1 and 1:1) were also studied, and gave complementary insights into the segregation and domain sizes of the surface adsorbates.

Second, the optical coupling of two-dimensional flat surfaces, graphene and gold, was investigated. Graphene was identified with confocal Raman spectroscopy, reflection microscopy and scanning force microscopy (SFM). Both graphene and gold have been argued to provide Raman enhancement mainly through a chemical mechanism. Here Au(111) on mica was coated with copper phthalocyanine (CuPc) by vacuum evaporation. The homogeneity of CuPc on gold was verified by Raman spectroscopy. CuPc was chosen due to its planar structure and large π-conjugated electron system. By comparing the Raman peak at 1530 cm^{-1} (corresponding to the symmetric isoindole ring vibration mode), the enhancement of the flat gold surface with respect to mica was verified, and an enhancement of 4.5-fold was found. Single layer graphene was prepared by mechanical exfoliation, and deposited onto the gold surface coated with CuPc. Sandwiching CuPc between graphene and gold allows electrons to transfer in both directions and flat-lying CuPc promises good coupling of the system. The combined effect of graphene and gold showed strong Raman signals that were enhanced 68-fold, while graphene-enhanced Raman scattering (GERS) on mica only exhibited 7-fold enhancement. This system showed that the chemical enhancements from two individual enhancing materials can add to each other and the surface enhancements were vibrational-mode dependent. The GERS effect on gold showed a 15-fold enhancement, which implies that with this sandwiched structure, a nanoscale molecular junction is established. Also, this is the

first time that single layer graphene was identified with SFM by means of the quantitative imaging mode.

Lastly, given that Raman enhancement can be strengthened by employing two enhancing surfaces, TERS was applied on this sandwiched architecture in an attempt to increase the enhancement effect further, and obtain nanoscale spatial information. Chemical vapor deposition (CVD) grown graphene was transferred on top of an Au(111) surface modified with a self-assembled monolayer of OPE molecules. OPE was used as a sample molecule to monitor the optical response and the Raman enhancement. Confocal Raman spectroscopy showed that GERS on gold modified with OPE exhibited only a 2.5-fold enhancement, much less than the sandwiched CuPc. This reinforces that the GERS effect is highly sensitive to molecular details. OPE is a simple aromatic molecule and self-assembles with its long axis normal to the surfaces of gold and graphene. The combination of both its molecular similarity to graphene and its orientation relative to the graphene layer resulted in the lower Raman enhancement, but is explained by the molecular selectivity of GERS. Moreover, a further 10^4-fold enhancement of GERS on gold was supplied by the presence of a TERS tip. This indicated that the electromagnetic enhancement mechanism operates in a multiplicative fashion with chemical enhancement. This Raman enhancement strength is sufficient to observe very weakly scattering small molecules in graphene encapsulation applications. On the other hand, the area with molecules present but without graphene coverage, exhibits a 10^5-fold enhancement, as expected for gap-mode TERS. This indicates that graphene exhibits some shielding of the gap-mode TERS effect. The dependence on the tip-surface distance separation was evaluated, to make sure it was not simply a change in distance that caused the signal drop. The result showed that the signal intensity of bare OPE only dropped by 10 % at most when the separation of tip and surface changes by 0.34 nm, which equals the thickness of single layer graphene. Therefore, this rules out a distance effect dominantly affecting TERS signal strength.

This work provides fundamental understanding of optical coupling, and of chemical as well as electromagnetic enhancements. The roles of graphene in surface enhancement were carefully studied by experimental means. This might become useful for future design of graphene devices or biological applications. Owing to the inherent and unique features of graphene, such as being the thinnest yet the strongest material, outstanding electrical and heat conduction, whilst being transparent and impermeable to gases, graphene has found numerous applications in devices[189] and gas sensors.[66] The easy integration of graphene made

it feasible and flexible as a promising building block. Studies on organic electronic devices,[190, 191] such as organic light-emitting diodes, organic thin film transistors and organic photovoltaic cells,[192] have made a lot of efforts in understanding organic-metal interfaces,[193-195] intermolecular interactions,[196] and organic-organic heterojunctions,[197] etc. My study implies that graphene while serving as part of a device can also aid the detection of organic molecular layers in this molecular junction. Chemical information and molecular details, such as orientation on a surface,[194] intermolecular bonding, of which are important in improving a device performance can be obtained from this strongly enhanced Raman building architecture. Nondestructive mapping of these organic semiconducting thin films or defect detections in organic film growth can beconducted On the other hand, as gated graphene, doped graphene, and multilayered graphene showed some similar effects, the research in tailoring performance can be extended in the future and thus facilitate a broader wavelength spectrum for the use of graphene. Other two-dimensional materials (e.g. h-BN, MoS_2)[198] showing some surface enhancement can also be studied in parallel. Besides, graphene has also been used as a stiff and transparent substrate for imaging proteins at the single-molecule level by low-energy electrons.[199] My study indicates that graphene cannot only serve as a landing substrate for spectroscopy, but also acts as a good candidate for enhancing signals and in noninvasive imaging. The rise of graphene in imaging applications can pose the potential to replace the role of superlenses (or hyperlenses) in sub-diffraction scale imaging since graphene is much easier to produce.

In addition, combining the merits of TERS and GERS allows detection of molecules trapped under a graphene sheet, which are also protected from chemical degradation and physical wear caused by the tip.[174] The often seen carbonaceous contamination in TERS experiments could also be circumvented by covering analytes with graphene. This system is of particular interest for ultra-sensitive detection of small amounts of molecules. The immobilization of molecules by graphene provides a good platform for future detection at the single-molecule level since diffusion and reorientation of the molecules could thereby be avoided. Furthermore, graphene can also serve as an ultra-barrier membrane for isolation,[11] which allows one to dwell a thin water layer underneath,[178] and thereby to investigate biological questions and catalytic reactions proceeding in their natural environment. Compared to fluorescent microscopy, the label-free feature afforded inherently by Raman spectroscopy can help to study many fundamental biological behaviors, such as single

molecule dynamics. Study on this small amount of analytes is permitted by the high sensitivity of TERS as well as high light gathering and chemical inertness of graphene.

As a two-dimensional crystal, graphene can also be utilized as a standard material in TERS metrological applications. It is easy to prepare, highly reproducible, robust, and strong Raman scattering allows lab-to-lab comparison in the development of TERS instruments and tips. It is a transparent thin film, thus highly compatible with any of the existing TERS configurations. It has predefined and profound edge features, which allows one to evaluate the nanoscale resolution of TERS. It has a consistent optical response, which grants the evaluation of tip quality control.

Moreover, since graphene is a conductive and stable material, and can already be produced in sheets of large dimensions, employing graphene in STM-TERS measurements could help to establish a consistent tunneling feedback for the studies of non- or less-conductive materials. This extends a STM-TERS instrument's capability to study non-conductive materials. Some TERS artifacts or degradation of silver tips caused by unstable tunneling current can also thus be reduced or eliminated due to graphene conductivity. The uniform conductivity of graphene over a wide surface helps precise distance control between tip sample surfaces, which offers the opportunity for understanding the effect of quantum coupling in the nanometer regime. In other words, graphene can also be used as a nano-spacer to answer questions regarding quantum mechanical effects.

The strength of these investigated systems lies in a high degree of control over the surface, interfaces and tip-surface distance. A precisely controlled distance between tip and a metallic surface is desirable and holds promise for the generation of nanocavities. Meanwhile, this geometry might also provide opportunities for single molecule resolution of TERS at ambient conditions in the future.

References

1. E. Abbe, *Archiv für mikroskopische Anatomie*, 1873, **9**, 413-418.
2. Mischa Nicklaus, Tip-Enhanced Raman Spectroscopy for Nanoelectronics, 2014, Norderstedt, Germany
3. S. Schlücker, *Angew Chem Int Edit*, 2014, **53**, 4756-4795.
4. P.L. Stiles, J.A. Dieringer, N.C. Shah, and R.P. Van Duyne, *Annu. Rev. Anal. Chem.*, 2008, **1**, 601-626.
5. M. Fleischmann, P.J. Hendra, and A.J. Mcquillan, *Chem Phys Lett*, 1974, **26**, 163-166.
6. K.L. Kelly, E. Coronado, L.L. Zhao, and G.C. Schatz, *J Phys Chem B*, 2003, **107**, 668-677.
7. S.Y. Ding, J. Yi, J.F. Li, B. Ren, D.Y. Wu, R. Panneerselvam, and Z.Q. Tian, *Nat Rev Mater*, 2016, **1**. 16021.
8. E.C. Le Ru and P.G. Etchegoin, *Principles of Surface-Enhanced Raman Spectroscopy*. Ch. 4.8 The Chemical Enhancement, 2009. Oxford, UK, Elsevier. 258-261.
9. W.G. Xu, N.N. Mao, and J. Zhang, *Small*, 2013, **9**, 1206-1224.
10. R.R. Nair, P. Blake, A.N. Grigorenko, K.S. Novoselov, T.J. Booth, T. Stauber, N.M.R. Peres, and A.K. Geim, *Science*, 2008, **320**, 1308-1308.
11. P. Lange, M. Dorn, N. Severin, D.A. Vanden Bout, and J.P. Rabe, *J Phys Chem C*, 2011, **115**, 23057-23061.
12. N. Severin, M. Dorn, A. Kalachev, and J.P. Rabe, *Nano Lett*, 2011, **11**, 2436-2439.
13. K. Xiao, W. Deng, J.K. Keum, M. Yoon, I.V. Vlassiouk, K.W. Clark, A.P. Li, I.I. Kravchenko, G. Gu, E.A. Payzant, B.G. Sumpter, S.C. Smith, J.F. Browning, and D.B. Geohegan, *J Am Chem Soc*, 2013, **135**, 3680-3687.
14. X. Ling, J.X. Wu, W.G. Xu, and J. Zhang, *Small*, 2012, **8**, 1365-1372.
15. P. Li and T. Taubner, *Acs Nano*, 2012, **6**, 10107-10114.
16. P.N. Li, T. Wang, H. Bockmann, and T. Taubner, *Nano Lett*, 2014, **14**, 4400-4405.
17. X. Ling, L.G. Moura, M.A. Pimenta, and J. Zhang, *J Phys Chem C*, 2012, **116**, 25112-25118.
18. E.C. Le Ru, S.A. Meyer, C. Artur, P.G. Etchegoin, J. Grand, P. Lang, and F. Maurel, *Chem Commun*, 2011, **47**, 3903-3905.
19. J. Stadler, T. Schmid, and R. Zenobi, *Acs Nano*, 2011, **5**, 8442-8448.
20. R. Rickman and P. Dunstan, *J Raman Spectrosc*, 2014, **45**, 15-21.
21. F. Pashaee, F. Sharifi, G. Fanchini, and F. Lagugné-Labarthet, *Phys Chem Chem Phys*, 2015, **17**, 21315-21322.
22. S. Vantasin, I. Tanabe, Y. Tanaka, T. Itoh, T. Suzuki, Y. Kutsuma, K. Ashida, T. Kaneko, and Y. Ozaki, *J Physl Chem C*, 2014, **118**, 25809-25815.
23. T. Suzuki, T. Itoh, S. Vantasin, S. Minami, Y. Kutsuma, K. Ashida, T.-a. Kaneko, Y. Morisawa, T. Miura, and Y. Ozaki, *Phys Chem Chem Phys*, 2014, **16**, 20236-20240.
24. W.Q. Zhu, R. Esteban, A.G. Borisov, J.J. Baumberg, P. Nordlander, H.J. Lezec, J. Aizpurua, and K.B. Crozier, *Nat Commun*, 2016, **7**. 11495.
25. K.J. Savage, M.M. Hawkeye, R. Esteban, A.G. Borisov, J. Aizpurua, and J.J. Baumberg, *Nature*, 2012, **491**, 574-577.
26. R. Zhang, Y. Zhang, Z. Dong, S. Jiang, C. Zhang, L. Chen, L. Zhang, Y. Liao, J. Aizpurua, and Y.e. Luo, *Nature*, 2013, **498**, 82-86.
27. F. Benz, M.K. Schmidt, A. Dreismann, R. Chikkaraddy, Y. Zhang, A. Demetriadou, C. Carnegie, H. Ohadi, B. de Nijs, and R. Esteban, *Science*, 2016, **354**, 726-729.
28. C.V. Raman and K.S. Krishnan, *Curr Sci India*, 1998, **74**, 381-381.
29. P. Larkin, *Infrared and Raman Spectroscopy*, 2011. Waltham, MA, Elsevier.
30. B.C. Ferraro JR, *Introductory Raman Spectroscopy*, 2002. Waltham, MA, Elsevier.

31. D.G. Smith E, *Modern Raman Spectroscopy: A Practical Approach.*, 2005. Chichester, UK, Wiley.
32. T.W. Collette and T.L. Williams, *J Environ Monitor*, 2002, **4**, 27-34.
33. B.B. Johnson and W.L. Peticolas, *Annu Rev Phys Chem*, 1976, **27**, 465-491.
34. L. Opilik, T. Schmid, and R. Zenobi, *Annu Rev Anal Chem*, 2013, **6**, 379-398.
35. http://forum.sci.ccny.cuny.edu/core_facilities/microscopy-imaging/raman-confocal/Confocal-raman-note.pdf
36. D.L. Jeanmaire and R.P. Van Duyne, *Journal of Electroanalytical Chemistry and Interfacial Electrochemistry*, 1977, **84**, 1-20.
37. M. Moskovits, *J Chem Phys*, 1978, **69**, 4159-4161.
38. J.A. Creighton, C.G. Blatchford, and M.G. Albrecht, *Journal of the Chemical Society, Faraday Transactions 2: Molecular and Chemical Physics*, 1979, **75**, 790-798.
39. S.M. Nie and S.R. Emery, *Science*, 1997, **275**, 1102-1106.
40. K. Kneipp, Y. Wang, H. Kneipp, L.T. Perelman, I. Itzkan, R. Dasari, and M.S. Feld, *Phys Rev Lett*, 1997, **78**, 1667-1670.
41. P.L. Stiles, J.A. Dieringer, N.C. Shah, and R.R. Van Duyne, *Annual Review of Analytical Chemistry*, 2008, **1**, 601-626.
42. M. Moskovits, *J Raman Spectrosc*, 2005, **36**, 485-496.
43. A. Ricardo, *Surface-Enhanced Vibrational Spectroscopy*, 2006. Chichester, UK, Wiley.
44. B. Carolin, *Tip-Enhanced Raman Spectroscopy–Metrology and Applications to Biomolecules*, 2014, ETH Zürich, Ph.D. dissertation.
45. A.K. Geim and K.S. Novoselov, *Nat Mater*, 2007, **6**, 183-191.
46. H.A. Mouras S, Djurado D,Cousseins J.-C, *Revue de chimie minérale*, 1987, **24**, 572.
47. K.S. Novoselov, A.K. Geim, S.V. Morozov, D. Jiang, Y. Zhang, S.V. Dubonos, I.V. Grigorieva, and A.A. Firsov, *Science*, 2004, **306**, 666-669.
48. K.S. Novoselov, *Angew Chem Int Edit*, 2011, **50**, 6986-7002.
49. K.S. Novoselov, *Rev Mod Phys*, 2011, **83**, 837-849.
50. P. May, *Electronic and vibrational properties of low-dimensional carbon systems*, 2012, Technischen Universit¨at Berlin, Ph.D. dissertation. p. 7.
51. P.R. Wallace, *Phys Rev*, 1947, **71**, 622-634.
52. J.F. Liu, A.R. Wright, C. Zhang, and Z.S. Ma, *Appl Phys Lett*, 2008, **93**, 041106.
53. P. Alonso-González, A.Y. Nikitin, F. Golmar, A. Centeno, A. Pesquera, S. Vélez, J. Chen, G. Navickaite, F. Koppens, A. Zurutuza, F. Casanova, L.E. Hueso, and R. Hillenbrand, *Science*, 2014. 1369-1373
54. http://www.nanogune.eu/newsroom/science-flatland-optics-graphene
55. C.-J. Shih, *Understanding and Engineering Molecular Interactions and Electronic Transport at 2D Materials Interfaces*, 2014, Massachusetts Institute Of Technology, Ph.D. dissertation. p. 32.
56. M. Dorn, P. Lange, A. Chekushin, N. Severin, and J.P. Rabe, *J Appl Phys*, 2010, **108**, 106101.
57. B. Rezania, M. Dorn, N. Severin, and J.P. Rabe, *J Colloid Interf Sci*, 2013, **407**, 500-504.
58. K.S. Novoselov, D. Jiang, F. Schedin, T.J. Booth, V.V. Khotkevich, S.V. Morozov, and A.K. Geim, *P Natl Acad Sci USA*, 2005, **102**, 10451-10453.
59. X.S. Li, W.W. Cai, J.H. An, S. Kim, J. Nah, D.X. Yang, R. Piner, A. Velamakanni, I. Jung, E. Tutuc, S.K. Banerjee, L. Colombo, and R.S. Ruoff, *Science*, 2009, **324**, 1312-1314.
60. T.F. Chung, T. Shen, H.L. Cao, L.A. Jauregui, W. Wu, Q.K. Yu, D. Newell, and Y.P. Chen, *Int J Mod Phys B*, 2013, **27**. 1341002.
61. A. Reina, X.T. Jia, J. Ho, D. Nezich, H.B. Son, V. Bulovic, M.S. Dresselhaus, and J. Kong, *Nano Lett*, 2009, **9**, 30-35.
62. http://www.science.oregonstate.edu/~minote/wiki/doku.php?id=start

63. Y. Hernandez, V. Nicolosi, M. Lotya, F.M. Blighe, Z. Sun, S. De, I. McGovern, B. Holland, M. Byrne, and Y.K. Gun'Ko, *Nat Nanotechnol*, 2008, **3**, 563-568.
64. V. Nicolosi, M. Chhowalla, M.G. Kanatzidis, M.S. Strano, and J.N. Coleman, *Science*, 2013, **340**, 1226419.
65. S. Park and R.S. Ruoff, *Nat Nanotech*, 2009, **4**, 217-224.
66. Y. Zhu, S. Murali, W. Cai, X. Li, J.W. Suk, J.R. Potts, and R.S. Ruoff, *Adv Mater*, 2010, **22**, 3906-3924.
67. A.C. Ferrari, J.C. Meyer, V. Scardaci, C. Casiraghi, M. Lazzeri, F. Mauri, S. Piscanec, D. Jiang, K.S. Novoselov, S. Roth, and A.K. Geim, *Phys Rev Lett*, 2006, **97**, 187401.
68. A.C. Ferrari and D.M. Basko, *Nat Nanotech*, 2013, **8**, 235-246.
69. M.S. Dresselhaus, A. Jorio, and R. Saito, *Annu Rev Conden Ma P*, 2010, **1**, 89-108.
70. A.C. Ferrari, *Solid State Commun*, 2007, **143**, 47-57.
71. C. Casiraghi, S. Pisana, K.S. Novoselov, A.K. Geim, and A.C. Ferrari, *Appl Phys Lett*, 2007, **91**, 233108.
72. A. Das, S. Pisana, B. Chakraborty, S. Piscanec, S.K. Saha, U.V. Waghmare, K.S. Novoselov, H.R. Krishnamurthy, A.K. Geim, A.C. Ferrari, and A.K. Sood, *Nat Nanotech*, 2008, **3**, 210-215.
73. S. Pisana, M. Lazzeri, C. Casiraghi, K.S. Novoselov, A.K. Geim, A.C. Ferrari, and F. Mauri, *Nat Mater*, 2007, **6**, 198-201.
74. L. Xie, X. Ling, Y. Fang, J. Zhang, and Z. Liu, *J Am Chem Soc*, 2009, **131**, 9890-9891.
75. X. Ling, L.M. Xie, Y. Fang, H. Xu, H.L. Zhang, J. Kong, M.S. Dresselhaus, J. Zhang, and Z.F. Liu, *Nano Lett*, 2010, **10**, 553-561.
76. W. Xu, N. Mao, and J. Zhang, *Small*, 2013, **9**, 1206-1224.
77. X. Ling and J. Zhang, *Small*, 2010, **6**, 2020-2025.
78. H. Xu, L.M. Xie, H.L. Zhang, and J. Zhang, *ACS Nano*, 2011, **5**, 5338-5344.
79. S.X. Huang, X. Ling, L.B. Liang, Y. Song, W.J. Fang, J. Zhang, J. Kong, V. Meunier, and M.S. Dresselhaus, *Nano Lett*, 2015, **15**, 2892-2901.
80. L. Rayleigh, *Philos. Mag.*, 1879, **8**, 261.
81. E.H. Synge, *Philos Mag*, 1928, **6**, 356-362.
82. https://en.wikipedia.org/wiki/Near-field_scanning_optical_microscope
83. M.S. Anderson, *Appl Phys Lett*, 2000, **76**, 3130-3132.
84. N. Hayazawa, Y. Inouye, Z. Sekkat, and S. Kawata, *Opt Commun*, 2000, **183**, 333-336.
85. B. Pettinger, G. Picardi, R. Schuster, and G. Ertl, *Electrochemistry*, 2000, **68**, 942-949.
86. R.M. Stöckle, Y.D. Suh, V. Deckert, and R. Zenobi, *Chem Phys Lett*, 2000, **318**, 131-136.
87. J. Stadler, T. Schmid, and R. Zenobi, *Nanoscale*, 2012, **4**, 1856-1870.
88. J. Stadler, T. Schmid, and R. Zenobi, *Nano Lett*, 2010, **10**, 4514-4520.
89. J. Steidtner and B. Pettinger, *Phys Rev Lett*, 2008, **100**, 236101
90. N. Anderson, A. Hartschuh, S. Cronin, and L. Novotny, *J Am Chem Soc*, 2005, **127**, 2533-2537.
91. J. Steidtner and B. Pettinger, *Phys Rev Lett*, 2008, **100**, 236101.
92. M.D. Sonntag, J.M. Klingsporn, L.K. Garibay, J.M. Roberts, J.A. Dieringer, T. Seideman, K.A. Scheidt, L. Jensen, G.C. Schatz, and R.P. Van Duyne, *J Phys Chem C*, 2011, **116**, 478-483.
93. W. Zhang, B.S. Yeo, T. Schmid, and R. Zenobi, *J Phys Chem C*, 2007, **111**, 1733-1738.
94. C. Chen, N. Hayazawa, and S. Kawata, *Nat Commun*, 2014, **5**, 3312.
95. M. Liao, S. Jiang, C. Hu, R. Zhang, Y. Kuang, J. Zhu, Y. Zhang, and Z. Dong, *Nano Lett*, 2016, **16**, 4040-4046.
96. L.T. Nieman, G.M. Krampert, and R.E. Martinez, *Review of Scientific Instruments*, 2001, **72**, 1691-1699.
97. L. Opilik, Ü. Dogan, J. Szczerbiński, and R. Zenobi, *Appl Phys Lett*, 2015, **107**, 091109.
98. L. Opilik, Ü. Dogan, C.-Y. Li, B. Stephanidis, J.-F. Li, and R. Zenobi, *The Journal of Physical Chemistry C*, 2016, **120**, 20828-20832.
99. X. Cui, D. Erni, W. Zhang, and R. Zenobi, *Chem Phys Lett*, 2008, **453**, 262-265.

100. L. Opilik, *Tip-Enhanced Raman Spectroscopic Imaging of Molecular Monolayers*, 2015, ETH Zürich.
101. G.M. Whitesides, J.K. Kriebel, and J.C. Love, *Science progress*, 2005, **88**, 17-48.
102. J.C. Love, L.A. Estroff, J.K. Kriebel, R.G. Nuzzo, and G.M. Whitesides, *Chemical reviews*, 2005, **105**, 1103-1170.
103. M.M. Thuo, W.F. Reus, C.A. Nijhuis, J.R. Barber, C. Kim, M.D. Schulz, and G.M. Whitesides, *J Am Chem Soc*, 2011, **133**, 2962-2975.
104. A. Stewart, S. Zheng, M.R. McCourt, and S.E. Bell, *ACS Nano*, 2012, **6**, 3718-3726.
105. K.-Y. Wu, S.-Y. Yu, and Y.-T. Tao, *Langmuir*, 2009, **25**, 6232-6238.
106. J. Kim, Y.S. Rim, Y. Liu, A.C. Serino, J.C. Thomas, H. Chen, Y. Yang, and P.S. Weiss, *Nano Lett*, 2014, **14**, 2946-2951.
107. A. Hung, S. Mwenifumbo, M. Mager, J.J. Kuna, F. Stellacci, I. Yarovsky, and M.M. Stevens, *J Am Chem Soc*, 2011, **133**, 1438-1450.
108. D. Hobara, S.-i. Imabayashi, and T. Kakiuchi, *Nano Lett*, 2002, **2**, 1021-1025.
109. R.K. Smith, S.M. Reed, P.A. Lewis, J.D. Monnell, R.S. Clegg, K.F. Kelly, L.A. Bumm, J.E. Hutchison, and P.S. Weiss, *J Phys Chem B*, 2001, **105**, 1119-1122.
110. Y. Qi, X. Liu, B. Hendriksen, V. Navarro, J.Y. Park, I. Ratera, J. Klopp, C. Edder, F.J. Himpsel, and J. Frechet, *Langmuir*, 2010, **26**, 16522-16528.
111. S. Stranick, S. Atre, A.N. Parikh, M. Wood, D. Allara, N. Winograd, and P. Weiss, *Nanotechnology*, 1996, **7**, 438.
112. W.A. Hayes, H. Kim, X. Yue, S.S. Perry, and C. Shannon, *Langmuir*, 1997, **13**, 2511-2518.
113. G.E. Poirier, *Chemical reviews*, 1997, **97**, 1117-1128.
114. A.H. Schäfer, C. Seidel, L. Chi, and H. Fuchs, *Adv. Mater*, 1998, **10**, 839
115. J. Stadler, T. Schmid, L. Opilik, P. Kuhn, P.S. Dittrich, and R. Zenobi, *Beilstein journal of nanotechnology*, 2011, **2**, 509-515.
116. D. Wang, F. Tian, and J. Lu, *J Vac Sci Technol B*, 2002, **20**, 60-64.
117. S. Mannsfeld, T. Canzler, T. Fritz, H. Proehl, K. Leo, S. Stumpf, G. Goretzki, and K. Gloe, *The J Phys Chem B*, 2002, **106**, 2255-2260.
118. M.L. Donten, A. Królikowska, and J. Bukowska, *Phys Chem Chem Phys*, 2009, **11**, 3390-3400.
119. A. Centrone, Y. Hu, A.M. Jackson, G. Zerbi, and F. Stellacci, *Small*, 2007, **3**, 814-817.
120. C. Gentilini, P. Franchi, E. Mileo, S. Polizzi, M. Lucarini, and L. Pasquato, *Angew Chem Intl Ed*, 2009, **48**, 3060-3064.
121. C.D. Bain and G.M. Whitesides, *Science*, 1988, **240**, 62-63.
122. K.M. Harkness, A. Balinski, J.A. McLean, and D.E. Cliffel, *Angew Chem Intl Ed*, 2011, **50**, 10554-10559.
123. E. Lipiec, R. Sekine, J. Bielecki, W.M. Kwiatek, and B.R. Wood, *Angew Chem Intl Ed*, 2014, **53**, 169-172.
124. S. Najjar, D. Talaga, L.o. Schué, Y. Coffinier, S. Szunerits, R. Boukherroub, L. Servant, V. Rodriguez, and S.b. Bonhommeau, *J Phys Chem C*, 2014, **118**, 1174-1181.
125. N. Hayazawa, Y. Inouye, Z. Sekkat, and S. Kawata, *Opt Commun*, 2000, **183**, 333-336.
126. Z. Liu, X. Wang, K. Dai, S. Jin, Z.-C. Zeng, M.-D. Zhuang, Z.-L. Yang, D.-Y. Wu, B. Ren, and Z.Q. Tian, *J Raman Spectrosc*, 2009, **40**, 1400-1406.
127. Z. Zheng, L. Opilik, F. Schiffmann, W. Liu, G. Bergamini, P. Ceroni, L.-T. Lee, A. Schütz, J. Sakamoto, and R. Zenobi, *J Am Chem Soc*, 2014, **136**, 6103-6110.
128. G. Picardi, M. Chaigneau, R. Ossikovski, C. Licitra, and G. Delapierre, *J Raman Spectrosc*, 2009, **40**, 1407-1412.
129. G. Picardi, A. Krolikowska, R. Yasukuni, M. Chaigneau, M. Escude, V. Mourier, C. Licitra, and R. Ossikovski, *Chemphyschem*, 2014, **15**, 276-282.
130. N.N. Horimoto, S. Tomizawa, Y. Fujita, S. Kajimoto, and H. Fukumura, *Chem Commun*, 2014, **50**, 9862-9864.

131. H. Munakata, S. Kuwabata, Y. Ohko, and H. Yoneyama, *J Electroanal Chem*, 2001, **496**, 29-36.
132. S. Stranick, A.N. Parikh, Y.-T. Tao, D. Allara, and P. Weiss, *The Journal of Physical Chemistry*, 1994, **98**, 7636-7646.
133. J.-j. Yu, Y.H. Tan, X. Li, P.-K. Kuo, and G.-y. Liu, *J Am Chem Soc*, 2006, **128**, 11574-11581.
134. http://gwyddion.net/
135. K. Edinger, A. Gölzhäuser, K. Demota, C. Wöll, and M. Grunze, *Langmuir*, 1993, **9**, 4-8.
136. Z. Chernia, T. Livneh, I. Pri-Bar, and J. Koresh, *Vibrational Spectroscopy*, 2001, **25**, 119-131.
137. S.W. Joo and K. Kim, *J Raman Spectrosc*, 2004, **35**, 549-554.
138. M. Chaigneau, G. Picardi, and R. Ossikovski, *International journal of molecular sciences*, 2011, **12**, 1245-1258.
139. L. Opilik, T. Bauer, T. Schmid, J. Stadler, and R. Zenobi, *Physical Chemistry Chemical Physics*, 2011, **13**, 9978-9981.
140. A. Kudelski, *J Phys Chem B*, 2010, **114**, 5180-5189.
141. X.M. Qian and S.M. Nie, *Chem Soc Rev*, 2008, **37**, 912-920.
142. W.E. Doering and S.M. Nie, *J Phys Chem B*, 2002, **106**, 311-317.
143. C.S. Huang, M. Kim, B.M. Wong, N.S. Safron, M.S. Arnold, and P. Gopalan, *J Phys Chem C*, 2014, **118**, 2077-2084.
144. X. Ling, J.X. Wu, L.M. Xie, and J. Zhang, *J Phys Chem C*, 2013, **117**, 2369-2376.
145. N. Jung, A.C. Crowther, N. Kim, P. Kim, and L. Brus, *ACS Nano*, 2010, **4**, 7005-7013.
146. W.G. Xu, X. Ling, J.Q. Xiao, M.S. Dresselhaus, J. Kong, H.X. Xu, Z.F. Liu, and J. Zhang, *P Natl Acad Sci USA*, 2012, **109**, 9281-9286.
147. T. Uemura, M. Furumoto, T. Nakano, M. Akai-Kasaya, A. Salto, M. Aono, and Y. Kuwahara, *Chem Phys Lett*, 2007, **448**, 232-236.
148. X. Lu, K.W. Hipps, X.D. Wang, and U. Mazur, *J Am Chem Soc*, 1996, **118**, 7197-7202.
149. I. Chizhov, G. Scoles, and A. Kahn, *Langmuir*, 2000, **16**, 4358-4361.
150. C.J. Shih, R. Pfattner, Y.C. Chiu, N. Liu, T. Lei, D.S. Kong, Y. Kim, H.H. Chou, W.G. Bae, and Z.N. Bao, *Nano Lett*, 2015, **15**, 7587-7595.
151. J. Niederhausen, P. Amsalem, A. Wilke, R. Schlesinger, S. Winkler, A. Vollmer, J. P. Rabe, and N. Koch, *Phys Rev B*, 2012, **86**, 081411.
152. D.G. de Oteyza, A. El-Sayed, J.M. Garcia-Lastra, E. Goiri, T.N. Krauss, A. Turak, E. Barrena, H. Dosch, J. Zegenhagen, A. Rubio, Y. Wakayama, and J.E. Ortega, *J Chem Phys*, 2010, **133**, 214703
153. H.-J. Butt and M. Jaschke, *Nanotechnology*, 1995, **6**, 1.
154. E.C. Le Ru, E. Blackie, M. Meyer, and P.G. Etchegoin, *J Phys Chem C*, 2007, **111**, 13794-13803.
155. Y.F. Dufrene, D. Martinez-Martin, I. Medalsy, D. Alsteens, and D.J. Muller, *Nat Methods*, 2013, **10**, 847-854.
156. J.R. Pratt, G.A. Shaw, L. Kumanchik, and N.A. Burnham, *J Appl Phys*, 2010, **107,** 044305
157. B.W. Caplins, T.K. Mullenbach, R.J. Holmes, and D.A. Blank, *Phys Chem Chem Phys*, 2016, **18**, 11454-11459.
158. Z.H. Ni, T. Yu, Z.Q. Luo, Y.Y. Wang, L. Liu, C.P. Wong, J.M. Miao, W. Huang, and Z.X. Shen, *ACS Nano*, 2009, **3**, 569-574.
159. S. Berciaud, S. Ryu, L.E. Brus, and T.F. Heinz, *Nano Lett*, 2009, **9**, 346-352.
160. E.H. Hwang, S. Adam, and S. Das Sarma, *Phys Rev Lett*, 2007, **98**, 186806
161. J. Martin, N. Akerman, G. Ulbricht, T. Lohmann, J.H. Smet, K. von Klitzing, and A. Yacoby, *Nat Phys*, 2008, **4**, 144-148.
162. C. Neumann, S. Reichardt, P. Venezuela, M. Drogeler, L. Banszerus, M. Schmitz, K. Watanabe, T. Taniguchi, F. Mauri, B. Beschoten, S.V. Rotkin, and C. Stampfer, *Nat Commun*, 2015, **6**, 8429
163. J.R. Lombardi, R.L. Birke, T.H. Lu, and J. Xu, *J Chem Phys*, 1986, **84**, 4174-4180.
164. B. Knoll and F. Keilmann, *Nature*, 1999, **399**, 134-137.

165. B. Pettinger, P. Schambach, C.J. Villagómez, and N. Scott, *Annu Rev Phys Chem*, 2012, **63**, 379-399.
166. Y. Saito, P. Verma, K. Masui, Y. Inouye, and S. Kawata, *J Raman Spectrosc*, 2009, **40**, 1434-1440.
167. T.-a. Yano, P. Verma, Y. Saito, T. Ichimura, and S. Kawata, *Nature Photonics*, 2009, **3**, 473-477.
168. P. Lange, G. Kewes, N. Severin, O. Benson, and J.P. Rabe, *arXiv preprint arXiv:1404.6518*, 2014.
169. A. Grigorenko, M. Polini, and K. Novoselov, *Nature Photonics*, 2012, **6**, 749-758.
170. P. Li, T. Wang, H. Böckmann, and T. Taubner, *Nano Lett*, 2014, **14**, 4400-4405.
171. H. Yan, X. Li, B. Chandra, G. Tulevski, Y. Wu, M. Freitag, W. Zhu, P. Avouris, and F. Xia, *Nat Nanotechnol*, 2012, **7**, 330-334.
172. O. Khatib, J.D. Wood, A.S. McLeod, M.D. Goldflam, M. Wagner, G.L. Damhorst, J.C. Koepke, G.P. Doidge, A. Rangarajan, and R. Bashir, *ACS Nano*, 2015, **9**, 7968-7975.
173. X. Ling, S. Huang, S. Deng, N. Mao, J. Kong, M.S. Dresselhaus, and J. Zhang, *Accounts Chem Res*, 2015, **48**, 1862-1870.
174. A. Kalachev, J.P. Rabe, and N. Severin, *Method for analyzing a substance*, 2013, US Patent.
175. C. Vericat, M. Vela, and R. Salvarezza, *Phys Chem Chem Phys*, 2005, **7**, 3258-3268.
176. H. Sellers, A. Ulman, Y. Shnidman, and J.E. Eilers, *J Am Chem Soc*, 1993, **115**, 9389-9401.
177. M.D. Lay, K. Varazo, and J.L. Stickney, *Langmuir*, 2003, **19**, 8416-8427.
178. N. Severin, P. Lange, I.M. Sokolov, and J.P. Rabe, *Nano Lett*, 2012, **12**, 774-779.
179. Y. Moon, J. Shin, S. Seo, J. Park, S. Dugasani, S. Woo, T. Park, S. Park, and J. Ahn, *Appl Phys Lett*, 2014, **104**, 231904.
180. A. Matković, B. Vasić, J. Pešić, J. Prinz, I. Bald, A.R. Milosavljević, and R. Gajić, *New J Phys*, 2016, **18**, 025016.
181. W. Zhang, Cui, B.-S. Yeo, T. Schmid, C. Hafner, and R. Zenobi, *Nano Lett*, 2007, **7**, 1401-1405.
182. E. Lipiec, R. Sekine, J. Bielecki, W.M. Kwiatek, and B.R. Wood, *Angew Chem Int Edit*, 2014, **53**, 169-172.
183. S. Najjar, D. Talaga, L. Schue, Y. Coffinier, S. Szunerits, R. Boukherroub, L. Servant, V. Rodriguez, and S. Bonhommeau, *J Phys Chem C*, 2014, **118**, 1174-1181.
184. P. Nordlander, C. Oubre, E. Prodan, K. Li, and M. Stockman, *Nano Lett*, 2004, **4**, 899-903.
185. S. Hayashi, *Spectroscopy of Gap Modes in Metal Particle—Surface Systems*, in *Near-field optics and surface plasmon polaritons,* 2001, Springer. p. 71-95.
186. C. Toccafondi, G. Picardi, and R. Ossikovski, *J Phys Chem C*, 2016, **120**, 18209-18219.
187. Z.X. Sun, S.K. Hamalainen, J. Sainio, J. Lahtinen, D. Vanmaekelbergh, and P. Liljeroth, *Phys Rev B*, 2011, **83**, 081415
188. J. Mertens, A.L. Eiden, D.O. Sigle, F. Huang, A. Lombardo, Z. Sun, R.S. Sundaram, A. Colli, C. Tserkezis, and J. Aizpurua, *Nano Lett*, 2013, **13**, 5033-5038.
189. S. Pang, Y. Hernandez, X. Feng, and K. Müllen, *Adv Mater*, 2011, **23**, 2779-2795.
190. R.H. Friend, R.W. Gymer, A.B. Holmes, J.H. Burroughes, R.N. Marks, C. Taliani, D.D.C. Bradley, D.A.D. Santos, J.L. Bredas, M. Logdlund, and W.R. Salaneck, *Nature*, 1999, **397**, 121-128.
191. B. Mazhari, *Org Electron*, 2005, **6**, 229-236.
192. F. Zhang, A. Vollmer, J. Zhang, Z. Xu, J.P. Rabe, and N. Koch, *Org Electron*, 2007, **8**, 606-614.
193. H. Ishii, K. Sugiyama, E. Ito, and K. Seki, *Adv Mater*, 1999, **11**, 605-625.
194. S. Duhm, G. Heimel, I. Salzmann, H. Glowatzki, R.L. Johnson, A. Vollmer, J.P. Rabe, and N. Koch, *Nat Mater*, 2008, **7**, 326-332.
195. A. Kahn, N. Koch, and W. Gao, *J. Polym. Sci., Part B: Polym. Phys.*, 2003, **41**, 2529-2548.
196. F. Cacialli, J.S. Wilson, J.J. Michels, C. Daniel, C. Silva, R.H. Friend, N. Severin, P. Samorì, J.P. Rabe, and M.J. O'Connell, *Nat Mater*, 2002, **1**, 160-164.

197. S. Duhm, I. Salzmann, G. Heimel, M. Oehzelt, A. Haase, R.L. Johnson, J.P. Rabe, and N. Koch, *Appl Phys Lett*, 2009, **94**, 19.
198. X. Ling, W.J. Fang, Y.H. Lee, P.T. Araujo, X. Zhang, J.F. Rodriguez-Nieva, Y.X. Lin, J. Zhang, J. Kong, and M.S. Dresselhaus, *Nano Lett*, 2014, **14**, 3033-3040.
199. J.-N. Longchamp, S. Rauschenbach, S. Abb, C. Escher, T. Latychevskaia, K. Kern, and H.-W. Fink, *P Natl Acad Sci*, 2017, **114**, 1474-1479.

Abbreviation

AFM	atomic force microscopy
CCD	charge-coupled device
CM	chemical enhancement
CT	charge transfer
CuPc	Cu-phthalocyanine
CVD	chemical vapor deposition
CV	crystal violet
EF	enhancement factor
E_F	Fermi level
EM	electromagnetic field mechanism
EMCCD	electron-multiplying charge-coupled device
FET	field-effect transistor
FWHM	full width at half maximum
GERS	graphene-enhanced Raman scattering
HOMO	highest occupied molecular orbital
HOPG	highly oriented pyrolytic graphite
IR	infrared
ITO	indium tin oxide
KPFM	kelvin probe force microscopy
LA	longitudinal acoustic
LB	Langmuir-Blodgett
LUMO	lowest unoccupied molecular orbital
NA	numerical aperture
OPE	thioacetic acid S-[4-[4-(phenylethynyl)-phenyl]ethynyl]benzene-thiol ester
PhS	thiolphenol
PMMA	poly(methyl methacrylate)
PMT	photomultiplier tube
PPP	protoporphyrin IX
R6G	rhodamine 6G
SAM	self-assembled monolayer
SEM	scanning electron microscopy
SERS	surface-enhanced Raman spectroscopy
SFM	scanning force microscopy
SFM-QI	scanning force microscope in quantitative imaging mode
SLG	single layer graphene
SNOM	scanning near-field optical microscopy
SPM	scanning probe microscopy
STM	scanning tunneling microscopy
TEM	transmission electron microscopy
TERS	tip-enhanced Raman spectroscopy
TO	transverse optical
UV	ultraviolet

Acknowledgement

This thesis would not have been finished that smoothly without many people's favors. I am grateful to many people who have accompanied me and significantly helped me in each step, leading to the successful completion of this thesis.

First of all, I would like to deeply thank Prof. Dr. Jürgen P. Rabe and Prof. Dr. Renato Zenobi, who gave me this unique opportunity to carry out doctoral studies under their guidance, scientific advice, as well as for career and life mentoring. Ich danke Ihnen, dass Sie immer für mich da waren.

I thank SALSA for the funding through DFG and their support in thisdoctoral study.

Committee members

I would like to thank Prof. Dr. Kallol Ray who chaired the committee and Dr. Gudrun Scholz who participated as a committee member. I particularly thank Prof. Dr. Janina Kneipp, who kindly agreed to be a reviewer and took the time to write a report of my thesis. I have known Prof. Kneipp since the first day of my doctoral study due to the SALSA graduate school. She is always very kind and supportive in helping students, including me. I specially thank Prof. Zenobi who reviewed my thesis and spent one day in traveling to Berlin for joining the defense. Prof. Rabe is deeply acknowledged for my thesis corrections and writing a report on it from Boston, as well as defense preparations.

Zürich

I gratefully thank Prof. Zenobi for teaching me Tip-enhanced Raman Spectroscopy, sharing his profound experiences and information in this specific field, offering thoughtful guidance and support all the time and for all the efforts and time he invested in my professional and personal education. Besides, I thank him also for his open talks and always tolerating my thoughtless/inattentive mistakes. I am truly impressed and appreciate all the things you have shown me from the high scope these past years. I thank Dr. Lothar Opilik for always being very thoughtful and attentive in scientific discussions, as well as instrument development and maintenance. You demonstrated a great and unbeatable example as a

senior member. I thank Dr. Carolin Blum who was super generous for giving me a printed thesis as a present. This thesis has accompanied many of my TERS education periods and therefore traveled with me to Germany, Japan, and Taiwan. I thank Prof. Jian-Feng Li who has been so kind and friendly in sharing his very successful experiences in research and offering concise suggestions. Jacek and Feng are sincerely thanked for numerous amount of significant helps in science as well as acting as important friends and colleagues. Guido is thanked for warm, sincere and firm friendship through many matey, in-depth conversations across all topics. Robert is thanked for more than just strong technical supports. Stephan, Simon, Jasmin, Amy, Agni and Jan for your help and friendship. I significantly thank Prof. Chih-Jen Shih for showing how to transfer graphene, lecturing me several times in graphene properties, and also for sharing career experiences. I thank Dr. Loau Pi deeply and significantly for sharing Ph.D. studying experiences- whenever I had difficulties, you were always encouraging me. You were a good-listener and demonstrated a great model in this lonely study-abroad journey by your diligence, kindness, as well as good analysis in life, culture and career. Heinz Benz is thanked for the strong electronic support and manufacturing etching-device. Brigitte is thanked for many important administrative steps. I particularly thank Florian for the help in graphics.

Berlin

I express my greatest gratitude to Prof. Jürgen P. Rabe in my Ph.D. education, as a Doktorvater. He offered me these fancy and fantastic projects, as well as a powerful and brand-new instrument to drive with! Prof. Rabe was always there for me, acting justified for any issues and in the course of discussions, showing extremely precise accuracy at work. Prof. Rabe has directed me significantly with useful discussion, encouraged me when I was lost and offering thoughts contributing to the finest version of this work.

I thank Dr. Nikolai Severin and Dr. Stefan Kirstein for always being there to provide scientific advices and technical support in instrumentation, and Manuel, Valentin, Egon, Jose and Caroline for sharing their experiences and friendship. Fardin is extremely acknowledged for the significant company (in Adlershof) and firm friendship, as well as all sorts of discussions

and advices. I thank Bita, Hu, Rauf and Katie for being friendly. I also thank Dr. Marc Chaigneau for providing complete instrument training and Mr. Michael Beier for the instrument support. I thank Mr. Scholz for fixing the instrument once in an urgent situation. I thank Paul Beyer for being a responsible collaborator in publishing.

I thank Aidan Rafferty for his genuine and cute friendship through many supports and encouragement, particularly for proofreading my thesis and manuscript to publish. Without your generous and kind favors, this thesis and paper would stuck somewhere.

I would like to thank Anna Au for her firm and supportive flatmate friendship! You have accompanied me going through many hard times and we had great time in Berlin together. You have shown unforgettable friendship to my life through acting as a good-listener and advices-giver, and also shown me an indulgence and love for Berlin, as well as many details of (funky) living ways.

I also thank Prof. Dr. Chung-Yen Mou at National Taiwan University for inspiring my research by his intense enthusiasm and for always being a good mentor to me, as well as his supports.

Finally, I thank my mother, my sister, and my family for always loving me, and supporting me.

List of Publications

-Publications comprising parts of this work

- W. -I. Lin, F. Gholami, R. Zenobi, J. P. Rabe. Graphene-enhanced Near-Field Raman Scattering, in preparation
- W. -I. Lin, F. Gholami, P. Beyer, N. Severin, F. Shao, R. Zenobi, J. P. Rabe. Strongly enhanced Raman scattering of Cu-phthalocyanine sandwiched between graphene and Au(111), *Chem. Commun.*, **2017**, *53*, 724-727
- W. -I. Lin, F. Shao, B. Stephanidis, R. Zenobi. Tip-enhanced Raman spectroscopic imaging shows segregation within binary self-assembled thiol monolayers at ambient conditions, *Anal Bioanal Chem*, **2015**, *407,* 8197-8204

-Publications in addition to this work

- W. Cheng, F. Rechberger, G. Ilari, H. Ma, W.-I. Lin , M. Niederberger. A morphous cobalt silicate nanobelts@carbon composites as a stable anode material for lithium ion batteries, *Chem. Sci.*, **2015**, *6*, 6908-6915
- W. -I. Lin, C.-Y. Lin, S.-H. Wu, Y.-S Lin, Y. Huang, C. Chang, C.-Y. Mou. Gd(III)-containing Nanorattles for High Resolution Magnetic Resonance Angiography, *J. Mater. Chem. B*, **2013**, *1*, 639-645
- M. Makosch, W. -I. Lin, V. Bumbálek, J. Sá, J. W. Medlin, K. Hungerbühler and J. van Bokhoven. Organic Thiol Modified Pt/TiO_2 Catalysts to Control Chemoselective Hydrogenation of Substituted Nitroarenes, *ACS Catal*. **2012**, *2*, 2079-2081.

Poster Presentations at International conferences

- International Ramanfest, Berlin, **Germany**, 19-20, May, 2016
- 5th International Conference on tip-enhanced Raman Spectroscopy, Osaka, **Japan**, 29, Oct., 2015
- Swiss Chemical Society Fall meeting, Zürich, **Switzerland**, 11, Sept., 2014
- Scanning Probe Microscopy on Soft and Polymeric Materials, Toronto, **Canada**, 2-6, Sept., 2014
- 24th International Conference on Raman Spectroscopy, Jena, **Germany**, 10-15, Aug, 2014

Declaration of originality

Mathematisch-Naturwissenschaftliche Fakultät

Akademische Angelegenheiten

'I declare that I have produced this doctor's thesis independently using only the tools I have specified, in accordance with section 7 para. 3 of the Faculty of Mathematics and Natural Sciences PhD regulations, published in the Official Gazette of Humboldt-Universität zu Berlin (*Amtliches Mitteilungsblatt*) no. 126/2014 on 18/11/2014.'